# Model-Based Reconstruction Methods for MR Relaxometry

# Modellbasierte Rekonstruktionsmethoden für die MR-Relaxometrie

Dissertation zur Erlangung des naturwissenschaftlichen Doktorgrades
der Graduate School of Life Sciences,
Julius-Maximilians-Universität Würzburg,
Klasse Biomedizin

vorgelegt von

Johannes Tran-Gia
aus
Stuttgart

Würzburg, 2014

Eingereicht am: ……………………………………………………………………

## Mitglieder des Promotionskomitees:

Vorsitzender: Prof. Dr. Thomas Dandekar

1. Betreuer: Prof. Dr. Herbert Köstler

2. Betreuer: Prof. Dr. Dr. Dietbert Hahn

3. Betreuer: Prof. Dr. Meinrad Beer

4. Betreuer: Prof. Dr. Christian O. Ritter

Tag des Promotionskolloquiums: ……………………………………………

Doktorurkunden ausgehändigt am: …………………………………………

# Contents

**1 Introduction** **10**

**2 Theory** **13**
- 2.1 The FLASH Imaging Sequence . . . . . . . . . . . . . . . . . . . . . . . . . 13
- 2.2 Sampling Trajectories and Undersampling Artefacts . . . . . . . . . . . . 15
- 2.3 $T_1$, $T_2$ and $T_2^*$ Relaxation . . . . . . . . . . . . . . . . . . . . . . . . . . . . 16
- 2.4 Segmented Inversion Recovery $T_1$ Mapping . . . . . . . . . . . . . . . . . 18
- 2.5 Inversion Recovery Look-Locker $T_1$ Mapping . . . . . . . . . . . . . . . . 18
- 2.6 Saturation Recovery Look-Locker $T_1^*$ Mapping . . . . . . . . . . . . . . 20
- 2.7 Other $T_1$ Mapping Methods . . . . . . . . . . . . . . . . . . . . . . . . . . 21
- 2.8 $T_1$ Correction for Insufficient Relaxation Delays . . . . . . . . . . . . . . 21
- 2.9 From an RF Excitation Pulse to an Excited Slice . . . . . . . . . . . . . 23
- 2.10 Dictionary Learning in MR Relaxometry . . . . . . . . . . . . . . . . . . 24
- 2.11 A Sign-dependent Sum of Squares Approach for Coil Combination . . . . 26
- 2.12 Gadolinium-based Contrast Agents . . . . . . . . . . . . . . . . . . . . . . 28
- 2.13 SR-LL FLASH Sequences after the Admission of Contrast Agent . . . . . 29
- 2.14 Myocardial First-pass Perfusion Imaging . . . . . . . . . . . . . . . . . . 29
- 2.15 Quantification of Myocardial Perfusion Using DCE-MRI . . . . . . . . . 31
- 2.16 Quantification of Myocardial Perfusion Using Arterial Spin Labeling . . . 33

**3 Model-based Acceleration of Parameter Mapping (MAP)** **35**
- 3.1 Introduction . . . . . . . . . . . . . . . . . . . . . . . . . . . . . . . . . . 35
- 3.2 The MAP Reconstruction Scheme . . . . . . . . . . . . . . . . . . . . . . 35
- 3.3 Improvement of the Initial Estimates . . . . . . . . . . . . . . . . . . . . 37
- 3.4 Relaxation Models and Fitting Algorithms Used in MAP . . . . . . . . . 37
- 3.5 Using MAP with Multiple Receiver Coils . . . . . . . . . . . . . . . . . . 38

**4 MAP with Saturation Recovery Magnetization Preparation** **39**
- 4.1 Introduction . . . . . . . . . . . . . . . . . . . . . . . . . . . . . . . . . . 39
- 4.2 Implementation of SR-MAP . . . . . . . . . . . . . . . . . . . . . . . . . 39
- 4.3 Methods . . . . . . . . . . . . . . . . . . . . . . . . . . . . . . . . . . . . 40
  - 4.3.1 Numerical Simulations . . . . . . . . . . . . . . . . . . . . . . . . 40
  - 4.3.2 Phantom Experiments . . . . . . . . . . . . . . . . . . . . . . . . 41
  - 4.3.3 In Vivo Measurements . . . . . . . . . . . . . . . . . . . . . . . . 42
- 4.4 Results . . . . . . . . . . . . . . . . . . . . . . . . . . . . . . . . . . . . . 43
  - 4.4.1 Numerical Simulations . . . . . . . . . . . . . . . . . . . . . . . . 43
  - 4.4.2 Phantom Experiments . . . . . . . . . . . . . . . . . . . . . . . . 45

4.4.3 In Vivo Measurements . . . . . 47
4.5 Discussion . . . . . 49
4.5.1 Radial Versus Other Trajectories . . . . . 49
4.5.2 The MAP Algorithm under Presence of Motion . . . . . 50
4.5.3 Higher Intensity towards Outer Regions of the Field of View . . . 50
4.5.4 Dependence of the Accuracy of the $T_1^*$ Estimates on the Temporal Coverage . . . . . 50
4.5.5 Convergence Behavior of the Algorithm . . . . . 51
4.5.6 In Vivo Measurements . . . . . 51
4.5.7 Iterative Algorithm Versus Numerical Optimization . . . . . 52
4.5.8 Numerical Fit Versus Dictionary-based Approach . . . . . 52
4.5.9 Limits of the Mono-exponential Signal Model . . . . . 53

**5 MAP with Inversion Recovery Magnetization Preparation 54**
5.1 Introduction . . . . . 54
5.2 Implementation of IR-MAP . . . . . 54
5.3 Methods . . . . . 56
5.3.1 Phantom Experiments . . . . . 56
5.3.2 In Vivo Measurements . . . . . 58
5.4 Results . . . . . 58
5.4.1 Phantom Experiments . . . . . 58
5.4.2 In Vivo Measurements . . . . . 60
5.5 Discussion . . . . . 61
5.5.1 Phantom Experiments . . . . . 61
5.5.2 In Vivo Measurements . . . . . 63
5.5.3 Comparison of IR-MAP and SR-MAP . . . . . 65
5.5.4 Dependence of the Accuracy of the $T_1$ Estimates on the Temporal Coverage . . . . . 65
5.5.5 Duration of the IR-MAP Algorithm . . . . . 66
5.5.6 Comparison of IR-MAP to Existing $T_1$ Mapping Techniques . . . 66

**6 MAP for Dynamic Contrast-Enhanced $T_1$ Mapping 68**
6.1 Introduction . . . . . 68
6.2 Methods . . . . . 68
6.2.1 Implementation of IR-MAP . . . . . 69
6.2.2 Acquisition and Reconstruction Scheme . . . . . 69
6.2.3 Determination of the Quality of Inversion $K$ . . . . . 70
6.2.4 Validation Study: Phantom . . . . . 71
6.2.5 Validation Study: Healthy Volunteer . . . . . 71
6.2.6 Clinical DCE-MRI Examination . . . . . 71
6.3 Results . . . . . 72
6.3.1 Validation Study: Phantom . . . . . 72
6.3.2 Validation Study: Healthy Volunteers . . . . . 74
6.3.3 Clinical DCE-MRI Examination . . . . . 75

6.4 Discussion . . . . . 77
6.4.1 Validation Study: Phantom . . . . . 77
6.4.2 Validation Study: Healthy Volunteer . . . . . 78
6.4.3 Clinical DCE-MRI Examination . . . . . 79
6.4.4 Limitations of the Presented Combination of IR-MAP and T1C . 79
6.4.5 Temporal Resolution of the Presented Technique . . . . . 80
6.4.6 Advantages of the Proposed Approach over Existing $T_1$ Mapping Techniques . . . . . 80

**7 MAP for Arterial Spin Labeling Perfusion MRI in Small Animals 82**
7.1 Introduction . . . . . 82
7.2 Implementation of ASL-MAP . . . . . 84
7.3 Methods . . . . . 84
7.4 Results . . . . . 85
7.5 Discussion . . . . . 87

**8 Consideration of Slice Profiles (CSP) in IR-LL $T_1$ Mapping 90**
8.1 Introduction . . . . . 90
8.2 The CSP Model . . . . . 91
8.3 Methods . . . . . 92
8.3.1 Numerical Simulations . . . . . 93
8.3.2 Phantom Experiments . . . . . 93
8.3.3 In Vivo Measurements . . . . . 95
8.4 Results . . . . . 95
8.4.1 Numerical Simulations . . . . . 95
8.4.2 Phantom Experiments . . . . . 97
8.4.3 In Vivo Measurements . . . . . 99
8.5 Discussion . . . . . 101
8.5.1 Limitations of the Mono-exponential Relaxation Model . . . . . 102
8.5.2 Limitations of the CSP model . . . . . 104
8.5.3 Limitations in the Assumption of a Mono-exponential Behavior in Every Voxel . . . . . 104
8.5.4 Comparison of the Obtained $T_1$ Values to Standard Literature . . 105
8.5.5 Application Areas of the New Model . . . . . 105

**9 MAP for AIF Determination in Myocardial Perfusion MRI 106**
9.1 Introduction . . . . . 106
9.2 Implementation of SR-MAP . . . . . 107
9.3 Methods . . . . . 108
9.3.1 Determination of the Tissue Enhancement Curves . . . . . 109
9.3.2 Determination of Unsaturated Arterial Input Functions . . . . . 110
9.3.3 Comparison of the Perfusion Values . . . . . 111
9.4 Results . . . . . 111
9.4.1 Determination of the Tissue Enhancement Curves . . . . . 111
9.4.2 Determination of Unsaturated Arterial Input Functions . . . . . 113

9.4.3 Comparison of the Perfusion Values . . . . . . . . . . . . . . . . . . 114
9.5 Discussion . . . . . . . . . . . . . . . . . . . . . . . . . . . . . . . . . . . 115

**10 Summary and Conclusions 117**

**11 Zusammenfassung und Schlussfolgerungen 121**

**12 Outlook 126**

**A Bibliography 128**

**B Curriculum Vitae 138**

**C Publications 140**

**D Eidesstattliche Erklärung / Affidavit 142**

**E Acknowledgements 143**

**F Appendix 146**

# Abbreviations

**AIF** **A**rterial **I**nput **F**unction

**ASL** **A**rterial **S**pin **L**abeling

**CA** **C**ontrast **A**gent

**CSF** **C**erebro**S**pinal **F**luid

**CSP** **C**onsideration of **S**lice **P**rofiles

**CT** **C**omputed **T**omography

**DCE-MRI** **D**ynamic **C**ontrast-**E**nhanced **MRI**

**ECG** **E**lectro**C**ardio**G**ram

**EXP** mono-**EXP**onential three-parameter fit

**FAIR** **F**low sensitive **A**lternating **I**nversion **R**ecovery

**FAIR-LL FLASH** **FAIR** prepared **LL FLASH**

**FoV** **F**ield **o**f **V**iew

**FLASH** **F**ast **L**ow **A**ngle **SH**ot

**GL** **GL**obal

**GM** **G**rey **M**atter

**GRAPPA** **G**ene**R**alized **A**utocalibrating **P**artially **P**arallel **A**cquisition

**GROG** **GR**APPA **O**perator **G**ridding

**IR** **I**nversion **R**ecovery

**IR-LL** **I**nversion **R**ecovery **L**ook-**L**ocker acquisition

**IR-LL FLASH** **I**nversion **R**ecovery **L**ook-**L**ocker **FLASH**

**IR-MAP** **I**nversion **R**ecovery **MAP**

**IRFSE** **I**nversion **R**ecovery **F**ast **S**pin **E**cho

**KWIC** **k**-space **W**eighted **I**mage **C**ontrast

**LL** **L**ook-**L**ocker

**MAP** **M**odel-based **A**cceleration of **P**arameter mapping

**MBF** **M**yocardial **B**lood **F**low

**MR** **M**agnetic **R**esonance

**MRI** **M**agnetic **R**esonance **I**maging

**MRT** **M**agnet**r**esonanz**t**omographie

**NMR** **N**uclear **M**agnetic **R**esonance

**NRMSE** **N**ormalized **R**oot-**M**ean-**S**quare **E**rror

**OMP** **O**rthogonal **M**atching **P**ursuit

**PET** **P**ositron **E**mission **T**omography

**RF** **R**adio **F**requency

**RoI** **R**egion **o**f **I**nterest

**SNR** **S**ignal-to-**N**oise **R**atio

**SoS** square root of the **S**um **o**f **S**quares

**SR** **S**aturation **R**ecovery

**SR-LL FLASH** **S**aturation **R**ecovery **L**ook-**L**ocker **FLASH**

**SR-MAP** **S**aturation **R**ecovery **MAP**

**SS** **S**lice-**S**elective

**T1C** $\mathbf{T_1}$ **C**orrection

**TEC** **T**issue **E**nhancement **C**urve

**VFA** **V**ariable **F**lip **A**ngle

**WM** **W**hite **M**atter

# 1 Introduction

Due to a wide range of technical and methodological innovations, imaging modalities have become one of the major areas in the life sciences. First and foremost, **M**agnetic **R**esonance **I**maging (MRI) has established itself among the most important techniques for diagnostic imaging as it offers a large number of advantages over other imaging methods such as **C**omputed **T**omography (CT) and **P**ositron **E**mission **T**omography (PET). While CT is based on ionizing radiation to which the subject is exposed during the measurement, PET works by detecting ionizing radiation emitted by radioactive agents, which are introduced to the subject prior to the scan. In contrast to these techniques, which can potentially damage body cells, MRI utilizes a combination of static magnetic fields and high frequency electromagnetic fields for image acquisition. The absence of any known long-term side-effects not only greatly improves the patient safety, but also enables risk-free volunteer studies, which can be of great importance in many areas of clinical research. **M**agnetic **R**esonance (MR) images have an inherently high soft tissue contrast, which can, to a large extent be adjusted through the imaging parameters. Compared to most imaging modalities, which only offer the possibility of observing a very limited set of physical properties (e.g. electron density in x-ray imaging), MRI additionally enables the observation of a wide range of parameters such as proton density, diffusion, flow, and temperature. Even complex quantities like tissue perfusion or brain activation can be observed using the appropriate techniques.

Amongst this variety of parameters, mapping the longitudinal relaxation time $T_1$ has widespread applications in clinical MRI as it promises a quantitative comparison of tissue properties across subjects and scanners. A quantitative assessment of tissue is relevant in the detection of many pathologies such as diffuse myocardial fibrosis in cardiac MRI [45, 63] or inflammation, infarction, white matter edema and tumor malignancy in neurological MRI [10, 43, 71, 87]. Moreover, the continuous quantification of the $T_1$ relaxation parameter during the first and delayed passage of paramagnetic contrast agents would bring a great benefit towards the quantification of **D**ynamic **C**ontrast-**E**nhanced **MRI** (DCE-MRI) in pathologies like brain tumors [69, 76] and obstructive coronary artery disease [61,91,107]. Due to the long scan times of conventional methods, however, the use of quantitative MRI in clinical routine is still very limited.

In relaxation-based MR parameter mapping, a suitable magnetization preparation is typically applied, followed by the acquisition of a predefined number of images of the relaxation process. After the acquisition, these snapshots and a relaxation model according to the type of preparation applied are used for a fit of the relaxation parameters. In presence of short relaxation times, however, the acquisition of multiple images with a spatial and temporal resolution that is sufficient for clinical use can be difficult or even impossible [18,88]. One approach to overcome this problem is a segmentation of the data acquisition process [39, 59]. After each magnetization preparation pulse, only fractional parts of the desired k-space are acquired corresponding to different contrasts of the relaxation process. By repeating this measurement with different k-space lines, the temporal resolution can be highly improved. For the most commonly used **I**nversion **R**ecovery (IR) preparation, a sufficient delay is required between two repetitions to ensure a complete relaxation back to the thermal equilibrium before the subsequent preparation pulse is applied. Alternatively to the lengthy segmented acquisition techniques, single-preparation techniques with a very low spatial resolution have to be used, impairing the accuracy of the resulting parameter maps. Therefore, ways to reconstruct high-resolution images from undersampled k-spaces with less data sampled than required by the Nyquist criterion would be desirable for fast and accurate $T_1$ mapping.

Parallel imaging techniques [36, 75] exploit the information received in multiple receiver coils to resolve aliasing in images reconstructed from coherently undersampled k-space data. In these methods, however, the **S**ignal-to-**N**oise **R**atio (SNR) is limited by noise enhancement due to the geometry factor of the particular coil setup and the signal loss due to the reduction in the number of k-space points acquired. In dynamic studies, non-Cartesian trajectories such as radial sampling schemes, which redundantly sample the low spatial frequencies, can be used to reduce motion artifacts especially in undersampled acquisitions [35, 64]. Contrast manipulation techniques such as **k**-space **W**eighted **I**mage **C**ontrast (KWIC) use k-space filters to enhance or reduce the amount each of the acquired projections contributes to the central region of k-space to generate multiple images of different contrast from radially acquired single-preparation experiments [27, 85]. A considerable disadvantage of these techniques is the lack of consistency caused by the averaging of data belonging to various time points, which could possibly lead to errors in the estimated contrasts.

Over the past years, model-based reconstruction techniques based on the mathematical theory of compressed sensing [11,26] have become a very active field of research in MRI. Images can be recovered from incoherently undersampled k-space data by exploiting sparsity in any known transform domain. Apart from frequently used sparse transform domains such as the wavelet or $x$-$f$ domain [32,60], more specific sparsifying transforms such as the exponential relaxation parameter spaces of $T_1$ and $T_2$ after magnetization preparation [8,25,90] have recently been used to obtain images and parameter maps from undersampled k-space data.

In this work, a **M**odel-based **A**cceleration of **P**arameter mapping (MAP) technique for $T_1$ mapping is presented, enabling the model-based reconstruction of a parameter map from undersampled datasets of different stages of the relaxation process. In the most extreme case, one image can be reconstructed for each radial projection obtained in a **L**ook-**L**ocker (LL) [59] acquisition after the application of a single magnetization preparation pulse. It makes use of the fact that each of the projections carries information about a single time point of the relaxation curve. By enforcing an appropriate relaxation model to the measured data, MAP is capable of fully resolving an exponential signal evolution after the application of a preparation pulse using a single-preparation dataset.

### Organization of the thesis

First, all methodological concepts of MRI that are relevant for a better understanding of this work are described in **chapter 2**. Subsequently, the model-based reconstruction algorithm MAP, which will be used throughout this work, is introduced in **chapter 3**. **Chapters 4** and **5** present implementations of MAP for saturation recovery as well as inversion recovery prepared sequences. **Chapter 6** describes how MAP can be used for dynamic $T_1$ mapping with the example of a dynamic contrast-enhanced MRI experiment of the brain. In **chapter 7**, the MAP technique is adjusted for perfusion measurements in small animals using an **A**rterial **S**pin **L**abeling (ASL) technique. **Chapter 8** introduces a way of considering the slice profiles of **R**adio **F**requency (RF) excitation pulses in the relaxation model and improving the $T_1$ fit. Finally, **chapter 9** presents an implementation of MAP for an **A**rterial **I**nput **F**unction (AIF) estimation, which is essential for quantitative myocardial first-pass perfusion MRI.

# 2 Theory

There is broad literature about the basic principles of **N**uclear **M**agnetic **R**esonance (NMR) and MRI [6, 38, 62]. Therefore, some MRI basics such as the physics of the signal generation, spatial encoding using magnetic field gradients, the k-space concept and the Fourier transform will not be dealt with in great detail. Instead, only the concepts that are relevant for an understanding of this work will be mentioned and described in the following theory section.

## 2.1 The FLASH Imaging Sequence

MRI pulse sequences combine **R**adio **F**requency (RF) pulses and magnetic field gradients for image acquisition. One sequence that will be used throughout this work is the spoiled gradient echo sequence, which combines one RF excitation pulse with a series of gradient pulses to create a single echo. The pulse diagram is depicted in Figure 2.1.

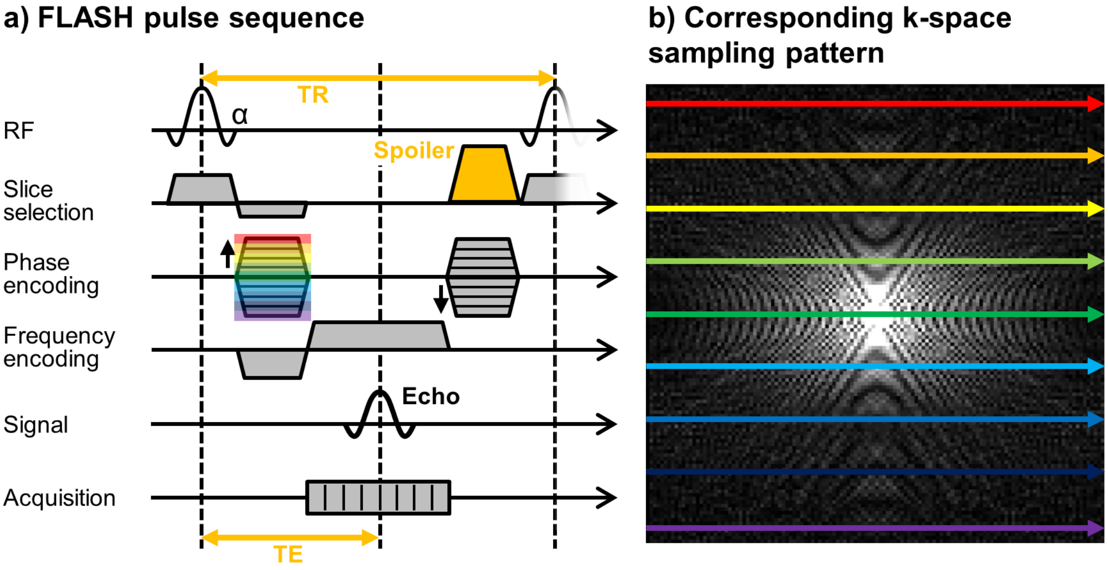

**Figure 2.1:** Spoiled gradient echo sequence. Shown is the pulse diagram (a) as well as the corresponding k-space sampling pattern (b).

First, a slice-selection gradient is applied simultaneously to an RF excitation pulse of flip angle $\alpha$ for a slice-selective excitation in the $z$-direction. Next, a $y$-dependent phase encoding gradient is applied, modifying the spin resonance frequencies depending on the location in the $y$-direction. This results in a phase modulation in the $y$-direction after the gradient is switched off. Finally, a frequency encoding gradient is applied during data collection, modifying the Larmor frequency depending on the $x$-location. Only one line of k-space is acquired in each repetition of this sequence. It has to be repeated multiple times with different phase encoding gradients to fully encode a 2D k-space (colored boxes in Fig. 2.1a).

Using the described pattern, a relaxation delay is required between two repetitions of the described gradient echo pulse sequence to ensure that the equilibrium magnetization $M_0$ is restored and no transverse magnetization $M_{xy}$ is left before the next RF excitation pulse is applied. Therefore, any remaining transverse magnetization has to be dephased (spoiled) in order to shorten the relaxation delay. Typically, two spoiling techniques are combined to obtain the best possible dephasing:

- **Spoiling Gradients:** A straightforward way of spoiling is the application of gradients at the end of each repetition to dephase any transverse magnetization. An exemplary spoiling gradient is indicated in orange in Figure 2.1a. While the echo time $T_E$ between the RF excitation pulse and the formation of the echo is unaffected by this modification, the repetition time $T_R$ between two consecutive RF excitation pulses can considerably be reduced.

- **RF Spoiling:** To further prevent transverse magnetization remaining from an RF pulse from interfering with the transverse magnetization which is brought to the transverse plane by the subsequent RF excitation pulse, each RF pulse is transmitted with a different phase. In RF spoiling, the phase differences between subsequent pulses increase linearly by a so-called phase increment (e.g. 117° [111] or 84° [29]).

Although the transverse magnetization can be effectively dephased by spoiler gradients and RF spoiling, the longitudinal magnetization will not be completely relaxed into equilibrium if $T_R$ is shorter than the required relaxation time. Therefore, a steady-state magnetization forms after a number of repetitions, with a magnitude depending on the flip angle $\alpha$ used for the RF excitations. For this reason, low flip angles are typically used in spoiled gradient echo sequences, which will be called **F**ast **L**ow **A**ngle **SH**ot (FLASH)[40] pulse sequence throughout this work. The steady-state signal can be described by [22]

$$S_{\text{FLASH}} = \frac{M_0(1 - E_1)\sin(\alpha)}{(1 - E_1 \cos(\alpha))} \,, \tag{2.1}$$

where $M_0$ is the equilibrium magnetization, $\alpha$ is the flip angle and $E_1 = \exp(-T_R/T_1)$ is a factor dependent on the repetition time $T_R$ and the longitudinal relaxation time $T_1$ (see section 2.3).

## 2.2 Sampling Trajectories and Undersampling Artefacts

Instead of traversing k-space in a line-by-line fashion, the so-called Cartesian sampling pattern, alternative paths can be used for data collection in k-space. Although, in principle, there is an infinite number of sampling trajectories, two non-Cartesian sampling schemes have established themselves besides the most frequently used Cartesian trajectories, namely the radial trajectory, which is also known as projection reconstruction [35], and the spiral trajectory [64]. Both sampling schemes are illustrated in Figure 2.2. As the center of k-space is sampled with every readout, these trajectories are very robust in the presence of motion or flow. Moreover, sampling the k-space center can be beneficial if changes in contrast appear during the acquisition as for example in acquisitions performed after a magnetization preparation, which will be described in one of the following sections.

For non-Cartesian sampling, the acquired data are typically brought to a Cartesian grid to simplify further post-processing in what is called gridding. The most commonly used technique for gridding is convolution gridding [46], where each (non-Cartesian) data point is convolved with a gridding kernel, and the result sampled and accumulated on a Cartesian grid. A density compensation function $w = w(|\boldsymbol{r}|)$ decreasing with the distance $|\boldsymbol{r}|$ to the k-space center is typically applied to compensate for the oversampling of the central k-space. In a different approach for gridding, non-Cartesian points are shifted to the nearest Cartesian location. It is based on the concept of parallel imaging and especially the **G**ene**R**alized **A**utocalibrating **P**artially **P**arallel **A**cquisition (GRAPPA) technique, which includes the information from multiple receiver coils in the image reconstruction, and which will not be dealt with in this work. A detailed explanation can be found in [7,36,41,75,84]. Based on this technique, the so-called GRAPPA operator can be derived that shifts data in k-space by arbitrarily small amounts. The self-calibrating **GR**APPA **O**perator **G**ridding (GROG) technique [80, 81] makes use of this GRAPPA operator. First, all acquired points are shifted to the nearest Cartesian location. Next, each of the resulting k-space points is divided by the number of k-space points that were shifted to this Cartesian location to compensate for the non-uniform density of the non-Cartesian trajectories (similar to the density compensation function $w$ in convolution gridding).

Many contrast manipulation approaches such as the **k**-space **W**eighted **I**mage **C**ontrast (KWIC) technique [85] make use of the fact that the central region of k-space is intrinsically oversampled for radial or spiral k-space sampling. While the weighting function $w$ is usually only applied to compensate for the non-uniform density of non-Cartesian trajectories, these techniques apply different filters to enhance or reduce the amount each acquired radial projection or spiral arm contributes to the central k-space region. This enables the reconstruction of a dynamic image series from a continuous acquisition of dynamic processes such as a moving object (e.g. cardiac motion) or an image contrast which is changing during the acquisition (e.g. if $T_1$ or $T_2$ relaxation is present which will be described in the next section). However, although the KWIC technique appears to generate a dynamic image series, it uses temporal averaging, which can lead to image artifacts if the temporal footprint, that is the time interval in which all the data used to reconstruct the respective image were acquired, is too large. Such filtering techniques are inapplicable for Cartesian sampling where only the k-space line without phase encoding traverses the k-space center.

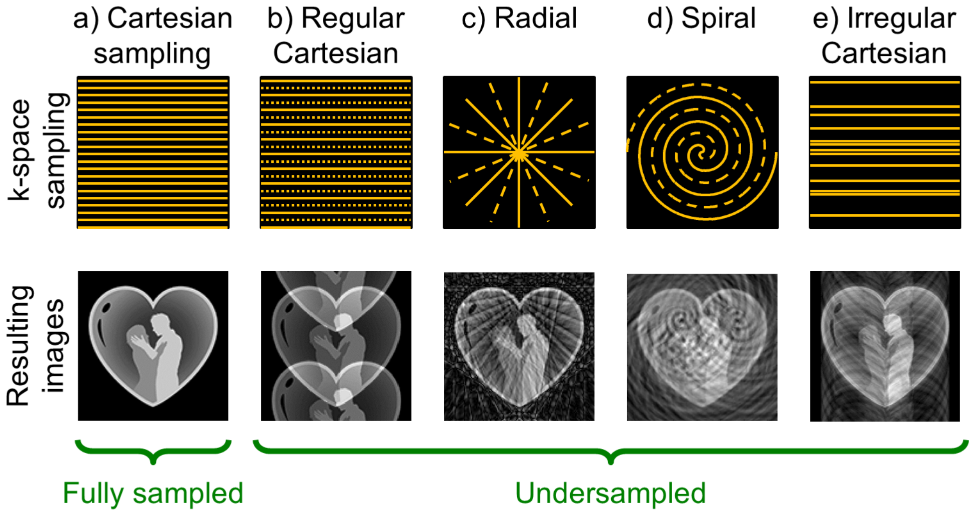

**Figure 2.2:** Cartesian and non-Cartesian undersampling. Depicted are k-space sampling patterns (top) and the resulting images (bottom) for a Nyquist sampled image (a) and for different undersampling patterns (b-e).

Another major difference between Cartesian and non-Cartesian trajectories is the appearance of undersampling artifacts, that is, if less data than required by the Nyquist limit are acquired. In contrast to Cartesian sampling, where so-called "coherent" aliasing artifacts appear as replicas of the image in the typically undersampled phase encoding direction (Fig. 2.2b), non-Cartesian aliasing artifacts are more evenly distributed in all directions of the imaging plane and therefore have a more noise-like appearance, as illustrated in Figure 2.2c&d. Therefore, it is often possible to recognize an underlying object despite a high acceleration factor if the images are undersampled with a non-Cartesian trajectory, providing a great potential for many MRI applications.

Non-Cartesian versions of any MRI pulse sequence (e.g. the FLASH sequence described in section 2.1) can be obtained by omitting the phase encoding gradient and by applying frequency encoding gradients in both spatial dimensions ($x$- and $y$-direction) instead. The shape of these gradients can be adjusted to traverse the k-space in any desired manner.

## 2.3 $T_1$, $T_2$ and $T_2{}^*$ Relaxation

For a spin system in a static magnetic field at thermal equilibrium, the phases of the magnetic moments are uncorrelated, leading to a net magnetization $\vec{M}_0$ that is perfectly aligned with the static magnetic field ($z$-direction). By appropriately applying an RF pulse, the spin system can be excited, resulting in a net magnetization in the transverse plane ($M_{xy}$), which is usually measured in an MRI acquisition. Subsequently, the magnetization relaxes back into equilibrium, which can be described by two different relaxation parameters:

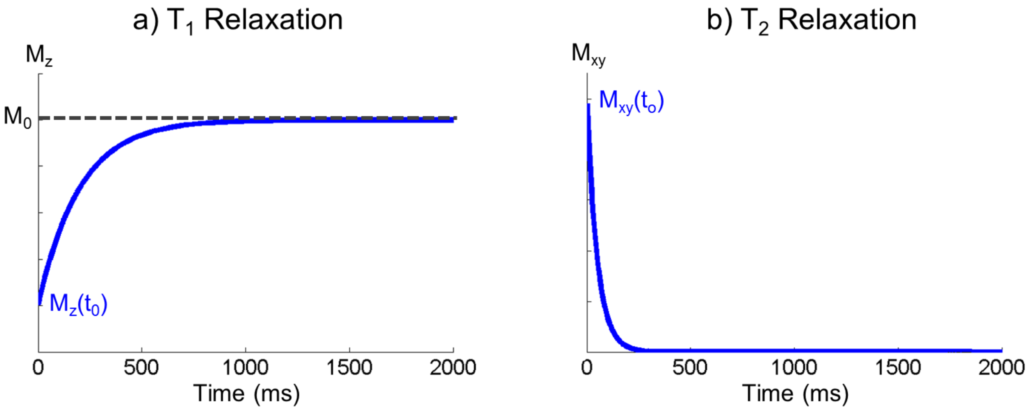

**Figure 2.3:** Exemplary relaxation curves for $T_1 = 200\,\text{ms}$ (a) and $T_2 = 100\,\text{ms}$ (b).

- The $T_1$ relaxation time is a measure of how quickly the magnetization recovers towards its equilibrium orientation in the direction of the static magnetic field. As the return of excited protons from the high energy state to the ground state is associated with a loss of energy to the surrounding lattice, it is also known as spin-lattice relaxation time. If $M_z(t_0)$ describes the $z$-component after an excitation, its relaxation back to the equilibrium $M_0$ can be described as follows:

  $$M_z(t) = M_0 + [M_z(t_0) - M_0] \cdot \exp(-t/T_1)\,. \tag{2.2}$$

  An examplary $T_1$ relaxation curve for $T_1 = 200\,\text{ms}$ is depicted in Figure 2.3a.

- The $T_2$ relaxation time characterizes the rate of dephasing of magnetic moments in the transverse plane after excitation by an RF pulse. As $T_2$ relaxation only refers to dephasing that is caused by interactions between the spins of an ensemble, it is also referred to as spin-spin relaxation. A transverse magnetization of $M_{xy}(t_0)$ is typically described by:

  $$M_{xy}(t) = M_{xy}(t_0) \cdot \exp(-t/T_2)\,. \tag{2.3}$$

  An examplary $T_2$ relaxation curve for $T_2 = 100\,\text{ms}$ is depicted in Figure 2.3b.

- $T_2^*$ decay refers to a total decrease in transverse magnetization following the initial excitation pulse. In contrast to the $T_2$ relaxation, it includes dephasing that is not caused by other spins of the ensemble, such as local field inhomogeneities caused by hardware imperfections or magnetic susceptibility effects in the patient within the magnetic field.

## 2.4 Segmented Inversion Recovery $T_1$ Mapping

$T_1$ can be very accurately determined by a segmented **I**nversion **R**ecovery (IR) experiment. At a starting time $t_0$, the equilibrium magnetization $M_0$ is inverted by a 180° RF pulse, the so-called magnetization preparation pulse. As described in section 2.3, the magnetization subsequently relaxes back to the thermal equilibrium $M_0$ according to Eq. 2.2. In case of an inversion recovery magnetization preparation, the starting magnetization equals the negative equilibrium magnetization, that is $M(t_0) = -M_0$, and Eq. 2.2 simplifies to

$$M(t) = M_0 \cdot [1 - 2\exp(-t/T_1)] \ . \tag{2.4}$$

For reasons of clarity, the index $z$ is typically omitted. An RF excitation pulse can be applied at a specific inversion time $t = T_I$ to obtain one line of k-space corresponding to this specific contrast (e.g. using a FLASH readout as described in section 2.1). In a segmented IR experiment, this acquisition is repeated for a predefined number of inversion times $T_I$ and k-space lines to obtain a set of snapshots of the relaxation process. A pixel-wise fit of Eq. 2.4 to the resulting image series leads to a spatial distribution of $T_1$ relaxation parameters over the desired **F**ield **o**f **V**iew (FoV), a so-called $T_1$ map. It is important to keep a relaxation break between successive acquisitions to ensure that the equilibrium magnetization is reached before each acquisition and that $M(t_0) = -M_0$.

Unfortunately, the relaxation of the magnetization according to Eq. 2.4 requires $\sim 5\,T_1$ to reach 99 % of the equilibrium magnetization $M_0$. As an example, the relaxation in gray matter tissue where $T_1 \approx 1.4\,\mathrm{s}$ at a field strength of 3 T [30, 65, 110] requires 7.4 s to reach 99 % of $M_0$ and even 13.9 s to reach 99.99 %. While a segmented acquisition with insufficient relaxation delays would result in $T_1$ errors, an extension of these delays leads to unacceptably lengthy scan times.

As an example, the acquisition of a $128 \times 128$ matrix at 10 different $T_I$ would require $128 \cdot 10 = 1280$ inversions. It would therefore require a total delay time of $1280 \cdot 7.4\,\mathrm{s} = 9472\,\mathrm{s} \approx 2.6\,\mathrm{h}$ to obtain correct $T_1$ values in **G**rey **M**atter (GM) regions of a human brain. Therefore, the segmented IR $T_1$ mapping technique described in this section can only be used for the acquisition of reference $T_1$ values, i.e. in phantom measurements where time-efficiency of the acquisition is of less relevance. Other, much faster techniques have been developed for in vivo applications, one of which will be presented in the next section.

## 2.5 Inversion Recovery Look-Locker $T_1$ Mapping

As described in the previous section, the segmented inversion recovery acquisition has the major disadvantage of acquiring only a single line of k-space per inversion pulse. Combined with the lengthy relaxation time between successive inversions, this leads to unacceptably long scan times.

This acquisition time can be significantly reduced by the so-called **L**ook-**L**ocker (LL) concept [59], which enables a high acceleration of inversion recovery $T_1$ mapping. As in the segmented IR acquisition, the sequence is started by applying an inversion pulse for magnetization preparation. Instead of only applying one RF excitation pulse and acquiring one line of k-space after each of the inversions, Look-Locker techniques apply a series of low-angle RF pulses for a spoiled gradient echo (FLASH) acquisition of multiple k-space lines after each IR pulse. According to [20], the continuous application of RF excitation pulses of flip angle $\alpha$ results in a modified relaxation time $T_1^* < T_1$ which can be described by

$$T_1^* = \frac{1}{1/T_1 - (1/T_R) \cdot \ln(\cos(\alpha))} , \tag{2.5}$$

where the repetition time $T_R$ denotes the time between two consecutive RF excitations. Additionally, the continuous application of RF excitation pulses leads to a modified steady-state magnetization $M_0^* < M_0$:

$$M_0^* = M_0 \cdot \frac{1 - \exp(-T_R/T_1)}{1 - \exp(-T_R/T_1^*)} . \tag{2.6}$$

For $T_R \ll T_1^* < T_1$, this can be simplified to

$$M_0^* = M_0 \cdot T_1^*/T_1 . \tag{2.7}$$

This new parameter set $(M_0, M_0^*, T_1^*)$ defines the relaxation process in this so-called **I**nversion **R**ecovery **L**ook-**L**ocker **FLASH** (IR-LL FLASH) sequence:

$$M(t) = M_0^* - (M_0 + M_0^*) \cdot \exp(-t/T_1^*) . \tag{2.8}$$

After the acquisition of a set of images of different contrasts, $M_0^*$, $M_0$ and $T_1^*$ can be determined by means of a three-parameter least-squares fit of Eq. 2.8. The desired value $T_1$ can then be calculated using a combination of Eqs. 2.7 and 2.8:

$$T_1 = T_1^* \cdot [(M_0 + M_0^*)/M_0^* - 1] . \tag{2.9}$$

Again, this relation only holds if the spin system is at equilibrium before the application of the inversion pulse.

Instead of only a single line of k-space, multiple k-space lines can be acquired after each inversion using the IR-LL FLASH sequence, leading to a considerable reduction in scan time. If images at 10 different $T_I$ were to be acquired in a $T_1$ mapping experiment, the scan time would be reduced by a factor of 10 as all 10 contrasts for one line of k-space could be acquired after each inversion. The $128 \times 128$ matrix of the example in the previous section could be acquired in ~ 16 min instead of 2.6 h using the IR-LL FLASH technique.

As mentioned in section 2.2, the IR-LL FLASH sequence can be applied with any Cartesian or non-Cartesian trajectory.

## 2.6 Saturation Recovery Look-Locker $\mathbf{T_1}^*$ Mapping

The inversion recovery preparation scheme, which is used in the previously described $T_1$ mapping techniques, requires long waiting periods between subsequent acquisitions to ensure that the equilibrium magnetization $M_0$ is reached before the application of each inversion pulse. To avoid these relaxation delays, a **S**aturation **R**ecovery (SR) preparation scheme can be used instead. In this case, the magnetization is brought to zero by a 90° RF pulse before the spoiled gradient echo acquisition is carried out. The magnetization directly after the SR pulse is ideally $M(t_0) = 0$, and Eq. 2.8 becomes:

$$M(t) = M_0^* \cdot [1 - \exp(-t/T_1^*)] \ . \tag{2.10}$$

Although this so-called **S**aturation **R**ecovery **L**ook-**L**ocker **FLASH** (SR-LL FLASH) acquisition can be described by a very simple two-parameter model, the new model Eq. 2.10 no longer provides information about the equilibrium magnetization $M_0$. Therefore, Eq. 2.9 can no longer be used for calculating $T_1$ out of the effective longitudinal relaxation parameter $T_1^*$. Although - in general - Eq. 2.5 could be used instead to calculate $T_1$ out of $T_1^*$, variations of the $B_1$ pulse amplitude lead to variations of the flip angle $\alpha$ across the FoV. This can cause considerable errors in a calculation of $T_1$ by simply using the nominal flip angle that is entered by the operator in the scanner console. Instead, the exact flip angle has to be determined in each voxel if $T_1$ is to be calculated using Eq. 2.9. This typically leads to an additional scan that might be required, in turn prolonging the scan time. An additional disadvantage is the saturation of the equilibrium magnetization prior to the FLASH acquisition, which leads to a loss in SNR compared to an inversion magnetization preparation, where the acquisition starts at the inverted equilibrium magnetization. Despite these limitations, the saturation recovery preparation scheme has been used for the elimination of relaxation breaks in a variety of applications where a magnetization preparation is unavoidable [14, 21, 82].

A more precise yet more complex description of an SR prepared Look-Locker FLASH acquisition is given in [48]. It includes the delay $T_D$ between the saturation preparation pulse and the first excitation pulse of the FLASH acquisition into the relaxation model given by Eq. 2.10:

$$M(n) = M \cdot (1 - E_D) \cdot a^{n-1} + M \cdot (1 - E_1) \cdot \frac{1 - a^{n-1}}{1 - a}$$

$$\text{where} \quad M = M_0 \cdot \sin(\alpha) \cdot e^{-T_E/T_2^*}, \quad E_D = e^{-T_D/T_1},$$

$$E_1 = e^{-T_R/T_1}, \quad a = \cos(\alpha) \cdot E_1 \ . \tag{2.11}$$

## 2.7 Other T$_1$ Mapping Methods

Besides the segmented IR and LL-based methods for $T_1$ mapping, there are two other main methods for determining $T_1$:

**I**nversion **R**ecovery **F**ast **S**pin **E**cho (IRFSE) measurements use spin echoes rather than gradient echoes for $T_1$ mapping. As described in section 2.4, the magnetization relaxes back to the equilibrium according to Eq. 2.4 after the application of an IR preparation pulse. After an appropriate inversion time $T_I$, a 90° excitation pulse is applied to rotate the available $z$-magnetization to the transverse plane and obtain a transverse magnetization $M_{xy}$ proportional to the $M(T_I)$. Subsequently, multiple echoes are generated out of this transverse magnetization using a fast spin echo sequence [42,58]. These sequences use multiple 180° refocusing pulses to continually invert the dephasing of the spins in the transverse plane. One echo is generated per applied refocusing pulse, using phase encoding and frequency encoding as described in section 2.1. All data collected after the initial 90° excitation pulse carries the contrast of the inversion time $T_I$. The number of k-space lines that can be acquired after one inversion is limited by the $T_2$ decay of the transverse magnetization $M_{xy}$. Therefore, multiple acquisitions of the same $T_I$ have to be performed in most cases to obtain an entire 2D k-space of one contrast of the $T_1$ relaxation process. Similar to section 2.4, the acquisition is repeated for a predefined number of inversion times $T_I$ to obtain a set of snapshots of the relaxation process. Again, a pixel-wise fit of Eq. 2.4 to the resulting image series yields a $T_1$ map.

**V**ariable **F**lip **A**ngle (VFA) approaches use 2D or 3D FLASH acquisitions of at least two different flip angles $\alpha_j$ for the quantification of the longitudinal relaxation time $T_1$ [22, 100]. According to [9], the steady-state signal $S_{\text{FLASH}}$ of a FLASH sequence (Eq. 2.1) can be represented in the linear form $y = mx + b$ as:

$$\frac{S_{\text{FLASH}}}{\sin(\alpha_j)} = E_1 \frac{S_{\text{FLASH}}}{\tan(\alpha_j)} + M_0(1 - E_1) \,, \tag{2.12}$$

where the same image is acquired with only the flip angle $\alpha_j$ changed. Using linear regression, $T_1$ and $M_0$ can be calculated out of the slope $m$ and the $y$-intercept $b$:

$$T_1 = -T_R / \ln(m) \ , \ \ M_0 = b/(1 - m) \,. \tag{2.13}$$

## 2.8 T$_1$ Correction for Insufficient Relaxation Delays

As it was mentioned in section 2.5, the calculation of $T_1$ out of the fitted parameters $M_0$, $M_0^*$ and $T_1^*$ using Eq. 2.9, as it is typically performed in inversion recovery Look-Locker $T_1$ mapping, only results in accurate $T_1$ values if the spin system is at equilibrium before the application of the inversion pulse. Relaxation delays of $\sim 5T_1$ as they were described in section 2.4 would be in the order of several seconds for most types of human tissue, leading to lengthy and ineffective acquisitions. Therefore, shorter waiting times are often used in LL-based parameter mapping, leading to errors for high $T_1$ values.

In [83], a method was presented to correct for the insufficient relaxation between consecutive IR-LL FLASH acquisitions and determine the underlying $T_1$ value from a parameter set $(M_A, M_B, T_1^*)$ obtained from a fit of Eq. 2.8 with $M_0^* \to M_A$ and $M_0 \to -M_B$:

$$M(t) = M_0^* - (M_0 + M_0^*) \cdot \exp(-t/T_1^*)$$

$$\Downarrow$$

$$M(t) = M_A - (M_A - M_B) \cdot \exp(-t/T_1^*)\,. \tag{2.14}$$

It makes use of the fact that the proportion of $T_1^*$ relaxation during the acquisition followed by $T_1$ relaxation during the waiting period, which is illustrated in Figure 2.4, is precisely known. By exploiting this knowledge, a set of underlying parameters $T_1$ and $M_0$ best describing the observed relaxation behavior in every voxel of the acquired FoV can be found.

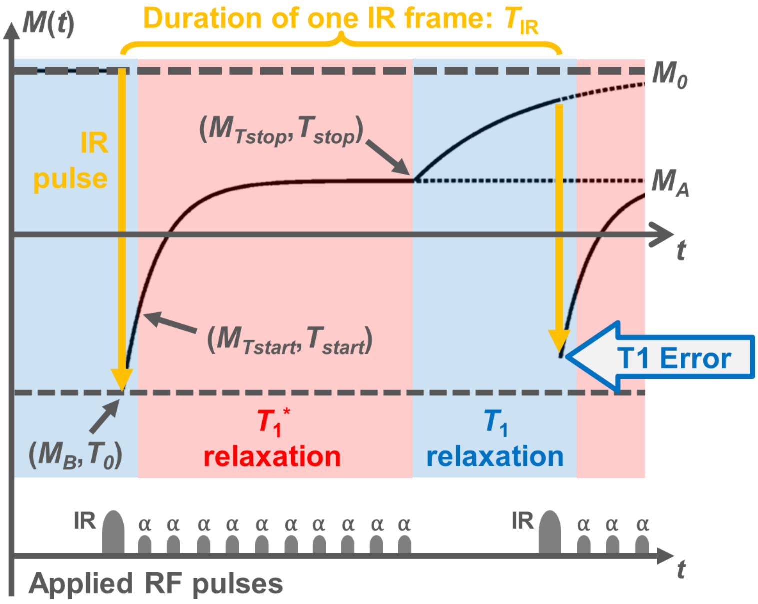

**Figure 2.4:** The relaxation process of an entire IR frame. After the inversion pulse at $T_0$ and a short period of undisturbed $T_1$ relaxation (blue background), an IR-LL FLASH pulse sequence is applied from $T_{\text{start}}$ until $T_{\text{stop}}$ (red background). The magnetization at these time points is denoted by $M_{T_{\text{start}}}$ and $M_{T_{\text{stop}}}$. A fit of Eq. 2.14 to the IR-LL FLASH curve yields the magnetization $M_B$ directly after inversion, a steady-state magnetization $M_A$ owed to the continuous RF excitation and the apparent $T_1^*$. The acquisition is followed by a waiting period of $T_{\text{IR}} - T_{\text{stop}}$ of undisturbed $T_1$ relaxation until the whole process is repeated at $T_{\text{IR}}$. If this waiting period is too short for the magnetization in order to reach the equilibrium, an error can be introduced in the determination of $T_1$.

First, the following expression for $T_1$ is derived:

$$T_1 = -\frac{T_R}{\ln\left[1 - \left(M_A - M_A \cdot e^{-T_R/T_1^*}\right)/M_0\right]} \,. \tag{2.15}$$

$M_0$ is the only unknown parameter in this equation as $T_R$ represents the exactly known repetition time between two excitation pulses of the IR-LL FLASH acquisition and $M_A$ as well as $T_1^*$ can be obtained by a three-parameter fit of Eq. 2.14.

Subsequently, the following term for $M_0$ can be derived:

$$M_0 = \frac{M_{T_\text{start}} + M_{T_\text{stop}} \cdot K \cdot e^{-T_\text{start}/T_1} \cdot e^{-(T_\text{IR}-T_\text{stop})/T_1}}{1 - e^{-T_\text{start}/T_1} \cdot \left[1 + K - K \cdot e^{-(T_\text{IR}-T_\text{stop})/T_1}\right]} \,. \tag{2.16}$$

Here, a parameter $K$ was introduced describing the quality of the inversion pulse (0: no inversion, 1: perfect inversion), and $T_\text{IR}$ denotes the time between two consecutive inversions. Additionally, $T_\text{start}$ and $T_\text{stop}$ represent the acquisition times at the start and stop of the IR-LL FLASH excitation pulse train and $M_{T_\text{start}}$ and $M_{T_\text{stop}}$ stand for the magnetization at these time points. The entire relaxation process of an IR-LL FLASH acquisition followed by a relaxation delay of pure $T_1$ relaxation before the next inversion pulse, which is called IR frame in the following, is illustrated in Figure 2.4.

In the following, a fully sampled set of images of an IR-LL FLASH relaxation process is considered that was recorded after an insufficient relaxation break. In addition, it is assumed that the inversion efficiency $K$ is known. After obtaining the parameter set $(M_A, M_B, T_1^*)$ in a voxel-wise fit of Eq. 2.14, the resulting $T_1^*$ is used as initial guess for $T_1$ and inserted in Eq. 2.16 to obtain an initial guess for $M_0$. This value can in turn be used as input to Eq. 2.15 to receive a better estimate for $T_1$. This succession is repeated until $T_1$ converges to a value where no significant changes occur between two successive iterations. By repeating this iterative process in every voxel of the acquired FoV, a map of $T_1$ values best describing the relaxation behavior of the respective voxel can be derived. This iterative $T_1$ correction will be referred to as $\mathbf{T_1}$ **C**orrection (T1C) in the following.

## 2.9 From an RF Excitation Pulse to an Excited Slice

In MRI, RF excitation pulses are typically used for selecting the slice to be imaged. In the ideal case of a sinc excitation pulse of infinite duration, this results in a rectangular excitation profile in the observed object (dotted black line in Fig. 2.5b). To keep the scan time acceptably short for clinical applications, filtered excitation pulses in the order of milliseconds are usually applied. As an example, the amplitude of a commonly used Hanning-filtered sinc pulse is given by:

$$A(t) = \frac{1}{2} \cdot \left[1 + \cos(\pi t)\right] \cdot \text{sinc}(t) \,. \tag{2.17}$$

An example of a Hanning-filtered sinc pulse of 800 $\mu$s duration sampled every 0.1 $\mu$s (i.e. 8000 samples) is given in Figure 2.5a. A Bloch equation simulation can be applied to obtain a distribution $\breve{A}(\omega)$ of excitation amplitudes in the frequency domain.

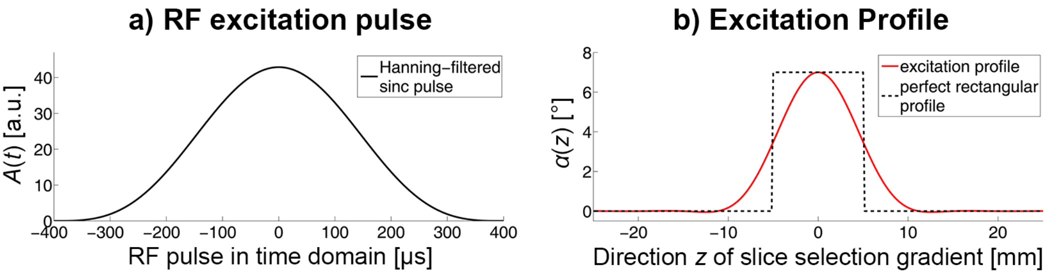

**Figure 2.5:** From RF excitation pulse to the excited slice. a: Hanning-filtered sinc pulse of 800 $\mu$s duration in the time domain. b: Corresponding excitation profile obtained by a Fourier transform (red line) and the desired perfect rectangular profile for a nominal flip angle of $\alpha_0 = 7°$, a repetition time of $T_R = 4.24$ ms and slice thickness 10 mm (black dashed line).

According to [6,70], a straightforward Fourier transform of $A(t)$ leads to a distribution

$$\widetilde{A}(\omega) = \int_{-\infty}^{\infty} A(t) \cdot \exp(-i\omega t)\, dt \tag{2.18}$$

that, for small flip angles, is nearly identical to the Bloch simulated distribution $\breve{A}(\omega) \approx \widetilde{A}(\omega)$. For symmetric RF pulses A(t), the normalized real part of its Fourier transform can be utilized as the frequency-dependent excitation profile $\widetilde{p}(\omega) \propto \mathrm{Real}\left\{\widetilde{A}(\omega)\right\}$. For linear slice selection gradients, the frequency $\omega$ is proportional to the spatial dimension $z$ in the slice direction $\omega \propto z$, and a reparametrization of $\widetilde{p}(\omega)$ can be performed to obtain a $z$-dependent excitation profile $p(z)$. The flip angle distribution $\alpha(z)$ can be obtained by scaling $p(z)$ such that its central maximum has the value of the nominal flip angle $\alpha_0$. Figure 2.5b shows the perfect rectangular excitation profile of an ideal sinc pulse (black dotted line) and the imperfect, non-rectangular excitation profile of the Hanning-filtered sinc pulse obtained using Eq. 2.18 (red solid line) for a nominal flip angle of $\alpha_0 = 7°$.

## 2.10 Dictionary Learning in MR Relaxometry

Dictionary learning methods are a new and promising way of efficiently approximating a signal of dimension $N$ by a linear combination of predefined signal prototypes [77]. $L$ of these model signals $\boldsymbol{d}$ - the so-called atoms - are typically combined to form an new basis $\boldsymbol{D} = [\boldsymbol{d}_1, \boldsymbol{d}_2, ..., \boldsymbol{d}_L] \in \mathbb{R}^{N \times L}$, in which each signal $\boldsymbol{x}$ can be represented by means of the dictionary:

$$\boldsymbol{x} = \boldsymbol{D}\, \gamma_s \,. \tag{2.19}$$

$\gamma_s$ is a vector containing the weighting coefficients of the linear combination of dictionary elements, the so-called sparse representation of $\boldsymbol{x}$. To find the sparsest $\gamma_s$, that is a $\gamma$ with as few non-zero coefficients as possible, the following sparse coding problem has to be solved:

$$\gamma_s = \underset{\gamma}{\operatorname{argmin}} \|\boldsymbol{x} - \boldsymbol{D}\gamma\|_2^2 \quad \text{subject to} \quad \|\gamma\|_0 \leq Q\,. \tag{2.20}$$

Here, $\|\cdot\|_0$ is the $l^0$ pseudo-norm which counts the non-zero entries and therefore constraints the sparse representation $\gamma$ to a maximum number of $Q$ elements. The $l^2$ norm or the difference between the initial signal vector and the sparse representation of the signal has to be minimized with respect to such constraints.

The solution of Eq. 2.20 has been extensively studied over the past years, and a wide range of algorithms have been proposed. In this work, an **O**rthogonal **M**atching **P**ursuit (OMP) algorithm which was presented in [78] was used to solve Eq. 2.20 and obtain the desired sparse representation $\gamma_s$ of the signal vector $\boldsymbol{x}$.

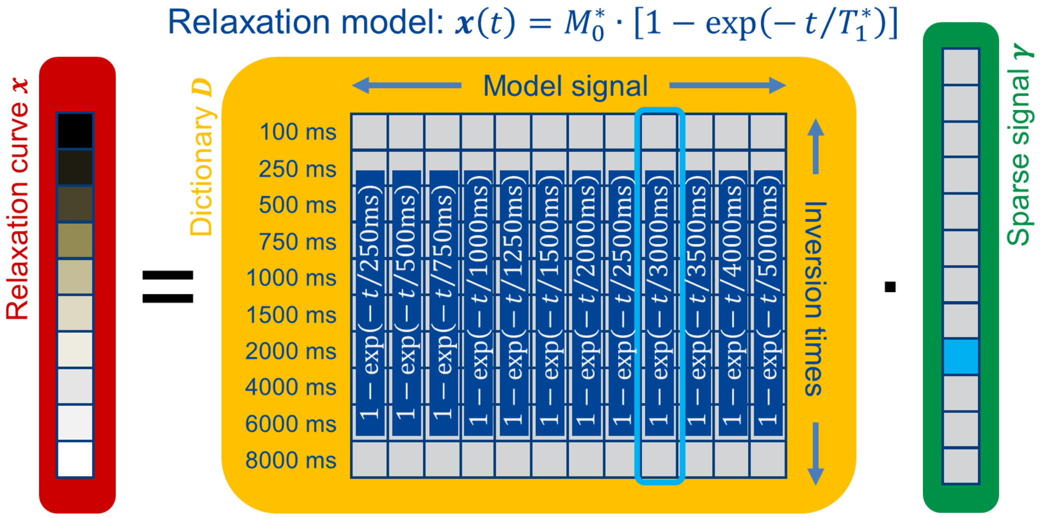

**Figure 2.6:** Exemplary dictionary for a SR-LL FLASH $T_1$ mapping experiment which is modeled by Eq. 2.10 for a relaxation curve $x$ acquired at $N = 10$ saturation times $T_S$ between 100 ms and 8000 ms, which is modeled for $L = 12$ different parameter sets with 250 ms $\leq T_1^* \leq$ 5000 ms. The blue box corresponds to a signal with $T_1^* = 3000ms$ which can be expressed by a sparse vector with only one element unequal to zero.

While the dictionary-based sparse coding approach is already widely used in many other science fields such as image [28] and audio processing [73], it was only recently applied for MR relaxometry [25]. In this case, the signal vector $\boldsymbol{x}$ is a relaxation curve which is sampled at $N$ multiple time points after magnetization preparation. The dictionary consists of potential relaxation curves that are precalculated using the respective relaxation model with $L$ different parameter sets. Therefore, the dimension of the dictionary is $N \times L$.

An exemplary dictionary for a SR-LL FLASH experiment is given in Figure 2.6. In this case, Eq. 2.10 is used for modeling a relaxation curve $\boldsymbol{x}$ acquired at $N = 10$ saturation times $T_S$ between 100 ms and 8000 ms with $L = 12$ different parameter sets with $250\,\text{ms} \leq T_1^* \leq 5000\,\text{ms}$. As described above, Eq. 2.20 can be solved using i.e. an OMP algorithm to obtain a sparse representation of the signal $\boldsymbol{x}$ in terms of a linear combination of a maximum of $Q$ dictionary elements. In other words, the dictionary can be used in conjunction with the OMP algorithm to find a maximum of $Q$ dictionary elements (corresponding to different parameter sets $(M_0, M_0^*, T_1^*)$) best describing the given relaxation curve. For $Q = 1$, the dictionary fit corresponds to a fit of Eq. 2.10 for a predefined set of possible solutions. It should be noted that while a major part of the relaxation model is represented by the dictionary $\boldsymbol{D}$, part of the modeled relaxation curve is always expressed by the sparse representation $\gamma_s$. As an example, the dictionary for a SR-LL FLASH consists of a set of multiple relaxation curves of potential parameters $T_1^*$, while the parameter $M_0^*$ is set to 1 in the generation of the dictionary. After the solution of Eq. 2.20, $M_0^*$ is represented by an element of the sparse vector $\gamma_s$.

The advantage of a dictionary-based fitting method is that any signal model, even relaxation models that are much more complicated than the two-parameter model of Eq. 2.10 or even the three-parameter model of Eq. 2.8, can be used to build up a dictionary, while a standard nonlinear least-squares fit such as for example a Levenberg-Marquardt method [57] might lead to a high computational complexity. Additionally, a fit of $Q > 1$ corresponds to a multi-exponential relaxation model which can for example be helpful to overcome partial volume effects in many parametric mapping applications. Again, a nonlinear least-squares fit of a multi-exponential function would lead to a considerable increase in computational complexity in these cases.

However, it should also be mentioned that the duration needed for a solution of Eq. 2.20 using the OMP algorithm largely depends on the size of the dictionary $\boldsymbol{D}$. As the dictionary size grows with the complexity of the model, complex relaxation models such as the model of a multi-parametric fit would not only require long computation times, but would also be highly demanding on the working memory of the reconstruction computer. Another disadvantage is that a dictionary-based fit highly depends on the accuracy of the model used for precalculating the dictionary and the range of parameters used. If, for example, only $T_1$ values in the range of $0\,\text{s} \leq T_1 \leq 1\,\text{s}$ were used in the design of the dictionary, a curve with an underlying $T_1$ of 2 s could not be solved and fitting errors would occur instead.

## 2.11 A Sign-dependent Sum of Squares Approach for Coil Combination

In an MRI measurement, data collection is usually performed with multiple receiver elements of small dimension. While the additionally obtained spatial information can be used to accelerate the data acquisition, the smaller winding diameter of the receiver coils leads to an increase in SNR compared to a volume coil. The complex signal intensity $I_\xi(x)$ in pixel $x$ that is received in receiver coil $\xi$ can be modeled by

$$I_\xi(x) = c_\xi(x) \cdot I(x) \,, \tag{2.21}$$

where $C_\xi$ describes the complex coil sensitivities that are superimposed on the underlying signal intensity $I(x)$. If no information is encoded in the phase of the signal (as for example in phase contrast imaging), these single-channel signals are usually combined using the square root of the **S**um **o**f **S**quares (SoS)

$$I_{\text{combined}}(x) = \sqrt{\sum_{\xi=1}^{N_c} |I_\xi(x)|^2} \,, \tag{2.22}$$

where $N_c$ is the number of receiver elements. The phase is destroyed in that process, which is of no consequence if images without any temporal variations in the sign are to be reconstructed. In a $T_1$ mapping experiment, however, the images of different contrasts are used to monitor the relaxation behavior after a suitable magnetization preparation. In this case, the sign of the magnetization can change during the period of the relaxation, which has to be respected in the coil combination. As an example, the signal after an inversion starts at $-M_0$, passes through zero during the relaxation and eventually arrives back at the equilibrium $M_0$.

To obtain one coil-combined model image $I(x,t)$ which depicts the relaxation behavior without losing any information of the sign, the complex-valued signal intensities of all coils can be combined using a sign-dependent SoS approach. In the following, a phase map $\varphi_\xi(x)$ for each location $x$ and coil $\xi$ has to be known. This can for example be calculated from later images of the relaxation process where the signal has already passed the phase-change at the zero-crossing. With this phase map, a real-valued intensity curve for each coil $\xi$ can be obtained by taking the real part of the complex-valued magnetization $I_\xi(x,t)$ after a rotation to the real axis:

$$I_{\text{Real},\xi}(x,t) = \text{Real}\left\{I_\xi(x,t) \cdot \exp(-i\varphi_\xi(x))\right\} \,. \tag{2.23}$$

To combine these relaxation curves for all $N_c$ coils, a sign-dependent SoS was then calculated using

$$I_{\text{combined}}(x,t) = \text{sign}\left(\theta(x,t)\right) \cdot \sqrt{|\theta(x,t)|} \,,$$

where

$$\theta(x,t) = \sum_\xi \left[\text{sign}\left(I_{\text{Real},\xi}(x,t)\right) \cdot |I_{\text{Real},\xi}(x,t)|^2\right] \,. \tag{2.24}$$

These coil-combined but still real-valued images can be used for further image processing.

Alternatively, the coil combination can be performed using the SoS of Eq. 2.22 if the absolute value of the relaxation model is used for the least-squares fit. As an example, the relaxation for an IR-LL FLASH sequence would change to:

$$M_{\mathrm{ABS}}(t) = |M(t)| = |M_0^* - (M_0 + M_0^*) \cdot \exp(-t/T_1^*)| \ . \tag{2.25}$$

Although this model can, in general, be used for a determination of $T_1$, the fitting method can lead to problems in the presence of noise. While noise is initially equally distributed above and below the course of the underlying relaxation curve, building the absolute value results in a positive bias of the magnetization in the area around the zero-crossing, potentially impairing the fitted $T_1$ values.

## 2.12 Gadolinium-based Contrast Agents

Water-soluble, paramagnetic contrast agents (usually metal chelates with multiple unpaired electrons) work by shortening both the $T_1$ and the $T_2$ relaxation time of surrounding water protons [13, 72, 92]. As an example, the gadolinium-based gadobutrol (Gd-DO3A-butrol) **C**ontrast **A**gent (CA) consists of a gadolinium(III) ($Gd^{3+}$) ion (the MRI active part) and a chelating carrier molecule (which is not MRI active) that is added to ensure the excretion of the CA via the renal system. Gadolinium is a lanthanide metal ion with seven unpaired electrons that very effectively enhances proton relaxation due to its high magnetic moment and very labile water coordination [13,23,98,109]. This leads to a shortening in $T_1$ and $T_2$ in surrounding water protons that may, in turn, produce the signal-enhancing effect. As the $T_1$ effect tends to dominate at standard clinical doses of 0.1-0.2 mmol/kg, these paramagnetic CAs are typically used to enhance the signal in $T_1$-weighted images [13].

The administration of CA with a concentration $C$ [mmol/l] results in shorter relaxation times $T_1'$ and $T_2'$, which can be described by [31, 37]:

$$\frac{1}{T_1'} = \frac{1}{T_1} + R_1 \cdot C \quad \text{and} \quad \frac{1}{T_2'} = \frac{1}{T_2} + R_2 \cdot C \ . \tag{2.26}$$

Gadobutrol is marketed by the Bayer Schering Pharma AG (Berlin, Germany) as Gadovist®, which was used as CA in all DCE-MRI acquisitions performed in this work. 1 ml of Gadovist® contains 1 mmol of gadolinium. According to [4], the relaxivities $R_1$ and $R_2$, as determined from the shortening of the spin-lattice relaxation time $T_1$ and the spin-spin relaxation time $T_2$ are about

$$R_1 = 3.58 \left[\frac{\mathrm{l}}{\mathrm{mmol} \cdot \mathrm{s}}\right] \quad \text{and} \quad R_2 = 3.99 \left[\frac{\mathrm{l}}{\mathrm{mmol} \cdot \mathrm{s}}\right] \ . \tag{2.27}$$

## 2.13 SR-LL FLASH Sequences after the Admission of Contrast Agent

Section 2.6 introduced Eq. 2.11 for describing the relaxation behavior of an SR-LL FLASH sequence under the assumption of a perfect SR pulse, that is $M(t_0) = 0$. To extend this model for DCE-MRI, Eq. 2.26 describing the relaxation times $T_1'$ and $T_2'$ after the administration of CA of a concentration $C$ has to be substituted into Eq. 2.11, leading to [48]:

$$\begin{aligned}
M'(n) &\quad\rightarrow\quad M(n,C) \\
M' = M_0 \cdot \sin(\alpha) \cdot e^{-T_E/T_2^{*\prime}} &\quad\rightarrow\quad M(C) = M_0 \cdot \sin(\alpha) \cdot e^{-T_E/T_2^*} \cdot e^{-T_E R_2^* C}, \\
{E_D}' = e^{-T_D/{T_1}'} &\quad\rightarrow\quad E_D(C) = e^{-T_D/T_1} \cdot e^{-T_D R_1 C}, \\
{E_1}' = e^{-T_R/{T_1}'} &\quad\rightarrow\quad E_1(C) = e^{-T_R/T_1} \cdot e^{-T_R R_1 C}, \\
a' = \cos(\alpha) \cdot {E_1}' &\quad\rightarrow\quad a(C) = \cos(\alpha) \cdot E_1(C)\,. 
\end{aligned} \tag{2.28}$$

Assuming a short echo time $T_E$, the change in signal intensity due to the CA injection can be described as

$$\begin{aligned}
\Delta(n,C) &= M(n,C) - M(n,0) \\
&\approx M \cdot a^{n-1} \cdot \left( E_D - \frac{E_1 - a}{1-a} \cdot \frac{1 - e^{-(T_S - T_D) R_1 C}}{1 - e^{-T_S R_1 C}} \right) \cdot \left(1 - e^{-T_S R_1 C}\right),
\end{aligned} \tag{2.29}$$

where $T_S = T_D + (n-1) T_R$ is the saturation time between the end of the SR preparation pulse and the $n$-th RF excitation pulse of the FLASH acquisition.

## 2.14 Myocardial First-pass Perfusion Imaging

**D**ynamic **C**ontrast-**E**nhanced **MRI** (DCE-MRI) is one of the most useful tools to evaluate myocardial perfusion using MRI [2, 34]. After the intravenous injection of a signal-enhancing (usually gadolinium-based) CA, the passage of the bolus through the desired anatomical slice is imaged over multiple consecutive heartbeats. In myocardial first-pass perfusion DCE-MRI, imaging is typically performed in the short heart axis view. To minimize artifacts due to respiratory motion, the entire acquisition is performed in breath-hold. In addition, the start of the imaging sequence in each heartbeat is triggered by an **E**lectro**C**ardio**G**ram (ECG) to ensure that the entire time series is acquired in the same phase of the cardiac cycle (typically within a temporal window of ~ 200 ms to freeze cardiac motion). A saturation recovery magnetization preparation is applied at the start of each image acquisition to ensure the same $T_1$-weighted contrast for every heartbeat. The acquisition scheme of a cardiac DCE-MRI measurement is illustrated in Figure 2.7.

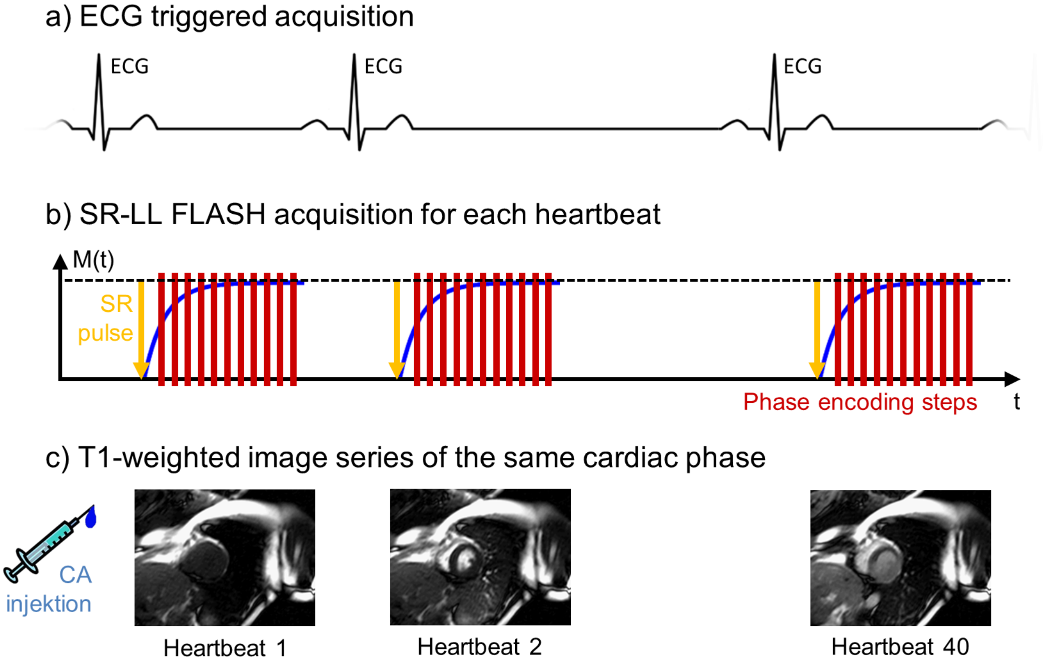

**Figure 2.7:** Acquisition scheme of a myocardial first-pass perfusion measurement. After the injection of CA, an ECG-triggered (a) SR-LL FLASH sequence (b) is applied over ~ 200 ms in diastole to minimize cardiac motion. By acquiring one image in each heartbeat, an image series of the CA passage can be generated (c).

As described in section 2.12, the CA is carried into the tissue of interest by the inflowing blood. As the CA enhances the signal intensity in perfused regions of the myocardium, a series of short axis views acquired after the administration of CA visualizes myocardial regions with reduced perfusion. This enables the diagnosis of coronary artery disease and myocardial ischemia using DCE-MRI [1, 79]. As the first pass of the CA through the myocardium occurs over a very short time span of about 10 s, very fast imaging sequences such as the SR-LL FLASH sequence described in section 2.6 are typically applied in myocardial first-pass perfusion imaging.

## 2.15 Quantification of Myocardial Perfusion Using DCE-MRI

The evaluation of a myocardial first-pass perfusion MRI measurement, as it was described in the previous section, is most often performed visually based on the reconstructed time series of $T_1$-weighted images (see Fig. 2.7c). Alternatively, a quantitative estimation of the **M**yocardial **B**lood **F**low (MBF) promises a more objective and unbiased analysis of the data, which could be advantageous in many clinical settings.

If the native $T_1$ value of the tissue before the CA injection as well as the altered ${T_1}'$ values during the pass of the CA were precisely known, Eq. 2.26 could be used to obtain the temporal evolution of the CA concentration $C$ and consequently quantify the perfusion. However, as the acquisition time of each image is limited to ∼ 200 ms, a determination of $T_1$ is not feasible. Instead, $T_1$ is typically estimated from the change $\Delta(C) = M(C) - M(0)$ in signal intensity due to CA injection, which is referred to as **A**rterial **I**nput **F**unction (AIF) in the blood pool and **T**issue **E**nhancement **C**urve (TEC) in the myocardial tissue.

In order to obtain TECs from a first-pass perfusion image series, the following steps are typically performed:

1. **Motion correction:** First, a motion correction is applied to obtain an image series where the structures of the individual frames correspond as closely as possible.
2. **Segmentation:** Next, these images are segmented into six myocardial sectors, according to the American Heart Association [12].
3. **Partial volume correction:** Left and right ventricle have a signal which is relatively high compared to the myocardial signal. Therefore, partial volume effects can alter the signal especially in the voxels near the endocardial border, which partially consist of myocardial tissue and blood of one of the ventricles. To correct for these effects, a partial volume correction has to be carried out in each of the six sectors.
4. **Baseline correction:** $B_1$ inhomogeneities and spatially varying coil sensitivities result in a variation of the signal amplitude across the FoV. Therefore, a baseline correction has to be performed using the initial frames, i.e. before the CA injection.

The AIF is determined by placing a left-ventricular **R**egion **o**f **I**nterest (RoI) in the motion-corrected image series.

As described in section 2.13, the relation between $\Delta(C)$ (i.e. TEC and AIF) and the concentration $C$ is given by

$$\Delta(C) = M(C) - M(0) \propto (1 - e^{-T_S R_1 C}) \,. \tag{2.30}$$

For $T_S R_1 C \ll 1$, a first-order Taylor series results in the linear relation

$$\Delta(C) \propto (1 - e^{-T_S R_1 C}) \quad \xrightarrow{T_S R_1 C \ll 1} \quad \Delta(C) \propto T_S R_1 C \,, \tag{2.31}$$

and the CA concentration $C$ can be directly determined from the change in signal intensity without an explicit conversion to gadolinium concentration. As the relaxivity $R_1$ is inherent to the CA used, the condition $T_S R_1 C \ll 1$ is only fulfilled if either $C$ is very small or $T_S$ is very short:

- A small $C$ corresponds to a low dose injection of CA. However, as the CA leads to an enhanced MRI signal only in the relatively small blood fraction of the myocardial tissue, a smaller dose of CA leads to a deterioration of the SNR in the myocardium. While the SNR could be highly improved using a higher dose of CA, it would lead to saturation effects especially in the blood pool, and Eq. 2.31 would no longer hold.

- A short $T_S$ can be reached by acquiring the image as soon as possible after the SR pulse. As the signal is zeroed by the saturation magnetization preparation, this likewise results in a poor SNR of the reconstructed images. Again, longer saturation times $T_S$ could be used to improve the SNR, but the linear relationship between $\Delta(C)$ and $T_S$ would no longer hold.

The most important ways of obtaining both an unsaturated AIF as well as a TEC of high SNR are:

- Dual-bolus methods [15, 16, 44, 55] consist of two separate first-pass perfusion acquisitions with two different CA doses. First, an unsaturated AIF (prebolus) is obtained from a low dose scan and scaled depending on the CA difference between the two acquisitions. Next, TECs with good SNR are obtained from a high dose injection. Combining the scaled unsaturated AIF of the low dose scan with the TECs of the high dose scan, the perfusion can be quantified. In addition to the extended scan time, the main disadvantage of dual-bolus methods is that the two injections may reflect different physiological states, particularly during vasodilation [51].

- In the second approach [33, 49], only one high dose CA injection is applied, and two images of different saturation times $T_S$ are acquired in each heartbeat. First, an image of a very short $T_S$ is acquired as soon as possible after the SR pulse (it typically consists of only a few k-space lines). Although this image has a very low spatial resolution, the blood pool is usually large enough for the determination of an AIF. The very short $T_S$ ensures that the condition $T_S R_1 C \ll 1$ is fulfilled despite the high CA dose, and that the AIF can be assumed to be unsaturated. In the remaining acquisition period, a second, well-resolved image of a good SNR is acquired, and the TECs are obtained from this dataset. A main disadvantage is that the saturation time $T_S$ has to be short enough for the condition $T_S R_1 C \ll 1$ to hold, greatly restricting the acquisition time available for the first low resolution image. Additionally, the already short acquisition time of ~ 200 ms is further reduced by the time required for acquiring the unsaturated image. Another potential source of error are imperfect saturation pulses with $M(t_0) \neq 0$, which lead to errors in the linear approximation of Eq. 2.31.

- In [48], an alternative method for estimating $T_1$ and thus gadolinium concentration from one high dose injection was proposed. The method applies a radial SR-LL FLASH sequence for image acquisition. For a radial acquisition, each projection equally contributes to the reconstructed image's contrast, and the acquired projections can be divided into four sub-images of different effective saturation times $T_{S,\mathrm{eff}}$. As the first sub-image has a relatively short $T_{S,\mathrm{eff}}$ of ~ 50 ms, it can be used to determine an unsaturated AIF. In contrast, the image of the longest effective $T_{S,\mathrm{eff}}$ has the highest SNR and can be used to obtain the TECs. Although an effective saturation time $T_{S,\mathrm{eff}}$ of ~ 50 ms is relatively short, it can still be considerably too long for the condition of $T_S R_1 C \ll 1$ to hold especially for short relaxation times $T_1$ or, equivalently, large relaxivities $R_1$ as they occur in DCE-MRI.

After all corrections have been carried out, the resulting TECs of all sectors can be deconvolved using the AIF with the constraint of a Fermi function as residuum to obtain absolute MBF values in ml $\mathrm{g}^{-1}$ $\mathrm{min}^{-1}$ (see [47] for a more detailed description).

## 2.16 Quantification of Myocardial Perfusion Using Arterial Spin Labeling

As described in the previous section, myocardial perfusion of the human heart is typically measured by tracking the first pass of an exogenous CA. In small animals, however, the fast heart rate ($>$ 600 bpm in mice) limits the ability to track a CA bolus with the required temporal resolution. Additionally, MBF values of small animals are typically 5 times higher than in humans, which further complicates contrast-enhanced first pass perfusion measurements. Alternatively, **A**rterial **S**pin **L**abeling (ASL) is a non-invasive method that provides quantitative measurements of tissue blood flow. As the ASL signal is directly proportional to the MBF, it is typically used for the quantification of myocardial perfusion in small animals.

The most common methodological approach is a **F**low sensitive **A**lternating **I**nversion **R**ecovery (FAIR) preparation combined with an ECG-gated LL FLASH acquisition scheme [5, 54, 89, 99]. In a FAIR-LL FLASH acquisition, which is schematically illustrated in Figure 2.8, two $T_1$ measurements are performed, following a **GL**obal (GL) and a **S**lice-**S**elective (SS) inversion (Fig. 2.8a). In the SS case, non-inverted spins will flow into the imaging slice in which the magnetization has been inversed, altering the apparent relaxation times $T_1^*$ in the relevant voxels. After a separate fit of the image series of both acquisitions (Fig. 2.8b-c) as described in section 2.5, the resulting $T_1$ values (Fig. 2.8d) can be combined to estimate the perfusion value $P$ [54] (Fig. 2.8e):

$$\frac{P}{\lambda} = \frac{T_1^{\mathrm{GL}}}{T_1^{\mathrm{blood}}} \left( \frac{1}{T_1^{\mathrm{SS}}} - \frac{1}{T_1^{\mathrm{GL}}} \right) . \tag{2.32}$$

$T_1^{\mathrm{GL}}$ and $T_1^{\mathrm{SS}}$ stand for the global and slice-selective $T_1$ value, $T_1^{\mathrm{blood}}$ denotes an average $T_1$ measured in a RoI in the left ventricular cavity and $\lambda$ is the blood/tissue partition

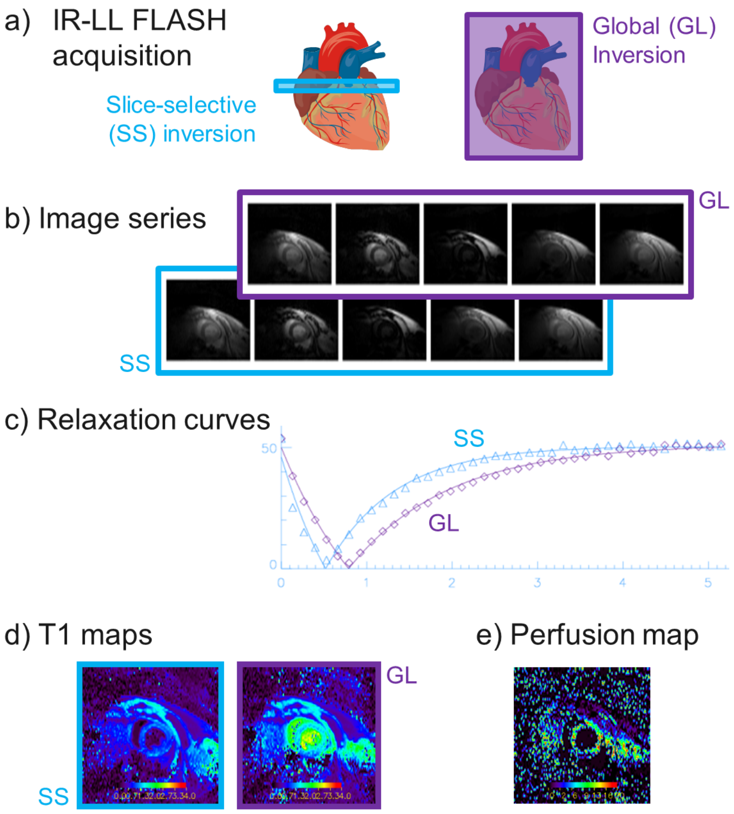

**Figure 2.8:** Acquisition scheme of an Arterial Spin Labeling experiment. a: FAIR-LL FLASH acquisition with slice-selective (SS) and global (GL) inversion. b: Resulting image series. c: Relaxation curves in an exemplary myocardial RoI. d: Fitted $T_1$ maps. e: Calculated perfusion map.

coefficient of water (e.g. 0.83 ml g$^{-1}$ for rat myocardium [3]). As a precise description of the relaxation process and therefore a more accurate determination of $T_1$ will be the main focus in this work, the details of the quantification process will not be discussed further in this section. However, a more detailed description can be found in [54].

Although the fast heart rate of rodents enables a high sampling rate of the $T_1$ relaxation curve, it limits the acquisition to only one phase-encoding (i.e. one k-space line) per heartbeat if blurring by cardiac motion is to be avoided. After the inversion, the same phase encoding step is acquired for about 50 consecutive FAIR-LL FLASH inversion times. This acquisition is repeated with different phase encoding gradients until the entire k-space is covered, leading to long scan times of about 20-25 min. In the initial implementation [54], the inversion time of each of the ~ 50 resulting images was obtained as an average of the logged $T_I$ over all of the associated phase-encoding steps. A long scan time associated with variable heart rates can therefore cause inconsistencies in the $T_I$ used for the $T_1$ fitting process which has been addressed in [99]. While cardiac motion is minimized by ECG-gating of each phase encoding step, artifacts caused by respiratory motion are visually excluded after the entire acquisition is completed.

# 3 Model-based Acceleration of Parameter Mapping (MAP)

## 3.1 Introduction

As mentioned in sections 2.4 to 2.6, one of the most prominent ways to perform $T_1$ mapping is to track the spin-lattice relaxation process after a suitable magnetization preparation. For short relaxation times, however, it can be difficult to cover the entire relaxation process using only one magnetization preparation. Instead, the acquisition often has to be performed in a segmented fashion, leading to long scan times. If the scan time is to be limited, the spatial resolution has to be lowered, impairing the clinical relevance of this promising technique for many clinical applications [18, 88, 94].

In the previous years, model-based reconstruction techniques based on the mathematical theory of compressed sensing [11, 26] have become an increasingly popular field of research. In a compressed sensing reconstruction, images can be recovered from incoherently undersampled k-space data by exploiting sparsity in any known transform domain. In addition to commonly used sparse transform domains such as the wavelet [60] or $x$-$f$ domain [32], more specific sparsifying transforms such as the exponential relaxation parameter spaces of $T_1$ and $T_2$ after a suitable magnetization preparation have been used to obtain images and parameter maps from undersampled k-space data [8, 25, 90].

In this work, a **M**odel-based **A**cceleration of **P**arameter mapping (MAP) technique is presented, capable of fully resolving an exponential signal evolution from a dataset acquired after a single magnetization preparation. The technique was initially presented for saturation recovery prepared, radially acquired Look-Locker datasets [94] and subsequently implemented for inversion recovery prepared datasets [96]. It was finally used for acceleration of various applications such as DCE-MRI of the human heart [86] and brain [53, 93] or arterial spin labeling in small animals [95], each of which will be described in a separate section. This section therefore focuses mainly on the principle of the MAP algorithm.

## 3.2 The MAP Reconstruction Scheme

The principle of the MAP algorithm is to use the contrast information in a set of k-space lines acquired after a suitable magnetization preparation in conjunction with an expected relaxation model to fill the missing parts of k-space that were not acquired during the acquisition.

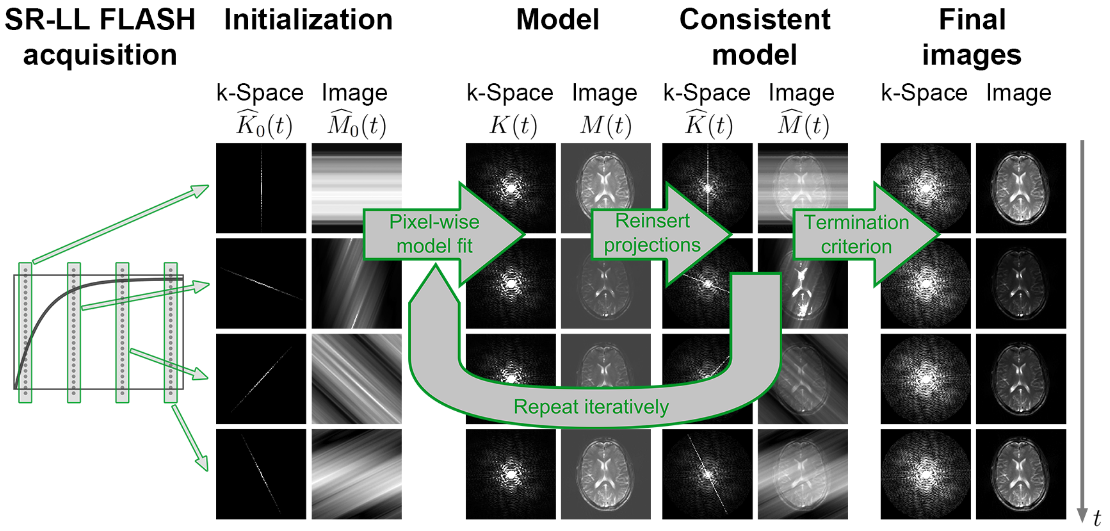

**Figure 3.1:** MAP reconstruction scheme. Modified Figure from [94].

A set of $n_p$ radial projections with $n_r$ readout points per projection acquired in a single SR-LL FLASH acquisition (see section 2.6) will be used to demonstrate the individual steps involved in the MAP reconstruction algorithm (see Fig. 3.1). Therefore, Eq. 2.10 in section 2.6 will be used as relaxation model:

$$M(t) = M_0^* \cdot \left[1 - \exp(-t/T_1^*)\right] \ .$$

First, the algorithm is initialized by gridding each non-Cartesian projection on a separate Cartesian grid using self-calibrating GROG (see section 2.2). Each of the $n_p$ resulting grids carries information about the contrast at one specific saturation time $T_S$ after the SR preparation pulse. These highly undersampled k-spaces $\widehat{K}_0(t)$ are used for the first iteration, each of which consists of the following steps:

1. Inverse discrete Fourier transform of the current consistent model k-spaces $\widehat{K}(t)$ into image space $\widehat{M}(t)$ (first iteration: $\widehat{K}_0(t)$, $\widehat{M}_0(t)$).
2. Pixel-wise fit of Eq. 2.10, yielding $T_1^*$ and $M_0^*$ in every pixel. This corresponds to one 2D model image $M(t)$ for every time point t.
3. Discrete Fourier transform to generate the corresponding model k-spaces $K(t)$.
4. Ensure data consistency: Substitute measured data for the model data for all acquired projections and zero the model k-space at all points where no information is acquired for all $T_S$, i.e. in the edges of the Cartesian grid that are not covered by the radial sampling pattern. This results in the consistent model k-spaces $\widehat{K}(t)$ that are passed on to the next iteration.

This reconstruction scheme is illustrated in Figure 3.1. It should be mentioned that $M$ and $K$ describe the *model* obtained by a fit of the relaxation model (Eq. 2.10), whereas $\widehat{M}$ and $\widehat{K}$ stand for the *consistent model*, i.e. after the substitution of the original data in the data consistency step 4 of the algorithm.

A minimum difference between model k-spaces $K(t)$ and consistent model k-spaces $\widehat{K}(t)$ or simply a fixed number of iterations can serve as termination criterion. The result is one parameter set $[T_1^*,\ M_0^*]$ for each pixel of the acquired FoV which can be depicted in a spatially resolved map to describe the local relaxation behavior.

## 3.3 Improvement of the Initial Estimates

In the reconstruction scheme described above, the gridded k-spaces of the single projections are simply used as initial estimates $\widehat{K}_0(t)$ in the first iteration of the MAP algorithm. To improve the convergence behavior of MAP (i.e. less iterations are needed to reach the termination criterion and local minima are avoided as solutions), these "nearly empty" k-spaces can be "filled" by a linear interpolation of all acquired k-space points through time before they are passed on to the first iteration. Using these new estimates $\widehat{K}_0(t)$ for the initialization of MAP can greatly improve the time-efficiency of MAP.

## 3.4 Relaxation Models and Fitting Algorithms Used in MAP

In principle, any model can be used to describe the relaxation curve obtained in the respective acquisition. A very accurate relaxation model translates into a high accuracy in the reconstructed parameter maps. If a rather simple two- or three-parameter model as described in sections 2.4 to 2.6 is used as relaxation model, a straightforward least-squares fit can be used in step 2 of the algorithm to obtain the parameter set best describing the relaxation behavior. Alternatively, a more complicated yet more appropriate model such as the **C**onsideration of **S**lice **P**rofiles (CSP) model which will be introduced in section 8.2 can be used as relaxation model. In this case, the least-squares fit has to be replaced by a dictionary-based fitting approach as described in section 2.10.

Dictionary-based fitting can also be used to sensitize the relaxation model to the influence of a multi-exponential relaxation, which can occur in voxels containing multiple different tissue types. For this purpose, the maximum number of coefficients $K$ in Eq. 2.20 that is permitted for the sparse representation of the signal has to be set to the desired number of atoms or, equivalently, tissue types. As described in section 2.10, a least-squares approach for such a multi-exponential relaxation model would lead to a considerable increase in computational complexity.

A dictionary-based fitting algorithm where only one atom is used to describe the relaxation signal (that is $K=1$) results in one parameter set that was used for calculating the respective dictionary atom and therefore leads to the same results as a least-squares fit of the respective relaxation model.

## 3.5 Using MAP with Multiple Receiver Coils

Most clinical MRI systems are equipped with multi-channel phased-array coils for signal reception. Therefore, the sensitivities of the individual receiver channels have to be included in the reconstruction scheme of section 3.2.

As described in section 2.11, the sensitivity profiles $c_\xi(x)$ received in coil $\xi$ at pixel $x$ have to be included in the image reconstruction for an acquisition with multiple receiver channels (Eq. 2.21 with $I \rightarrow M$):

$$M_\xi(x,t) = c_\xi(x) \cdot M(x,t)\ . \tag{3.1}$$

In case of a relaxation curve, the signal can have a positive or a negative sign. Therefore, a sign-dependent coil combination as described in section 2.11 has to be used for a combination of the individual coil signals (Eq. 2.24 with $I \rightarrow \widehat{M}$):

$$\widehat{M}_{\text{combined}}(x,t) = \text{sign}\left(\theta(x,t)\right) \cdot \sqrt{|\theta(x,t)|}\ ,$$

where

$$\theta(x,t) = \sum_\xi \left[\text{sign}\left(\widehat{M}_{\text{Real},\xi}(x,t)\right) \cdot \left|\widehat{M}_{\text{Real},\xi}(x,t)\right|^2\right]\ . \tag{3.2}$$

The resulting real-valued relaxation curves can be used for the pixel-wise fit that is performed in step 2 of the algorithm, resulting in the coil-combined signal model $M_{\text{combined}}(x,t)$ in each pixel $x$.

To perform the data consistency step 4 of the algorithm and substitute the measured data into the current model datasets, $M_{\text{combined}}(x,t)$ has to be re-separated into single-coil relaxation curves $M_\xi(x,t)$. The complex coil sensitivity factor $c_\xi(x)$ describes how the fitted signal model $M_{\text{combined}}(x,t)$ is divided into real and imaginary part of a single-coil model image $M_\xi(x,t)$. Therefore, $c_\xi(x)$ was calculated separately for each coil $\xi$ by applying a least-squares approach of Eq. 3.1 to the current consistent model images $\widehat{M}_\xi(x,t)$. Finally, the resulting complex-valued model images $M_\xi(x,t)$ were Fourier transformed into k-space (step 3 of the algorithm), where the data consistency was performed to obtain new consistent model k-spaces $\widehat{K}_\xi(x,t)$ for the next iteration (step 4 of the algorithm).

# 4 MAP with Saturation Recovery Magnetization Preparation

## 4.1 Introduction

In this chapter, an implementation of the MAP algorithm presented in chapter 3 for $T_1^*$ mapping using a saturation recovery prepared Look-Locker FLASH sequence is presented. The adjusted algorithm will be called **S**aturation **R**ecovery **MAP** (SR-MAP) in the following.

A majority of the content of this chapter has been published in [94]. The permission to reuse images and text from this publication was granted by *John Wiley and Sons*. Reused Figures and Tables are marked in the captions.

## 4.2 Implementation of SR-MAP

The implementation of MAP which is described in this chapter uses a radial dataset obtained in a single-preparation SR-LL FLASH acquisition (see section 2.6) as input. Therefore, the relaxation process after the SR pulse can be modeled by Eq. 2.10.

The "nearly empty" k-spaces obtained by gridding the single projections into separate k-spaces as described in section 3.2 were used as initial estimates $\widehat{K}_0(x,t)$ for the first iteration.

The changes in each step of the reconstruction scheme described in section 3.2 will be pointed out in the following. For reasons of clarity, the pixel index $x$ will be omitted.

1. As before, the current consistent model k-spaces $\widehat{K}_\xi(t)$ of all individual coils were Fourier transformed to obtain consistent model images $\widehat{M}_\xi(t)$.
2. Before the pixel-wise fit, the signals received in the different coils $\xi$ were combined using a SoS as described in section 2.11 (Eq. 2.22 with $I \to \widehat{M}(t)$):

$$\widehat{M}_{\text{combined}}(t) = \sqrt{\sum_{\xi=1}^{N_c} \left|\widehat{M}_\xi(t)\right|^2}\,. \tag{4.1}$$

As the signal after an SR preparation is expected to be positive for all saturation times $T_S$, the sign was not respected in that process. A pixel-wise least-squares fit of Eq. 2.10 was applied to obtain a combined model $M_{\text{combined}}(t)$ of all coils.

3. Before the backward transform, the model images $M_{\text{combined}}(t)$ had to be re-separated into one model image $M_\xi(t)$ for each coil which can be described by

$$M_\xi(t) = c_\xi \cdot M_0^* \cdot [1 - \exp(-t/T_1^*)] \ . \tag{4.2}$$

As $T_1^*$ was assumed to be coil-independent, the real and imaginary parts of the product $c_\xi \cdot M_0^*$ in each coil were determined separately by using a least-squares approach on Eq. 4.2. The resulting single-coil model images $M_\xi(t)$ were Fourier transformed to obtain single-coil model k-spaces $K_\xi(t)$.

4. As before, the data consistency was ensured by separately substituting the measured data of all acquired projections for the model data and by additionally zeroing the resulting consistent model k-spaces $\widehat{K}_\xi(t)$ at all pixels where no information was measured for all $T_S$.

The following termination criterion was used: As the intensity of the k-spaces is highly dependent on the saturation time $T_S$ after the SR pulse, a difference between model and consistent k-spaces would be strongly $T_S$-weighted. Therefore, the variation in the masked $T_1^*$ maps was used as termination criterion. As soon as the number of pixels without any change in $T_1^*$ for 10 subsequent iterations was decreasing, the algorithm was automatically stopped. In case this condition is not fulfilled within 1000 iterations, the algorithm is automatically terminated.

## 4.3 Methods

All imaging experiments were carried out on a 3 T whole-body scanner (MAGNETOM Trio, Siemens AG Healthcare Sector, Erlangen, Germany) employing a 12 channel phased-array head coil for signal reception.

All post-processing was performed on a standard desktop PC equipped with an Intel Core i7-2600 CPU (3.4 GHz) using MATLAB (The MathWorks, Natick, MA).

### 4.3.1 Numerical Simulations

To validate functionality and accuracy of the reconstruction algorithm, simulations were performed on a numerical phantom of matrix size $128 \times 128$ consisting of 4 compartments with longitudinal relaxation times $T_1^*$ of 180 ms, 250 ms, 340 ms and 600 ms. The magnetization $M_0$ was set to 1 within and 0 outside of these compartments and a phase $\varphi$ linearly changing in the interval $[\pi/2, 3\pi/2]$ was added. The relaxation process after SR magnetization preparation was simulated using Eq. 2.10 for 512 time steps $T_S$ in the range of [30 ms , 4118 ms] equally spaced with a repetition time $T_R = 8$ ms. Exemplary signal-time curves for one single coil of sensitivity $c = 1$ and $M_0^* = 1$ are depicted in Figure 4.1.

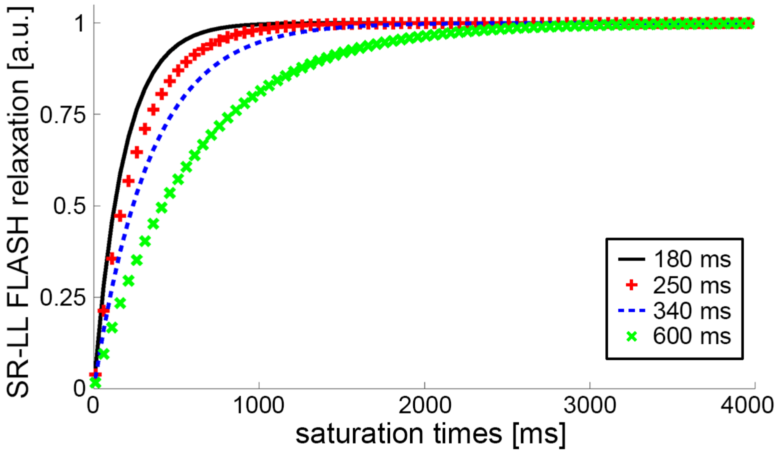

**Figure 4.1:** Exemplary SR-LL FLASH relaxation curves calculated using Eq. 2.10 for the $T_1^*$ values used in the numerical simulations. Modified Figure from [94].

To simulate a measurement with multiple receiver coils, sensitivities of an eight-element one-ring head coil array were derived using an analytic integration of the Biot-Savart equations [81] and applied to these images. The Cartesian k-spaces obtained by a discrete Fourier transform of the resulting images were then resampled as Golden Ratio [108] radial trajectory (projections: 512, readout points: 256, base matrix: 128 × 128) using sinc interpolation. Finally, Gaussian complex white noise with standard deviations ($\sigma_N$) of 0 (noiseless), 1.0, 2.5 and 5.0 in both real and imaginary part was added, corresponding to an SNR ranging from about 10, 4 and 2 for images at $T_S = 30$ ms up to about 200, 80 and 40 for images after complete relaxation ($T_S \sim 4000$ ms).

A maximum number of 1000 iterations of the proposed MAP algorithm was applied to reconstruct 512 images of various contrasts or, in other words, determine the parameter maps $T_1^*$ and $M_0^*$ for each of these datasets.

For an assessment of the quality of these reconstructions, a set of 512 Nyquist sampled reference datasets was created in the same way as the undersampled datasets described above and likewise gridded using self-calibrating GROG (see section 2.2).

### 4.3.2 Phantom Experiments

Phantom experiments were performed on a phantom consisting of 4 compartments with different concentrations of contrast agent (Gadovist®, Bayer Schering Pharma, Berlin, Germany) using a single-preparation SR-LL FLASH sequence (FoV: $200 \times 200 \times 8\,\text{mm}^3$, $T_R$: 6.8 ms, $T_E$: 3.1 ms, $\alpha_0$: 6°) with a Golden Ratio [108] radial k-space trajectory (projections: 512, readouts points: 128).

To assess the accuracy of these effective relaxation times, a fully sampled reference dataset was acquired for every time step $T_S$ by carrying out 512 separate measurements with a total scan time of more than 2 h compared to 3.6 s for the single-preparation measurement. In each of these measurements, the order of the acquired projections was shifted with respect to the previous one. By retrospectively reordering these projections, a complete dataset was reconstructed for each of the 512 time points, and a two-parameter fit of Eq. 2.10 to the SoS (Eq. 4.1) of the signals received in all coils was used to obtain a reference $T_1^*$ map.

To validate the functionality of the MAP algorithm, 1000 iterations of the MAP algorithm were applied to one of the 512 single-preparation datasets of the reference scan (scan time ~ 3.5 s), yielding $T_1^*$ and $M_0^*$ as results. A RoI analysis was used to compare the $T_1^*$ map of the reference to the one obtained from the MAP reconstruction. For comparison, mean values ($\mu$) and standard deviations ($\sigma$) of $T_1^*$ were calculated in every compartment.

### 4.3.3 In Vivo Measurements

All human in vivo studies were approved by our local ethics committee. They were performed on healthy volunteers, and written informed consents were obtained from the subjects prior to scanning.

Measurements of a human brain were carried out with the same sequence as in the phantom experiments (FoV: $220 \times 220 \times 8\,\mathrm{mm}^3$, $T_R$: 6.6 ms, $T_E$: 3.1 ms, $\alpha_0$: 6°, projections: 1024, readout points: 128). A set of 202 consecutive SR-prepared single-preparation datasets (scan time ~ 24 min) was acquired, corresponding to the Nyquist limit for a radial trajectory with 128 readout points per projection. By shifting the trajectory by one golden angle for each of these SR pulses and subsequently assigning all acquired projections to the appropriate time point $T_S$ of the relaxation process, Nyquist sampled reference images were reconstructed for each of the 1024 time points. Again, a two-parameter fit of Eq. 2.10 to the SoS of all coil signals was used to obtain a reference $T_1^*$ map.

As in the phantom studies, the MAP algorithm was applied to one of the 202 single-preparation datasets (scan time ~ 6.8 s) to obtain $T_1^*$ and $M_0^*$.

In addition, an IRFSE experiment (section 2.7) with a Cartesian k-space trajectory (FoV: $220 \times 220 \times 8\,\mathrm{mm}^3$, effective $T_E$: 7.6 ms, $\alpha_0$: 120°, echo train length: 32, base matrix: $128 \times 128$, total scan time ~ 23 min) was acquired for 24 different contrasts in the range of 100 ms to 8000 ms after the inversion. For a comparison of the effective relaxation parameters obtained by the MAP reconstruction ($T_1^*$, $M_0^*$) to this standard $T_1$ mapping method, the same slice was used for both measurements. A fit of Eq. 2.2 to the SoS of all coil signals was used to determine $T_1$ and $M_0$.

To facilitate a comparison between the $T_1^*$ maps of both the MAP reconstructions and the reference scan, a RoI analysis of typical **W**hite **M**atter (WM), GM, and **C**erebro**S**pinal

**F**luid (CSF) regions was performed. This analysis was repeated with the $T_1$ maps obtained from the IRFSE measurement for the same RoIs.

## 4.4 Results

### 4.4.1 Numerical Simulations

All reconstructions in this subsection were terminated after 1000 MAP iterations.

Figures 4.2-4.4 show results of the numerical simulations. Depicted are reconstructions of datasets featuring different noise levels after 1000 iterations of the MAP algorithm. In Figures 4.2 and 4.2, (a) corresponds to the Nyquist sampled reference dataset, whereas (b-e) are MAP images reconstructed from single-preparation datasets, including one noisefree dataset (b) as well as datasets with Gaussian white noise of standard deviation $\sigma_N = 1.0$ (c), $\sigma_N = 2.5$ (d), and $\sigma_N = 5.0$ (e).

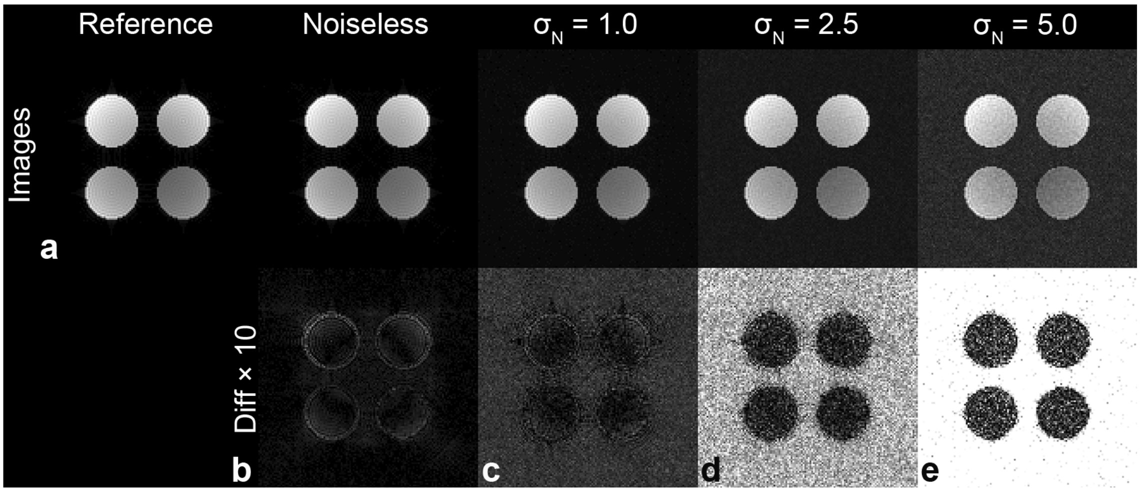

**Figure 4.2:** Numerical simulations. a-e: MAP reconstructed image spaces (top row) and a ten-fold difference from the reference (bottom row) for an exemplary time point $T_S = 502\,\text{ms}$ after 1000 iterations of the algorithm. Modified Figure from [94].

The upper part of Figure 4.2 shows images of one exemplary contrast at $T_S = 502\,\text{ms}$ after SR preparation. All images reveal Gibbs ringing artifacts at the boundaries. The reconstructions get noisier with $\sigma_N$ increasing. The differences from the reference image (Fig. 4.2a, top) can be seen in the lower part (Fig. 4.2b-e, bottom). To facilitate a comparison of the areas within the compartments, they were scaled up by a factor of 10. At this scale, it can be seen that the algorithm fails to reconstruct some of the small variations in signal intensity caused by the Gibbs ringing with an increasing noise level. For lower noise levels, the deviations from the reference image vary systematically over the compartments. Areas with more signal intensity reveal larger deviations. For higher noise levels, however, the differences are distributed randomly over the compartments.

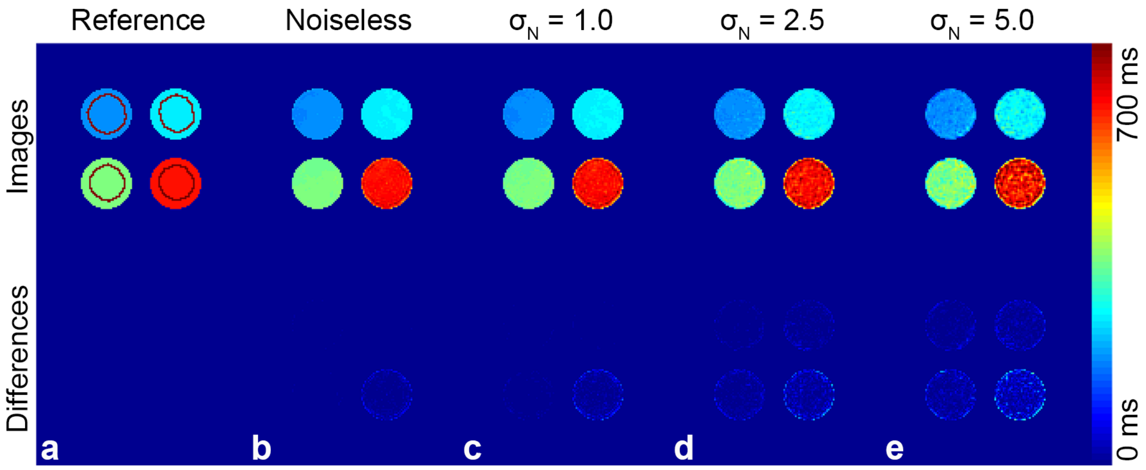

**Figure 4.3:** Numerical simulations. $T_1^*$ maps corresponding to the reconstructions depicted in Figure 4.2. The areas used for the RoI analysis are indicated in dark red. Modified Figure from [94].

Figure 4.3 depicts $T_1^*$ maps corresponding to the reconstructions of Figure 4.2 (top) and the differences between reference and reconstructed $T_1^*$ maps (bottom). For reasons of clarity, $T_1^*$ values outside of the compartments were masked. Figure 4.3a (top) shows the reference $T_1^*$ map with the areas used for the RoI analysis marked in dark red, Figure 4.3b-e (top) depicts MAP reconstructed $T_1^*$ maps obtained from single-preparation datasets with the indicated noise levels.

| Position | Top left<br>$\mu \pm \sigma$ (ms) | Top right<br>$\mu \pm \sigma$ (ms) | Bottom left<br>$\mu \pm \sigma$ (ms) | Bottom right<br>$\mu \pm \sigma$ (ms) |
|---|---|---|---|---|
| a) Reference | 180 | 250 | 340 | 600 |
| b) Noiseless | $178.6 \pm 2.9$ | $250.4 \pm 2.3$ | $341.8 \pm 4.0$ | $600.4 \pm 8.7$ |
| c) $\sigma_N = 1.0$ | $178.5 \pm 3.5$ | $250.8 \pm 3.0$ | $342.2 \pm 4.9$ | $601.7 \pm 13.1$ |
| d) $\sigma_N = 2.5$ | $180.5 \pm 5.7$ | $253.4 \pm 10.0$ | $344.1 \pm 11.2$ | $601.4 \pm 24.5$ |
| e) $\sigma_N = 5.0$ | $181.6 \pm 10.2$ | $255.5 \pm 16.9$ | $343.3 \pm 20.6$ | $603.4 \pm 45.3$ |

**Table 4.1:** Numerical simulations. Means ($\mu$) and standard deviations ($\sigma$) of $T_1^*$ obtained in the RoI analysis of the $T_1^*$ maps depicted in Figure 4.3. Table from [94].

The values obtained by the RoI analysis of the $T_1^*$ maps in Figure 4.3 are listed in Table 4.1. The noisier the initial dataset and the larger the $T_1^*$ value of the respective compartment, the wider the range of $T_1^*$ values obtained. Although the variations of the reconstructed $T_1^*$ values within the compartments are growing with an increasing noise level $\sigma_N$, their mean values are still in very good agreement with the reference values.

Figure 4.4 illustrates the temporal evolution of the consistent k-spaces $\widehat{K}_\xi(t)$ (obtained in step 4 of the reconstruction algorithm, top) and the corresponding image spaces $\widehat{M}_\xi(t)$

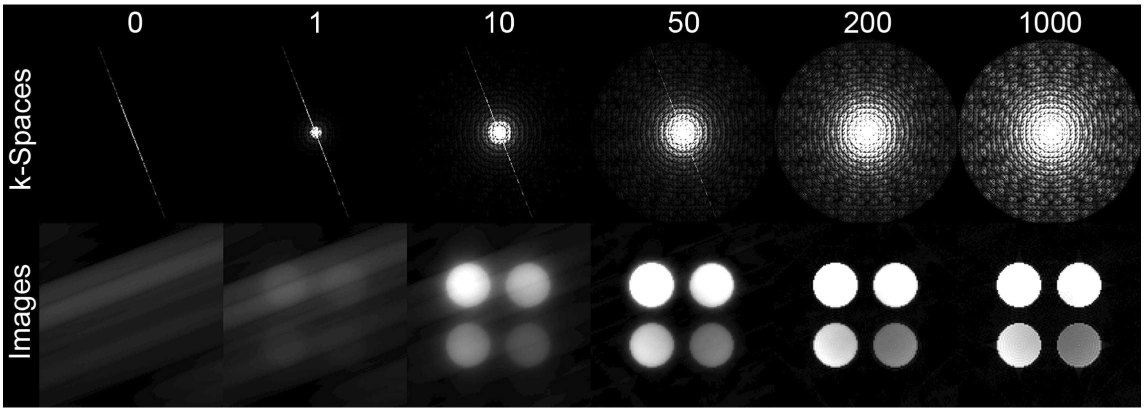

**Figure 4.4:** Numerical simulations. Temporal evolution of the consistent k-spaces and the corresponding image spaces for an exemplary time point $T_I = 38\,\mathrm{ms}$ after the indicated number of iterations performed. Modified Figure from [94].

(used in step 1 of the reconstruction algorithm, bottom) with the number of iterations performed. MAP reconstructions are shown corresponding to time point $T_S = 38\,\mathrm{ms}$ after the SR pulse for the iteration numbers indicated. The initial k-space only consists of one projection. An inverse Fourier transform yields the initial image space with only one dimension encoded. In the course of the reconstruction, this almost empty k-space is continuously filled with intensity. For the first iterations (iteration 1 to ~ 50), the k-space is still dominated by the initial projection. In the image domain, this is expressed by a superposition of the initial pseudo-two-dimensional image space and the slowly forming two-dimensional object. Once the central k-space is filled with enough intensity (~ iteration 50), the initial image space starts fading out. The corresponding k-space now contains enough information that it is no longer dominated by the signal of the acquired projection. With a growing number of iterations performed, the k-space is slowly filled from the central towards the outer regions, corresponding to an improvement of the image resolution. The edges of the compartments become more and more pronounced until eventually the whole circular k-space is filled with intensity and even the Gibbs ringing artifacts resulting from finite support in k-space become visible (~ iteration 1000). Changes between two consecutive iterations are now imperceptibly small.

### 4.4.2 Phantom Experiments

All reconstructions in this subsection were terminated after 1000 MAP iterations.

Figure 4.5 shows reconstructed images of the phantom measurements. Depicted is the Nyquist sampled reference (Fig. 4.5a) as well as the MAP reconstruction from a single-preparation dataset after 1000 iterations (Fig. 4.5b) for the saturation times $T_S$ indicated. A ten-fold difference image (Fig. 4.5c) is added to facilitate a comparison. $T_S = 140.3\,\mathrm{ms}$ (top row) is exemplary for the relaxation process, whereas at $T_S = 3459.7\,\mathrm{ms}$ (bottom

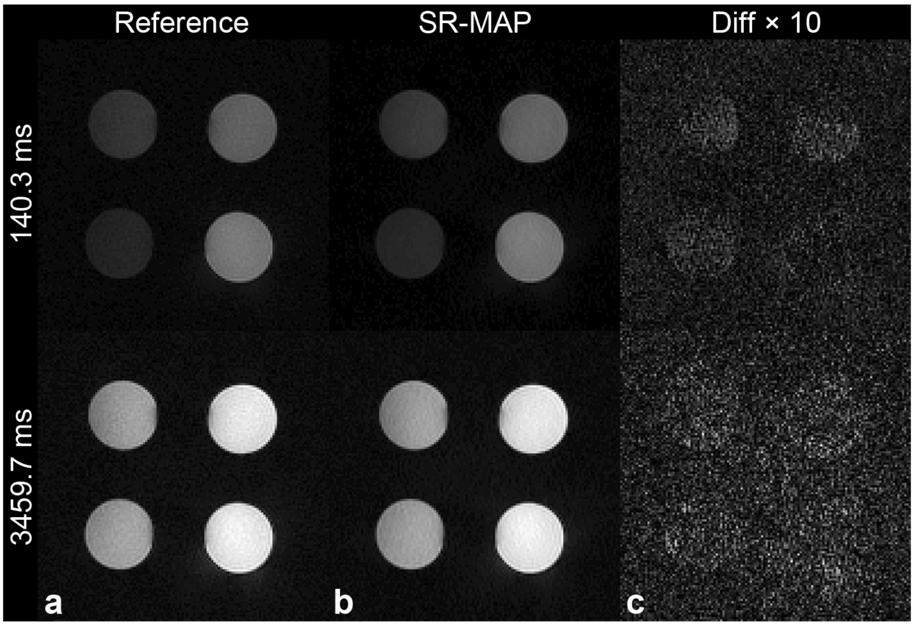

**Figure 4.5:** Phantom measurements. Reference and MAP reconstructed (1000 iterations) image spaces of the phantom measurements for the exemplary time points indicated on the left. Modified Figure from [94].

row), the magnetization has almost reached the steady-state magnetization $M_0^*$. The variations in both images are relatively small and no systematic errors occur.

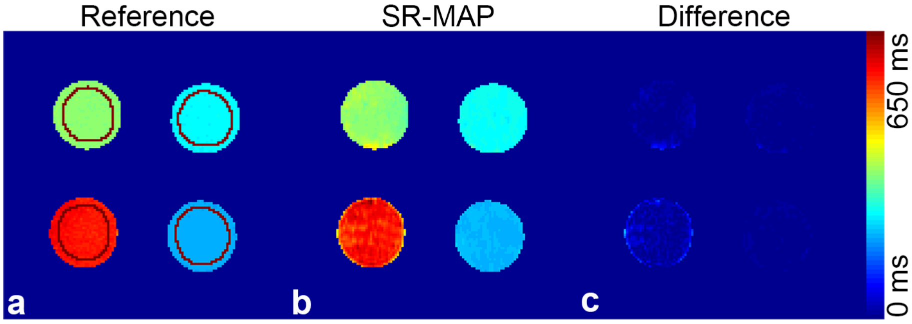

**Figure 4.6:** Phantom experiments. $T_1^*$ maps of the phantom measurements corresponding to the reconstructions of Figure 4.5. The areas used for the RoI analysis are indicated in dark red. Modified Figure from [94].

The corresponding $T_1^*$ maps are presented in Figure 4.6. The maps obtained from the reference dataset (Fig. 4.6a) and the MAP reconstructions (Fig. 4.6b) as well as their differences (Fig. 4.6c) are shown. Again, the areas used for the RoI analysis are indicated in dark red.

The results of the RoI analysis are listed in Table 4.2. The MAP reconstruction yields good estimates of the $T_1^*$ values. Although the standard deviation within the RoIs increases with the order of magnitude of $T_1^*$ ($\sim 3.4\,\%$ for the largest $T_1^*$ value) and a small

| Position | Bottom right<br>$\mu \pm \sigma$ (ms) | Top right<br>$\mu \pm \sigma$ (ms) | Top left<br>$\mu \pm \sigma$ (ms) | Bottom left<br>$\mu \pm \sigma$ (ms) |
|---|---|---|---|---|
| a) Reference | $185.7 \pm 1.5$ | $237.3 \pm 2.0$ | $329.1 \pm 3.6$ | $553.6 \pm 8.4$ |
| b) MAP | $192.0 \pm 2.7$ | $242.9 \pm 3.2$ | $330.0 \pm 9.2$ | $553.6 \pm 18.9$ |

**Table 4.2:** Phantom experiments. Means ($\mu$) and standard deviations ($\sigma$) of $T_1^*$ obtained in the RoI analysis of the $T_1^*$ maps depicted in Figure 4.6. Table from [94].

error in the mean $T_1^*$ value increasing towards smaller $T_1^*$ values (~ 3.4 % for the smallest $T_1^*$ value) can be observed, the means of reference and reconstruction still strongly agree, especially with regard to an acquisition time of only 3.6 s for the MAP acquisition compared to more than 2 h for the segmented reference scan.

### 4.4.3 In Vivo Measurements

Results of the in vivo measurements are depicted in Figures 4.7 and 4.8. The termination criterion was reached after 285 iterations.

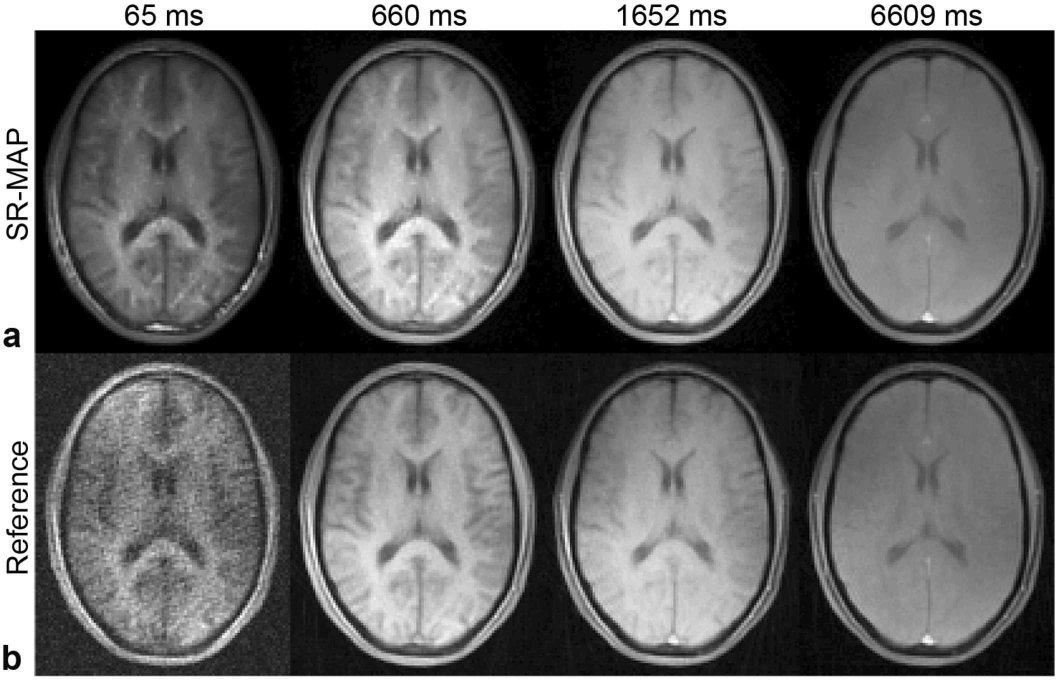

**Figure 4.7:** In vivo measurements. Exemplary MAP reconstructions (a) and the corresponding reference images (b) are shown for the contrasts indicated. Modified Figure from [94].

Representative MAP images (Fig. 4.7a) and the according reference images (Fig. 4.7b) are shown for different saturation times $T_S$. As the intensity in the images is increasing during the relaxation process, a separate normalization was performed for each $T_S$. Although the reference image is strongly affected by noise, both reconstructions show the same contrast behavior for all $T_S$.

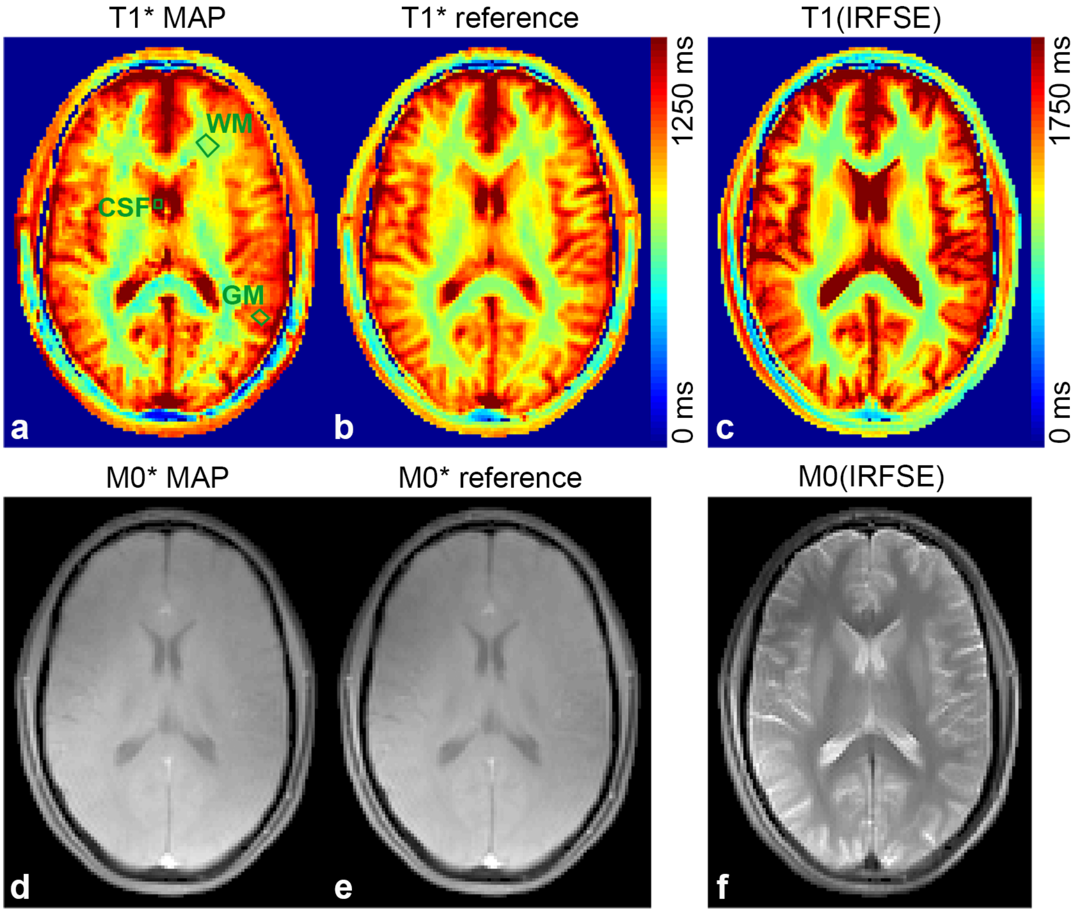

**Figure 4.8:** In vivo measurements. Depicted are $M_0^*$ and masked $T_1^*$ maps for the MAP reconstructions (a,d) and the reference data (b,e) as well as the standard $M_0$ (f) and masked $T_1$ maps (c) obtained by the IRFSE measurement. Modified Figure from [94].

Figure 4.8 depicts $M_0^*$ and masked $T_1^*$ maps for the MAP reconstructions (Fig. 4.8a,d) and the reference (Fig. 4.8b,e) as well as $T_1$ and $M_0$ obtained from the IRFSE measurement (Fig. 4.8c,f). While both $M_0^*$ maps as well as both $T_1^*$ maps are visually comparable, they show clear differences from the $T_1$ as well as the $M_0$ map, respectively. In particular, $T_1^*$ of both reconstructions is smaller than $T_1$.

The results of the associated RoI analysis (marked green in Fig. 4.8a) are listed in Table 4.3. While they indicate a very good agreement between the MAP reconstructed and the reference $T_1^*$ map in WM (deviation: 1.3 %), GM (deviation: 2.4 %) and CSF (deviation: 4.0 %), the clear difference to the $T_1$ values obtained in the IRFSE measurement, which was earlier observed in Figure 4.8, is confirmed.

| Position | WM<br>$\mu \pm \sigma$ (ms) | GM<br>$\mu \pm \sigma$ (ms) | CSF<br>$\mu \pm \sigma$ (ms) |
|---|---|---|---|
| a) $T_1^*$ Reference | $676 \pm 32$ | $928 \pm 39$ | $1655 \pm 102$ |
| b) $T_1^*$ MAP | $668 \pm 26$ | $900 \pm 37$ | $1588 \pm 28$ |
| c) $T_1$ IRFSE | $866 \pm 20$ | $1386 \pm 30$ | $4383 \pm 310$ |

**Table 4.3:** In vivo measurements. Means ($\mu$) and standard deviations ($\sigma$) of $T_1^*$ (IR-LL FLASH) and $T_1$ (IRFSE) obtained in the RoI analysis of the $T_1^*$ and $T_1$ maps depicted in Figure 4.8. Table from [94].

## 4.5 Discussion

The capability of the MAP algorithm to reconstruct images of various contrasts from a radial single-preparation dataset acquired after SR magnetization preparation was demonstrated in this chapter. As the difference between model and consistent images almost completely disappears after a certain number of iterations, every resulting image is carrying the contrast of the projection acquired at the respective saturation time $T_S$. Although an entire SR-LL FLASH dataset is used for the reconstruction, a consistency condition with a temporal resolution equal to the repetition time $T_R$ is applied to minimize the temporal footprint of the consistent images. An accurate determination of the resulting effective longitudinal relaxation parameter $T_1^*$ was shown in numerical simulations as well as in phantom and in vivo experiments. Although a determination of the native $T_1$ relaxation parameter would require knowledge about $B_1$ and therefore flip angle variations across the FoV (section 2.6) as well as further corrections concerning magnetization transfer and imperfect slice profiles [27], SR-MAP can be used to obtain quantitative information about a relaxation process from only one single-preparation measurement. The consistency of the MAP reconstructions with the acquired data signifies a major upgrade of the commonly used KWIC techniques [85] that use temporal averaging.

### 4.5.1 Radial Versus Other Trajectories

To describe the relaxation process in a single pixel of the image space, three pieces of information, namely magnetization, spin-lattice relaxation time, and a complex phase have to be known. In principle, this information can be obtained with any trajectory such as the interleaved Cartesian trajectories used in [25, 90]. Although in these publications, high acceleration factors were achieved by retrospective undersampling, it was still necessary to use segmented measurements. To enable the usage of single-preparation datasets, a radial sampling scheme was used in our approach. The advantage of the radial sampling pattern is the extensive coverage of the low spatial frequencies containing most of the image contrast, leading to a fast convergence of the algorithm. In addition, undersampling artifacts of radial trajectories are incoherent and have no preferential direction, improving the quality of the reconstructed images. Spiral trajectories offer another very promising way of k-space sampling as they not only cover the low frequencies but also feature a much better coverage of the higher frequencies compared to radial sampling.

### 4.5.2 The MAP Algorithm under Presence of Motion

All the data required for a MAP reconstruction can be acquired in one single-preparation measurement. This time efficient acquisition scheme leads to a lower sensitivity to motion artifacts compared to the more time-consuming segmented measurements. Even in case of motion occurring within the relatively short time span of a single-preparation acquisition, radial sampling schemes are often favored over their Cartesian counterpart due to their robustness in the presence of object motion [85]. Nevertheless, the technique would have to be adapted for anatomies such as the heart where cardiac or respiratory motion is to be expected.

### 4.5.3 Higher Intensity towards Outer Regions of the Field of View

In the numerical simulations, variations between reference and MAP reconstructions increase towards the outer regions of the FoV. This originates from the sensitivity profiles used in our numerical phantom. As these simulated coils were placed at the edges of the FoV, the corresponding sensitivity profiles lead to high signal intensities in these regions. Therefore, the Gibbs ringing is relatively large at the outer compartment edges. As the noise level reaches the order of magnitude of these truncation artifacts, they get lost in the noise and variations are evenly distributed over the entire compartments. In this case, the algorithm seems to suppress Gibbs ringing.

### 4.5.4 Dependence of the Accuracy of the $\mathbf{T_1}^*$ Estimates on the Temporal Coverage

Numerical simulations and phantom experiments both indicate that the exponential slope as well as the saturation value in every pixel has to be temporally covered by the dataset to quantify the relaxation parameter $T_1^*$ with sufficient accuracy. The larger the $T_1^*$, the longer the relaxation process will last, leading to ambiguous saturation values $M_0^*$ in case of an insufficient temporal coverage of the relaxation process. Depending on the desired accuracy of the reconstructed $T_1^*$ maps, the temporal coverage of the single-preparation measurement can be adapted with respect to the largest relaxation parameters expected. For experiments where only a limited temporal coverage is possible, e.g. due to motion of the measured object, the signal relaxation can be described by various large $T_1^*$ values in the same range, leading to a growing error in the determination of $T_1^*$. As relaxation curves more and more resemble other curves of similar $T_1^*$ values for large $T_1^*$, the algorithm will nevertheless deliver well resolved images consistent to the measured dataset.

In the numerical simulations, indications of this behavior can be seen for $T_1^* = 600\,\mathrm{ms}$, where the saturation value of $M_0^*$ is not sufficiently covered. For high noise levels, the standard deviation of the fitted relaxation parameter $T_1^*$ increases dramatically, whereas the image quality is not considerably impaired.

### 4.5.5 Convergence Behavior of the Algorithm

Every pixel of the k-space contains information about the relaxation process only for some time points $T_S$. Analogously, this leads to mentionable signal intensity only for several time points $T_S$ in every pixel of the corresponding image spaces. If a pixel is covered frequently enough by the k-space trajectory, the numerical two-parameter fit leads to the formation of a low-intensity version of the actual image. This results from only some pixels carrying the correct intensity while the other low-intensity pixels lead to an underestimation of the fitted parameters. The consistency step 4 can be seen as a superposition of the initial pseudo-two-dimensional image space and this low-intensity image of the measured object. As the energy in this low-intensity image is growing with every iteration, its proportion in the superimposed consistent image is growing as well until at some point, the intensity proportions in the superposition become equal or, in other words, the algorithm converges.

To improve the convergence behavior of MAP, the "nearly empty" k-spaces that are used to initialize the algorithm can be "filled" using a linear interpolation as described in section 3.3 or other temporal averaging methods. This way, less iterations might be necessary to fill the energy of the k-spaces and reach the termination criterion.

### 4.5.6 In Vivo Measurements

The reconstructions of the in vivo measurements demonstrate the functionality of the algorithm for clinical imaging. The deviations between the reference and the MAP reconstructed $T_1^*$ values obtained in the RoI analysis are as low as 1.3 % in WM, 2.4 % in GM, and 4.0 % in CSF. These differences are very small especially with respect to the acquisition times of ~ 24 min for the reference compared to 6.6 s for the single-preparation dataset. Inaccuracies of the MAP reconstructed maps can be caused by imperfect SR pulses leading to a residual magnetization $M_0 \neq 0$. In these areas, the signal cannot be perfectly described by the two-parameter model function Eq. 2.10, causing deviations in the fitted parameters. To compensate for that, the two-parameter model could be supplemented by an initial magnetization similar to Eq. 2.8. Alternatively, the type and order of pulses used for the saturation could be further optimized as proposed in [50].

The fact that the in vivo reconstruction - other than both phantom studies - reaches the termination criterion lies in the more complex nature of the object to be reconstructed. While the assumption of only one longitudinal relaxation parameter per voxel holds very well for the phantom, an anatomical voxel inside the human brain consists of various tissue types and can only be described by the mono-exponential model up to a certain point. At this point, the algorithm is terminated as no further improvement or even deterioration can be expected.

The values of the relaxation parameter $T_1$ obtained in the IRFSE measurement are in good agreement with the literature values published by Wansapura et al. [106] (WM: 832 ms, GM: 1331 ms). According to Eq. 2.7, the effective relaxation parameter $T_1^*$ is generally smaller than $T_1$ due to the continuous excitation. This prediction coincides with the in vivo results, where the effective values $T_1^*$ are systematically lower than the true relaxation times $T_1$. They are, however, in the same ratio with respect to Eq. 2.7.

### 4.5.7 Iterative Algorithm Versus Numerical Optimization

One iteration of the algorithm lasted around 70 s for a dataset with 512 time steps $T_S$ for a $256 \times 256$ image matrix. This time is proportional to the number of elements of the image matrix. Compared to numerical optimization procedures, the iterative method takes quite a long time to converge. In principle, such numerical optimization procedures could likewise be applied to perform MAP reconstructions, their convergence behavior is, however, depending on regularizing parameters. The lack of a generally accepted method for objectively choosing these parameters depending on the problem to be solved leads to problems of the transferability of these methods. The proposed method does without any explicit regularization parameters, making it transferable and independent of the particular problem. The fairly simple and straight-forward implementation of the algorithm used in this chapter (and therefore also in [94]) was used as a proof of principle of the idea. There is a variety of possibilities to speed up the algorithm such as parallelizing the implementation of the algorithm or using images with more intensity as initial image spaces for a faster convergence.

### 4.5.8 Numerical Fit Versus Dictionary-based Approach

In [25], Doneva et al. incorporate the signal model in the reconstruction using a collection (dictionary) of discrete-time signal prototypes (atoms). In case of a dictionary with infinitely many atoms, the signal can be represented by one single atom which is equivalent to a numerical fit of a model function to the signal. In our case of SR magnetization preparation, the signal can be modeled by only two parameters. Thus, a fast numerical fitting algorithm is easy to implement and provides equivalent results without the need of choosing the appropriate dictionary size and the number of atoms used for signal approximation. For more complex relaxation models such as the three-parameter model used to describe IR-LL FLASH sequences (section 2.5) or a multi-exponential model which might be used to describe voxels containing multiple different tissue types, a numerical fit would take considerably longer to converge and the dictionary-based approach might be the better choice.

### 4.5.9 Limits of the Mono-exponential Signal Model

Another issue that has to be addressed is the assumption of a mono-exponential relaxation in every voxel. This leads to a high sensitivity for artifacts in image regions or voxels not complying with this model such as voxels containing multiple tissues of different relaxation parameters. Gibbs ringing originating in regions of high intensity might also influence surrounding voxels by superimposing their exponential decay, leading to a multi-exponential behavior not described by the model. These problems could be overcome by extending the algorithm using a multi-exponential model, with the disadvantage of an even greater requirement in reconstruction time and computational power.

# 5 MAP with Inversion Recovery Magnetization Preparation

## 5.1 Introduction

The initial implementation of MAP which was described in the previous chapter combines the benefit of a simple two-parameter model with the speed-efficient saturation preparation, rendering relaxation breaks between subsequent preparations unnecessary. However, the relaxation process contains no information about the equilibrium magnetization $M_0$ (compare Eq. 2.10) and a direct calculation of $T_1$ using Eq. 2.9 becomes impossible. Moreover, variations of the flip angle $\alpha$ within the excited slice impede the use of Eq. 2.5 for calculating $T_1$.

In this chapter, the MAP algorithm is modified to directly enable $T_1$ mapping. By replacing the SR magnetization preparation with an inversion recovery preparation scheme, additional information about the relaxation process - namely the equilibrium magnetization $M_0$ - becomes available. Although this slightly complicates the fitting procedure, the true $T_1$ can now be obtained without knowledge of the actual flip angle $\alpha$. To additionally sensitize the fitted model to the influence of multi-exponential relaxation in voxels containing multiple different tissue types, a dictionary-based approach as described in section 3.4 is applied instead of the previously used mono-exponential least-squares fit to enforce the model to the acquired data. The technique will be called **I**nversion **R**ecovery **MAP** (IR-MAP) in the following.

Some of the content of this chapter has been submitted for publication in *PLOS ONE* [96]. Reused images are marked in the image caption.

## 5.2 Implementation of IR-MAP

In this implementation of MAP, a radial dataset obtained in a single IR-LL FLASH acquisition (see section 2.5) is used as input for the reconstruction. Therefore, the magnetization after the IR pulse can be modeled by Eq. 2.8.

To improve the convergence behavior of the algorithm, the "nearly empty" k-spaces obtained by gridding the single projections into separate k-spaces were "filled" by a linear interpolation of all acquired k-space points through time as described in 3.3. These improved k-spaces were used for initialization of the algorithm.

As in the previous chapter, any changes from the reconstruction scheme described in section 3.2 will be pointed out in the following. Again, the pixel index $x$ will be omitted for reasons of clarity.

1. As before, the current consistent model k-spaces $\widehat{K}_\xi$ of all individual coils were Fourier transformed to obtain consistent model images $\widehat{M}_\xi$.

2. Before the pixel-wise fit, the signals received in the different coils $\xi$ were combined using a SoS as described in section 2.11. As a negative signal intensity is to be expected directly after the inversion, the sign of the relaxation curve was respected by taking the real part of the complex-valued magnetization after a rotation to the real axis (2.23 with $I \to \widehat{M}$):

   $$\widehat{M}_{\mathrm{Real},\xi}(t) = \mathrm{Real}\left\{\widehat{M}_\xi(t) \cdot \exp(-i\varphi_\xi)\right\} . \tag{5.1}$$

   A phase map $\varphi_\xi(x)$ was determined before the application of the algorithm from a Nyquist sampled image reconstructed from the projections acquired after the zero-crossing of the magnetization. Using this "signed" magnetization, the sign-dependent SoS was calculated using Eq. 2.24 with $I \to \widehat{M}$:

   $$\widehat{M}_{\mathrm{combined}}(t) = \mathrm{sign}\left(\theta(t)\right) \cdot \sqrt{|\theta(t)|} ,$$

   where

   $$\theta(t) = \sum_\xi \left[\mathrm{sign}\left(\widehat{M}_{\mathrm{Real},\xi}(t)\right) \cdot \left|\widehat{M}_{\mathrm{Real},\xi}(t)\right|^2\right] . \tag{5.2}$$

   Next, a dictionary-fit was used to obtain a combined model $M_{\mathrm{combined}}(t) = \mathbf{D}\gamma_s$ of all coils (see section 2.10).

3. Before the backward transform, the model images $M_{\mathrm{combined}}(t)$ had to be re-separated into one model image $M_\xi(t)$ for each coil. Again, a complex single-coil relaxation process is modeled by multiplying the coil-combined model $M_{\mathrm{combined}}(t)$ with a complex coil sensitivity factor $c_\xi$, leading to the following model (Eq. 2.19 with $\mathbf{x} \to M$):

   $$M_\xi(t) = c_\xi \cdot M_{\mathrm{combined}}(t) = c_\xi \cdot \mathbf{D}\gamma_s . \tag{5.3}$$

   As $\mathbf{D}\gamma_s$ can be assumed to be coil-independent, the real and imaginary parts of the product $c_\xi$ in each coil were determined separately by using a least-squares approach on Eq. 5.3. The resulting single-coil model images $M_\xi(t)$ were Fourier transformed to obtain single-coil model k-spaces $K_\xi(t)$.

4. As before, the data consistency was ensured by substituting the measured data for the model data separately for all acquired projections and all coils and by additionally zeroing the resulting consistent model k-spaces $\widehat{K}_\xi(t)$ at all pixels where no information was acquired for all $T_S$.

The dictionary used for all reconstructions performed in this chapter consisted of 1665 mono-exponential relaxation curves calculated using Eq. 2.8 for different parameter combinations of $T_1$ (185 values between 10 ms and 5000 ms) and $\alpha \in \{1°, 2°, \ldots, 9°\}$. In the fitting step 2 of the algorithm, an orthogonal matching pursuit algorithm [78] was used in conjunction with this dictionary to find a linear combination of 3 relaxation curves best describing the relaxation behavior in each voxel of the consistent model images $\widehat{M}(t)$. After termination of the algorithm, a pixel-wise mono-exponential fit of Eq. 2.8 was applied to the final consistent model images to obtain $T_1^*$, $M_0^*$ and $M_0$. Finally, one single $T_1$ value was calculated for every pixel using Eq. 2.9.

## 5.3 Methods

All imaging experiments were carried out on a 3 T whole-body scanner (MAGNETOM Trio, Siemens AG Healthcare Sector, Erlangen, Germany) employing a 12 channel phased-array head coil for signal reception.

All post-processing was performed on a standard desktop PC equipped with an Intel Core i7-2600 CPU (3.4 GHz) using MATLAB (The MathWorks, Natick, MA).

For comparability of the reconstructions, the number of iterations was set to a fixed number of 50 for all IR-MAP reconstructions performed in this section.

### 5.3.1 Phantom Experiments

To validate the functionality of the proposed reconstruction algorithm and the accuracy of the resulting $T_1$ values, a phantom study was performed on a phantom consisting of 7 vials with different concentrations of CA (Resovist®, Bayer Schering Pharma, Berlin, Germany) and copper sulfate ($CuSO_4$). $T_1$ measurements were performed with a globally prepared IR-LL FLASH sequence (FoV: $200 \times 200 \times 4\,\text{mm}^3$, $T_R$: 6 ms, $T_E$: 2.5 ms, $\alpha$: 7°, total acquisition time: 6s) with a Golden Ratio [108] radial k-space trajectory (projections: 1000, readouts points: 128). After a single-prepared acquisition, the IR-MAP algorithm was used for $T_1$ mapping. This is schematically depicted in Figure 5.1 (green).

To assess the accuracy of these relaxation times, a fully sampled IR-LL FLASH reference was acquired in a segmented fashion which is illustrated in Figure 5.1 (orange). The acquisition consisted of 200 consecutive IR-LL FLASH measurements - the Nyquist limit for a radial measurement with 128 readout points per projection. While the same IR-LL FLASH sequence as before was used, the order of the 1000 projections was varied after each inversion pulse. By retrospectively reordering these projections, a set of 1000 k-spaces was generated, each carrying the contrast of one of the 1000 inversion times $T_I$ used in the acquisition and each fully sampled with 200 projections. Each of these IR-LL FLASH segments was followed by a delay of 15 s, allowing for a complete relaxation before the acquisition of the subsequent IR-LL FLASH segment. This led to a total scan time of ~ 1 h compared to 6 s for the single-inversion measurement. After

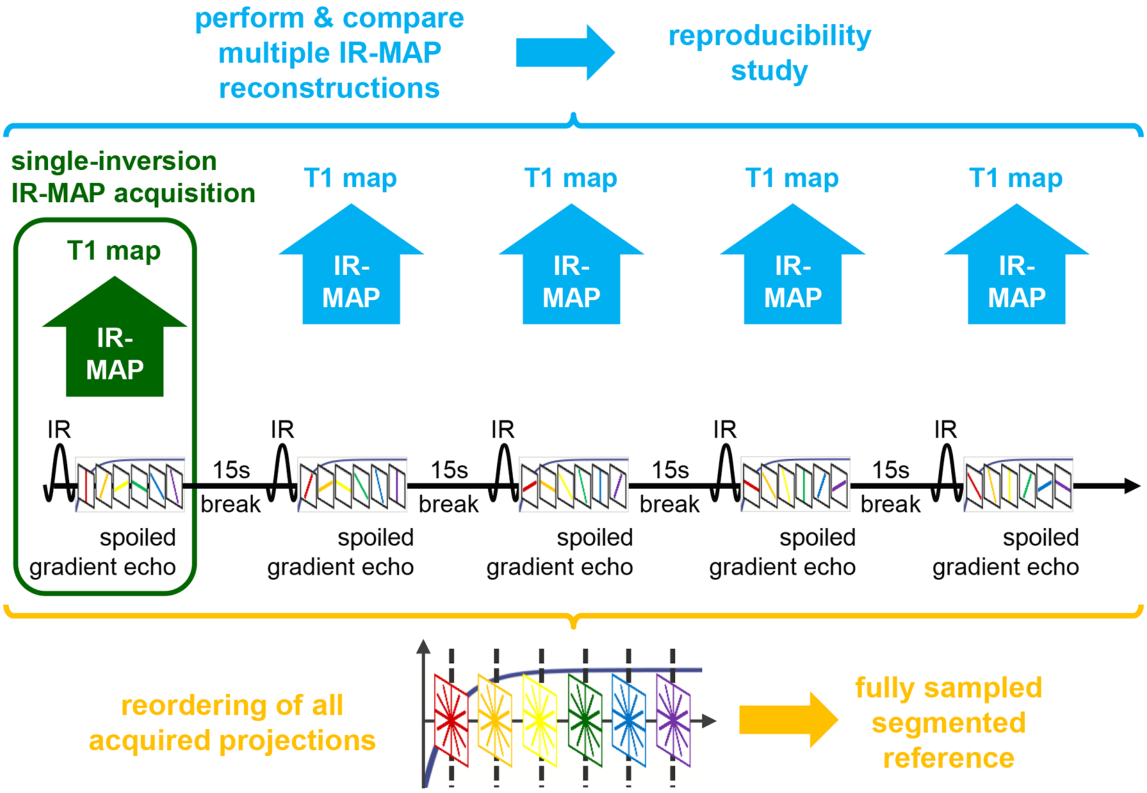

**Figure 5.1:** Acquisition scheme of all acquisitions performed in this work. The regular IR-MAP acquisition consists of one inversion followed by a spoiled gradient-echo data collection (green). The segmented reference is acquired by performing multiple IR-LL FLASH acquisitions, each of which is followed by a 15 s break for relaxation before the next inversion (orange). Using IR-MAP reconstructions for multiple of the acquired IR-LL FLASH datasets, a reproducibility study was carried out (blue). Figure from [96].

gridding, a pixel-wise three-parameter fit of Eq. 2.8 to the SoS of all coils was used to obtain reference $T_1^*$, $M_0^*$, $M_0$ maps. Again, Eq. 2.9 was used to obtain $T_1$.

Using the data of the segmented reference acquisition, a reproducibility study was performed by separately applying IR-MAP reconstructions to the first 10 IR-LL segments. This is illustrated in Figure 5.1 (blue). The resulting set of $T_1$ maps was used to test the reproducibility of the $T_1$ values obtained from the IR-MAP reconstruction in repeated acquisitions.

Additionally, a segmented inversion recovery $T_1$ mapping experiment as described in 2.4 with only one RF excitation and gradient-echo readout per inversion was performed (FoV: $200 \times 200 \times 4\,\mathrm{mm}^3$, $T_R$: 6 ms, $T_E$: 2.5 ms, $\alpha$: 7°, matrix size: $128 \times 128$, total acquisition time: $\sim 10$ h). In a segmented fashion, fully sampled images were acquired for 10 inversion times (13 ms, 50 ms, 100 ms, 250 ms, 500 ms, 1000 ms, 1600 ms, 2500 ms, 5000 ms, 8000 ms). As in the segmented IR-LL FLASH measurement, a relaxation break of 15 s was kept between successive segments. After the acquisition, a fit of Eq. 2.2 resulted in a $T_1$ map that was used for validating the general accuracy of the IR-MAP technique.

A RoI analysis was used to obtain mean values $\mu_{\text{vial}}$ and standard deviations $\sigma_{\text{vial}}$ of $T_1$ in every compartment of both the reference and the IR-MAP reconstructed $T_1$ maps. Additionally, the SNR in each of the vials was calculated for all three reconstruction techniques [24]:

$$\text{SNR}_{\text{vial}} = \frac{\mu_{\text{vial}}}{\sigma_{\text{vial}}} \tag{5.4}$$

### 5.3.2 In Vivo Measurements

All human in vivo studies were approved by our local ethics committee. They were performed on healthy volunteers, and written informed consents were obtained from the subjects prior to scanning.

$T_1$ measurements of the brains of 7 healthy volunteers aged between 23 and 30 years were carried out with the same sequence as in the phantom experiments (slice thickness: 4 mm, $T_R$: 6 ms, $T_E$: 2.5 ms, $\alpha$: 7°, projections: 1000, readout points: 128 , total acquisition time: 6 s), with a FoV ranging between $200 \times 200\,\text{mm}^2$ and $220 \times 220\,\text{mm}^2$. After the acquisition, $T_1$ maps were obtained using IR-MAP as described in the phantom experiments.

Additionally, a fully sampled IR-LL FLASH reference dataset was obtained using the same segmented acquisition as in the phantom experiments. To shorten the scan time, the number of segments was reduced from 200 to 100, leading to each of the 1000 contrast images consisting of only 100 projections, the equivalent of a two-fold Nyquist undersampling. Maintaining a relaxation delay of 15 s between successive inversions, the total scan time was reduced to ~ 30 min. Using this acquisition, a reference $T_1$ map was obtained as described in the phantom experiments.

A RoI analysis was used to obtain mean values of $T_1$ in WM, GM and CSF for the reference as well as the IR-MAP reconstructed $T_1$ maps of each volunteer. For comparison of both reconstruction methods, a mean SNR over all volunteers was obtained according to Eq. 5.4.

## 5.4 Results

### 5.4.1 Phantom Experiments

Figures 5.2, 5.3 and 5.4a show results of the phantom measurement. The upper part of Figure 5.2 depicts the masked $T_1$ maps obtained from the segmented IR reference (left), the IR-MAP reconstruction of a single-inversion IR-LL FLASH measurement (center) as well as the segmented IR-LL FLASH reference (right). The lower part shows differences of both LL-based reconstructions from the segmented IR reference. A comparison of the two reference measurements shows a small deviation between the segmented **I**nversion **R**ecovery **L**ook-**L**ocker acquisition (IR-LL) and the segmented IR method increasing with $T_1$. Despite a noisier appearance, the same deviation is visible for the IR-MAP reconstructed $T_1$ map.

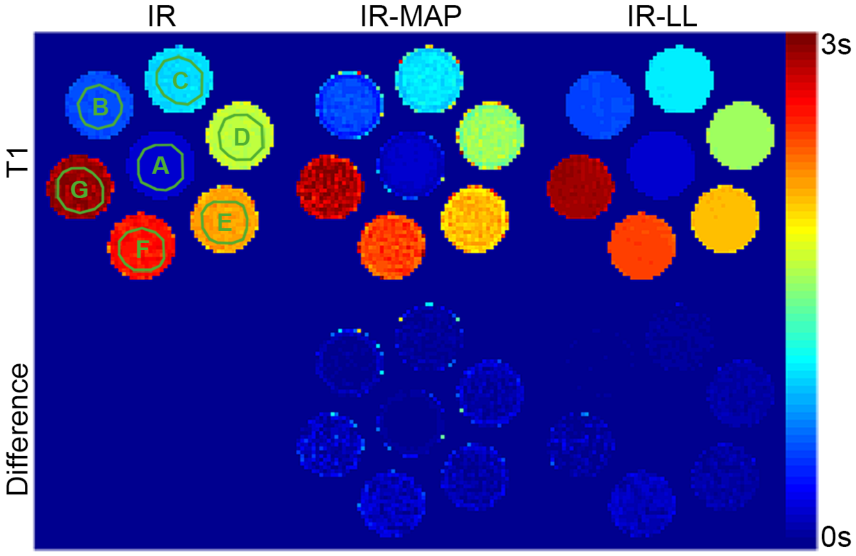

**Figure 5.2:** Phantom measurement. $T_1$ maps of the segmented IR reconstruction (left, top), the IR-MAP reconstruction of the single-inversion IR-LL FLASH acquisition (center, top) and the segmented IR-LL FLASH reference (right, top) as well as the differences (bottom). Figure from [96].

The visual observations are confirmed by the associated RoI analysis depicted in Table 5.1. The noisier appearance of the IR-MAP reconstruction is confirmed by a lower SNR (ranging between 14 and 35) especially in comparison to the segmented IR-LL acquisition (ranging between 80 and 220), but also to the segmented IR acquisition (ranging between 31 and 72). However, despite the larger standard deviations of the IR-MAP reconstruction, the values of both LL-based methods are in good agreement with a difference smaller than 2.3 % for all RoIs. Although there is a larger deviation between both of these methods and the segmented IR measurement, the differences, which are additionally listed in Table 5.1, also stay below 5.8 % for all RoIs. Overall, the IR-MAP results are in very good agreement with both references.

Figure 5.3 shows images of the IR-MAP reconstruction (top) and the reference (bottom) for exemplary inversion times. Again, although the visual appearance of the IR-MAP reconstructions is noisier, the contrasts of the both reconstructions are in good agreement.

The reproducibility study, which is depicted in Figure 5.4a, shows no systematic deviations in means and standard deviations of $T_1$ in repeated IR-MAP reconstructions of the

| Vial | IR | | IR-MAP | | | IR-LL | | |
|---|---|---|---|---|---|---|---|---|
| | $\mu \pm \sigma$ (ms) | SNR | $\mu \pm \sigma$ (ms) | SNR | diff (%) | $\mu \pm \sigma$ (ms) | SNR | diff (%) |
| A | $208 \pm 4$ | 50 | $201 \pm 14$ | 14 | 3.3 | $197 \pm 2$ | 80 | 5.1 |
| B | $573 \pm 15$ | 38 | $572 \pm 37$ | 16 | 0.1 | $560 \pm 6$ | 101 | 2.3 |
| C | $998 \pm 20$ | 49 | $1043 \pm 38$ | 27 | 4.5 | $1046 \pm 6$ | 171 | 4.8 |
| D | $1659 \pm 23$ | 72 | $1574 \pm 56$ | 28 | 5.1 | $1574 \pm 8$ | 188 | 5.1 |
| E | $2123 \pm 38$ | 55 | $2056 \pm 59$ | 35 | 3.2 | $2042 \pm 9$ | 220 | 3.8 |
| F | $2560 \pm 49$ | 52 | $2411 \pm 70$ | 34 | 5.8 | $2418 \pm 13$ | 191 | 5.5 |
| G | $2929 \pm 94$ | 31 | $2854 \pm 138$ | 21 | 2.6 | $2885 \pm 22$ | 130 | 1.5 |

**Table 5.1:** Phantom experiments. Listed are means ($\mu$) and standard deviations ($\sigma$) of $T_1$ within the RoIs A-G of the phantom experiment as well as the corresponding SNR. For the two LL-based acquisitions, the percentage difference to the IR values is additionally listed. Table from [96].

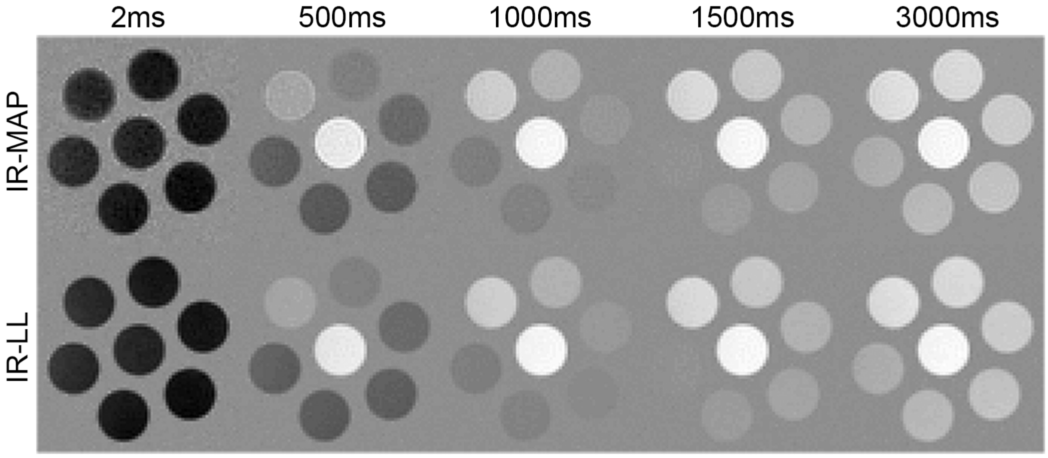

**Figure 5.3:** Phantom measurement. IR-MAP reconstructions (top) and reference IR-LL FLASH images (bottom) for exemplary inversion times. Figure from [96].

same FoV.

### 5.4.2 In Vivo Measurements

The results of the in vivo measurements are depicted in Figures 5.4b, 5.5 and 5.6. Figure 5.5 shows $T_1$ maps from IR-MAP reconstructions (left) and the IR-LL reference (center) as well as a difference for volunteers V3 and V7. Despite a general accordance between both $T_1$ maps, the IR-MAP reconstructions have the same noisier overall appearance that was already observed in the phantom measurements. In contrast to the phantom study, blurring can be observed in the in vivo reference. The largest differences occur in small areas of large $T_1$ values such as the CSF in the ventricles.

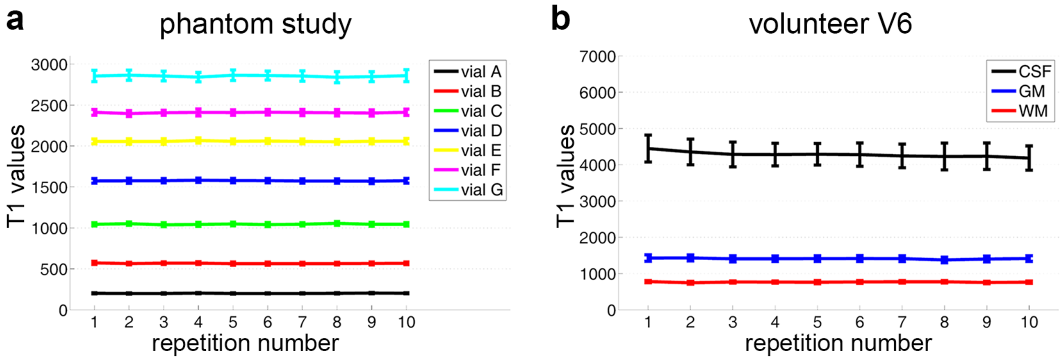

**Figure 5.4:** Reproducibility study. Shown are the mean $T_1$ values obtained from IR-MAP reconstructions of 10 consecutive IR-LL FLASH acquisitions, each of which was followed by a 15 s break for relaxation. While (a) shows the results in the 7 RoIs of the phantom (A-G), (b) depicts the RoIs used for evaluation of $T_1$ in WM, GM and CSF of volunteer V7. Figure from [96].

Figure 5.6 shows the corresponding images of the IR-MAP reconstruction (top) and the reference (bottom) for the same exemplary inversion times as in the phantom experiments. Despite the blurry nature of the reference images that was already observed in the $T_1$ maps, both reconstructions reveal the same contrast variations. The visual impression is confirmed by the results of the RoI analysis in Table 5.2. The noisier appearance of the IR-MAP reconstruction manifests in a larger standard deviation within the RoIs as well as a smaller mean SNR. This difference decreases with the value of $T_1$ ($\mathrm{SNR_{CSF}} < \mathrm{SNR_{GM}} < \mathrm{SNR_{WM}}$). However, differences of the means in WM and GM stay below 5.1 % in all volunteers, underlining the good agreement between the two reconstructions. In contrast, the means in the CSF regions deviate by up to 27.6 % in V6.

The in vivo reproducibility study, which is depicted in Figure 5.4b, shows no systematic deviations in means and standard deviations of $T_1$ in WM and GM. However, $T_1$ in the CSF is decreasing with each of the repeated IR-MAP acquisitions.

## 5.5 Discussion

### 5.5.1 Phantom Experiments

The $T_1$ maps of the phantom experiments clearly prove the functionality of IR-MAP for parameter mapping. The lower SNR of the IR-MAP reconstructions can be explained by the fact that only a small fraction of the data volume which was used for the reconstruction of both reference $T_1$ maps was used in the model-based IR-MAP reconstruction (0.5 % for the IR-LL reference and 10 % for the IR reference). This SNR reduction also causes the higher standard deviations within the RoIs of the IR-MAP reconstructed $T_1$

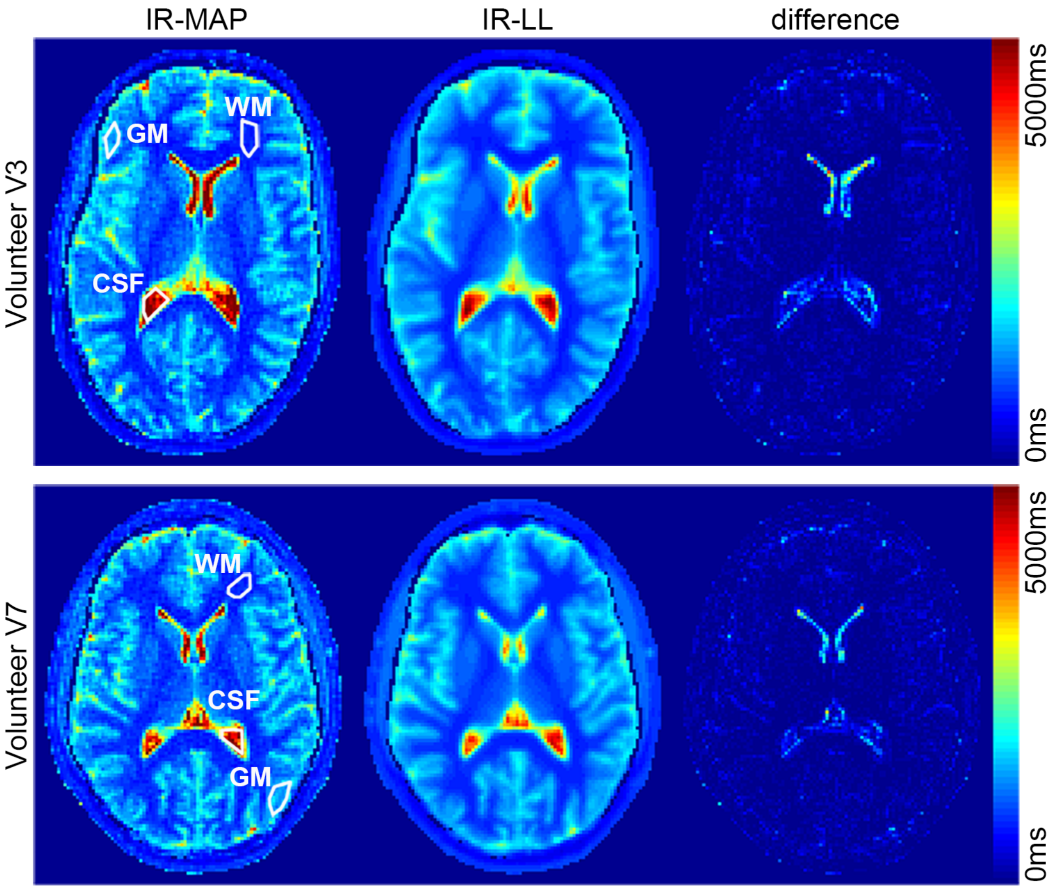

**Figure 5.5:** $T_1$ maps of the IR-MAP reconstruction (left) and the segmented IR-LL FLASH reference (center) as well as a difference (right) for volunteers V3 and V7. Figure from [96].

maps. With a difference of less than 2.3 % to the IR-LL reference and 5.8 % to the IR reference, IR-MAP still provides a very good accuracy of the reconstructed $T_1$ values. The images obtained by the IR-MAP reconstruction reveal the same noise enhancement as the $T_1$ maps. Apart from that, the images feature the same spatial and temporal resolution as well as the same contrast as the reference. Altogether, the very small degradation in image quality and the slightly larger standard deviation of the determined $T_1$ values is acceptable considering the acquisition time of 6 s for the IR-MAP reconstruction compared to ~ 1 h for the IR-LL reference and ~ 10 h for the IR reference.

Additionally, the reproducibility study demonstrates the functionality of the IR-MAP method in repeated measurements.

| | WM | | GM | | CSF | |
|---|---|---|---|---|---|---|
| | IR-MAP | REF | IR-MAP | REF | IR-MAP | REF |
| | $\mu \pm \sigma$ (ms) | $\mu \pm \sigma$ (ms) | $\mu \pm \sigma$ (ms) | $\mu \pm \sigma$ (ms) | $\mu \pm \sigma$ (ms) | $\mu \pm \sigma$ (ms) |
| V1 | 736 ± 82 | 734 ± 16 | 1447 ± 130 | 1436 ± 94 | 4694 ± 657 | 4296 ± 494 |
| V2 | 705 ± 75 | 709 ± 42 | 1400 ± 85 | 1385 ± 98 | 4669 ± 677 | 4082 ± 620 |
| V3 | 737 ± 68 | 712 ± 21 | 1455 ± 155 | 1402 ± 158 | 4565 ± 728 | 3877 ± 700 |
| V4 | 686 ± 79 | 695 ± 31 | 1448 ± 207 | 1378 ± 147 | 4085 ± 512 | 3924 ± 348 |
| V5 | 676 ± 81 | 693 ± 17 | 1425 ± 281 | 1401 ± 192 | 4473 ± 948 | 4061 ± 911 |
| V6 | 726 ± 99 | 698 ± 17 | 1395 ± 93 | 1400 ± 58 | 4129 ± 368 | 3236 ± 249 |
| V7 | 777 ± 63 | 744 ± 11 | 1426 ± 178 | 1409 ± 71 | 4445 ± 742 | 3878 ± 564 |
| $\overline{\mu} \pm \overline{\sigma}$ | 720 ± 78 | 712 ± 22 | 1428 ± 161 | 1402 ± 117 | 4437 ± 662 | 3908 ± 555 |
| $\overline{\text{SNR}}$ | 9 | 32 | 9 | 12 | 7 | 7 |

**Table 5.2:** In vivo measurements. Listed are means ($\mu$) and standard deviations ($\sigma$) obtained in the RoI analysis of the in vivo measurement. The RoIs were placed in WM, GM and CSF areas of the $T_1$ maps of all 7 volunteers (V1-V7). The different $T_1$ values correspond to the IR-MAP reconstruction and the fully sampled reference (REF). The last two rows depict the means ($\overline{\mu}$) and standard deviations ($\overline{\sigma}$) over all volunteers as well as the corresponding mean signal-to-noise ratio $\overline{\text{SNR}}$ calculated according to Eq. 5.4. Table from [96].

### 5.5.2 In Vivo Measurements

All observations regarding the noise-increase of the IR-MAP reconstructions compared to the reference can be explained similar to the phantom measurements. Due to the nature of radial sampling patterns, the two-fold undersampling of the reference dataset should only lead to negligible streaking artifacts and therefore only a small loss in spatial resolution. Therefore, it was assumed that the additionally appearing blurriness of the reference $T_1$ maps resulted from motion of the volunteers, which seems unavoidable for the lengthy acquisition of $\sim 30\,\text{min}$. This hypothesis is confirmed by the considerably sharper appearance of the IR-MAP reconstructed $T_1$ maps, each of which was acquired in only 6 s, and which are therefore much less susceptible to motion artifacts. If regions of high $T_1$ values extend to only one or two pixels, motion of the subject smears out each of these values over a small region of several pixels, leading to lower $T_1$ values in these regions. Due to the very fast acquisition process, less motion can occur in IR-MAP reconstructions, leading to much less pronounced blurring and therefore an improved accuracy in $T_1$.

The reproducibility study showed no changes in WM and GM for repeated measurements of the same FoV. The decreasing $T_1$ values in the CSF can be explained by the relaxation breaks of only 15 s that were used to ensure a complete relaxation of the magnetization before each IR-LL measurement. While 99.9 % of the magnetization will be relaxed for $T_1 < 2000\,\text{ms}$, less than 98 % will be relaxed for $T_1 > 4000\,\text{ms}$, leading to errors in a quantification of $T_1$ using Eq. 2.9. In conjunction with the motion-induced

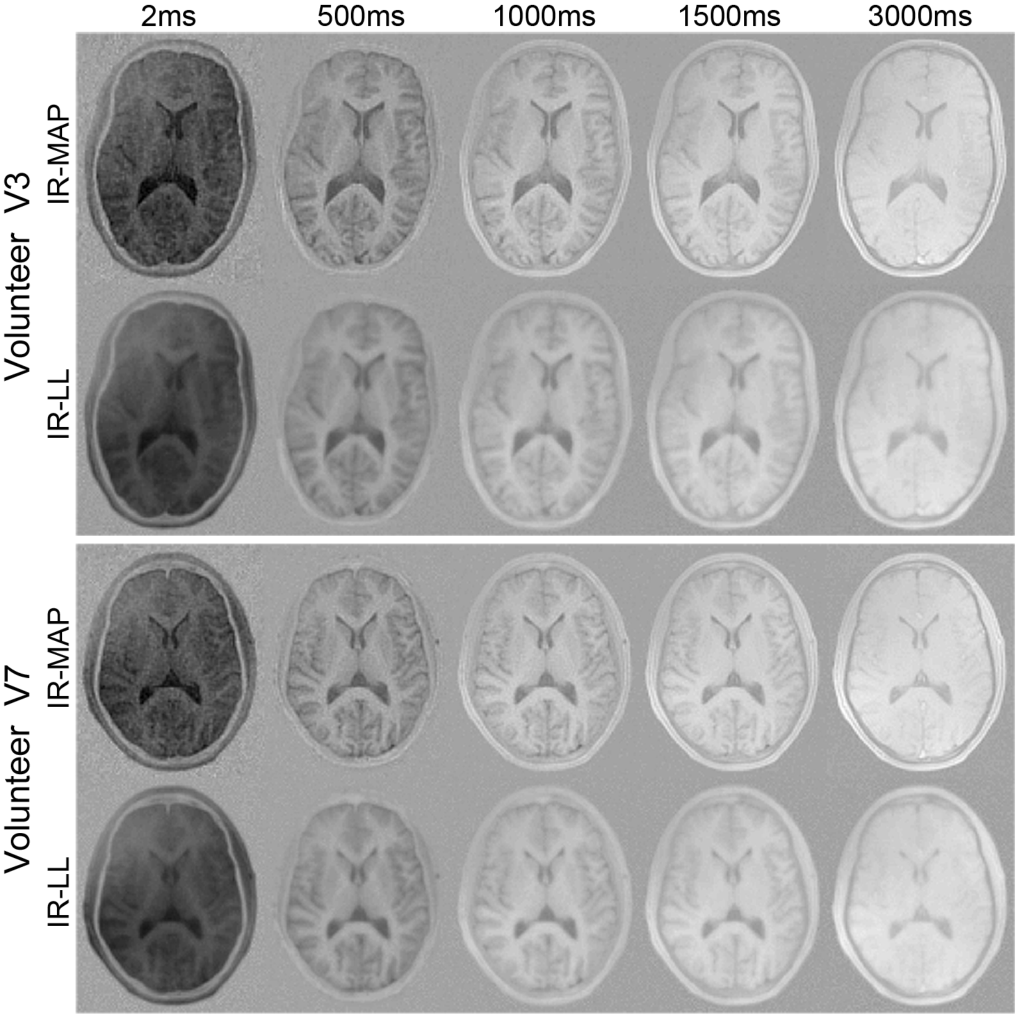

**Figure 5.6:** In vivo images. IR-MAP reconstruction (top) and segmented IR-LL FLASH reference (bottom) of volunteers V3 and V7 at exemplary inversion times. Figure from [96].

$T_1$ reduction mentioned above, this effect explains the smaller $T_1$ values observed in the CSF of the in vivo reference. With a proper waiting time between successive acquisitions, the reproducibility of IR-MAP could be ensured even in regions of higher $T_1$ such as the CSF. Such an acquisition, however, would be impractical for in vivo studies due to unacceptably long scan times. Alternatively, a correction method for insufficient relaxation times between subsequent inversions as described in section 2.8 could be used.

Although there is a wide range of literature WM and GM values, the $T_1$ values of GM obtained in this study (ranging from 1395 ms to 1455 ms) are in good agreement to many literature values [30, 65, 110] with a range from 1331 ms to 1470 ms. Although the values of WM (ranging from 676 ms to 777 ms) are smaller than many literature values for overall WM such as 832 ms in [106], it is in agreement with the value of 761ms found in [110] for frontal WM. Due to the large standard deviation within the RoIs of the CSF, these values were not compared to other literature.

### 5.5.3 Comparison of IR-MAP and SR-MAP

The proposed IR-MAP algorithm addresses some of the major issues of the SR-MAP algorithm presented in the previous chapter. The most important change is the IR pulse which is used instead of the SR pulse for magnetization preparation. Instead of an effective relaxation parameter $T_1^*$, one can now obtain $T_1$ independently of the flip angle from the three independent fit parameters $T_1^*$, $M_0^*$ and $M_0$. Additionally, the use of IR pulses results in an SNR gain in comparison to SR-prepared sequences, where the magnetization is initially zeroed. This can lead to a very low SNR especially for the radial projections acquired directly after the SR pulse and therefore causes an inevitable introduction of noise by the data consistency condition in step 4 of the algorithm (section 3.2). A drawback of the IR preparation is the additional relaxation time needed for reaching the equilibrium magnetization before subsequent IR-LL acquisitions which was already addressed in the previous section. This leads to a considerably longer scan time if multiple subsequent parameter maps are to be acquired.

Another limitation of the initial SR-MAP implementation, which is not connected to the type of magnetization preparation used, was the assumption of a mono-exponential relaxation in every voxel. Despite the advantage of a low numerical complexity of the fit, this can lead to systematic errors in image regions or voxels not complying with this model such as voxels containing various types of tissue [94]. To avoid such problems, a multi-exponential fit of up to three mono-exponentials was allowed in the dictionary look-up used in this IR-MAP implementation. In addition, imperfect slice profiles caused by the very short excitation pulses typically used in fast imaging sequences can cause variations of the flip angle $\alpha$ within the excited slice as described in section 2.9. This problem was addressed by adding mono-exponentials of different flip angles to the dictionary used for the model fit. A more sophisticated correction method will be presented in chapter 8.

### 5.5.4 Dependence of the Accuracy of the $T_1$ Estimates on the Temporal Coverage

As described in section 4.5.4, the exponential slope as well as the steady-state magnetization $M_0^*$ have to be covered in every pixel to ensure a quantification of $T_1$ with sufficient accuracy. All sequence parameters have to be chosen accordingly to fulfill this condition. For 1000 projections acquired with a repetition time $T_R = 6\,\text{ms}$ and a flip angle $\alpha = 7°$, as they were acquired in the experiments of this work, $M_0^*$ would be covered even for very large $T_1$ values of about 4000 ms as they would only occur in tissues with an extremely high water content such as the CSF. This ensures an accurate quantification of $T_1$.

### 5.5.5 Duration of the IR-MAP Algorithm

In our implementation, one iteration of the dictionary-based algorithm lasted 90 s for a dataset with 1000 time steps $T_I$ and a $256 \times 256$ image matrix. In comparison, a mono-exponential fit of the same matrix would take 86 s on the same CPU using standard MATLAB libraries. In both cases, this time is proportional to the number of pixels in the image matrix. For dictionary-based model fitting, the reconstruction time additionally depends on the size of the dictionary. A straightforward and therefore quite lengthy implementation of the dictionary look-up was used in this work to demonstrate the functionality of the method. However, the duration of the look-up for an entire dataset can be reduced by starting with a broad spacing of the parameters $T_1$ and $\alpha_0$ used in the dictionary of the first look-up which is recursively reduced in multiple iterations. As the look-up is performed in a sequential fashion for the individual pixels, there is also a great potential of speeding up the algorithm by parallelizing the implementation.

### 5.5.6 Comparison of IR-MAP to Existing $T_1$ Mapping Techniques

Many other $T_1$ mapping techniques have been proposed, some of which achieve full brain coverage with 1 mm in-plane resolution in less than 10 min. Most techniques based on the LL approach apply inversion pulses, followed by a LL acquisition, to track the LL relaxation process and subsequently use a fit similar to Eq. 2.9 to obtain a $T_1$ map. For a sufficiently high temporal and spatial resolution, the acquisition is performed in a segmented fashion using multiple inversions [19, 67, 82]. These approaches offer whole brain coverage with a slice thickness of up to 2 mm and an in-plane resolution of 1 mm with a total acquisition time of less than 10 min, leading to an effective acquisition time of about 20 s per slice. However, due to the segmented acquisition of the entire volume, the data needed to obtain the $T_1$ map of a single slice are collected after multiple sequential inversion pulses. Therefore, the temporal resolution for obtaining the $T_1$ map of a single slice using these techniques would therefore be considerably worse than the 6 s achieved using IR-MAP.

The VFA technique is another popular approach for $T_1$ mapping enabling an even better spatial resolution (see section 2.7). Using this approach, the 3D acquisition of a whole brain $T_1$ map with an isotropic resolution of 1 mm is possible in less than 8 min [22]. These measurements require the exact knowledge of the flip angle, leading to potential errors due to $B_1$ field inhomogeneities and slice profile imperfections. Due to the broad excitation profiles of fast RF pulses typically used in 2D acquisitions, a reliable $T_1$ map with a slice thickness of 1 mm would be hard to obtain using a VFA technique. As the slice profile errors are relatively low in the center portion of 3D slabs, most implementations of the VFA technique use 3D acquisitions. Similar to the LL-based approaches, the temporal resolution of the $T_1$ map of a single slice therefore corresponds to the acquisition time of the entire 3D volume.

In contrast to the methods described above, IR-MAP has a slightly lower spatial resolution of up to 1.6 mm × 1.6 mm × 4 mm, but no segmentation is necessary, enabling a self-contained acquisition of a single-slice $T_1$ map in 6 s. This is advantageous for applications such as dynamic $T_1$ mapping where a better temporal resolution is required (see chapter 6).

# 6 MAP for Dynamic Contrast-Enhanced $T_1$ Mapping

## 6.1 Introduction

Although the model-based IR-MAP reconstruction which was presented in chapter 5 greatly reduces the acquisition time needed for obtaining one $T_1$ map, the requirement of long waiting periods between two consecutive IR pulses leads to a significant delay between two subsequently acquired $T_1$ maps and therefore a poor temporal resolution of dynamic series. To circumvent prolonged waiting periods, a correction as described in section 2.8 can be applied to correct for $T_1$ errors introduced by insufficient relaxation, and thus enable a reduction of the waiting period.

In this chapter, the IR-MAP algorithm was applied for dynamic contrast-enhanced $T_1$ mapping: Multiple radial IR-LL FLASH acquisitions are consecutively performed, each followed by an insufficiently short waiting period (e.g. 3 s) for relaxation. Next, IR-MAP is used to reconstruct an individual $T_1$ map for each of these acquisitions. Finally, $T_1$ errors caused by the insufficient relaxation between subsequent IR pulses are iteratively corrected as described in section 2.8. After the method was implemented and validated in *Würzburg*, it was applied for dynamic $T_1$ mapping of a brain tumor patient in cooperation with Dr. Sotirios Bisdas and Prof. Dr. Uwe Klose at the *Department of Diagnostic and Interventional Neuroradiology, Eberhard Karls University, Tübingen, Germany.*

Some of the content of this chapter has been published in [53, 93]. The permission to reuse images and text from this publication was granted by the *International Society for Magnetic Resonance in Medicine.* Reused images are marked in the image caption.

## 6.2 Methods

All imaging experiments were carried out on a 3 T whole-body scanner (MAGNETOM Trio, Siemens AG Healthcare Sector, Erlangen, Germany) employing a 12 channel (*Würzburg*) or a 32 channel phased-array head coil (*Tübingen*) for signal reception.

All post-processing was performed on a standard desktop PC equipped with an Intel Core i7-2600 CPU (3.4 GHz) using MATLAB (The MathWorks, Natick, MA).

All in vivo studies were approved by the relevant local ethics committee. Written informed consent was obtained from each volunteer prior to scanning.

### 6.2.1 Implementation of IR-MAP

An implementation of IR-MAP as described in section 5.2 was used for all IR-MAP reconstructions performed in this chapter.

### 6.2.2 Acquisition and Reconstruction Scheme

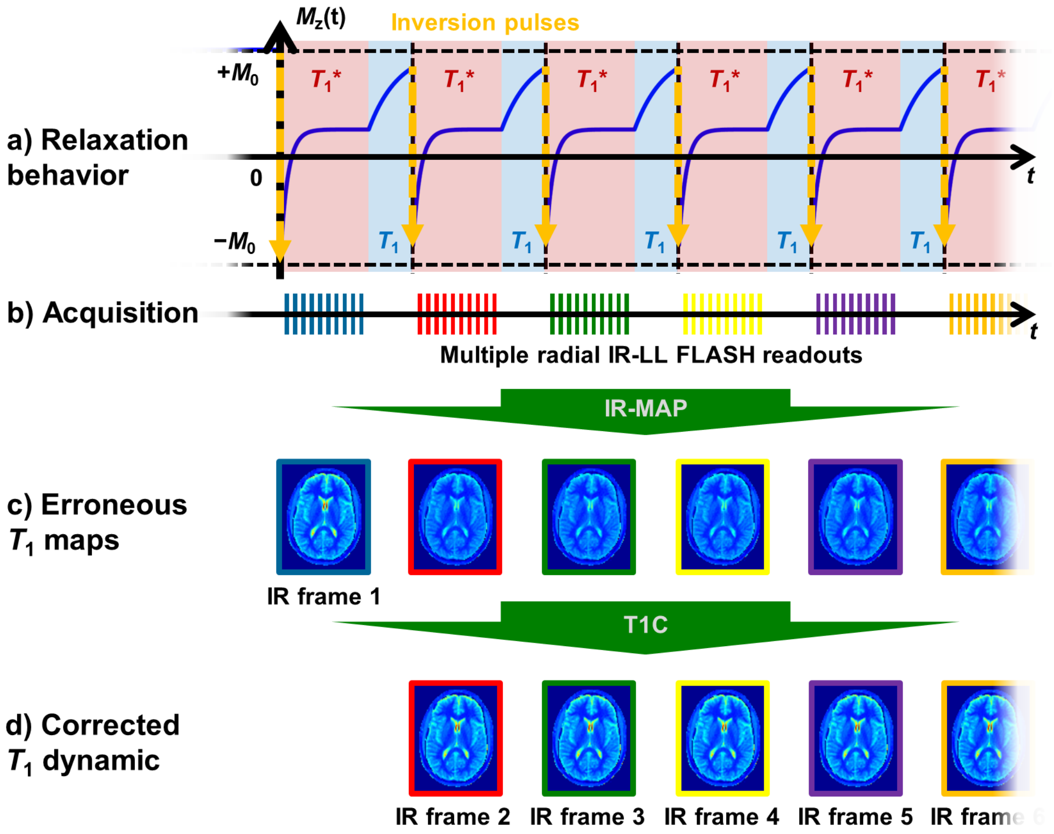

**Figure 6.1:** Acquisition and reconstruction scheme. The acquisition scheme including multiple consecutive IR pulses and the subsequent relaxation behavior is indicated in (a). Each of these IR frames consists of an acquisition period of $T_1^*$ relaxation (red background) followed by a waiting period of undisturbed $T_1$ relaxation (blue background). After the acquisition (b), the IR-MAP algorithm is used to obtain one $T_1$ map for each IR frame (c). Finally, potential errors caused by an insufficient waiting period are corrected using T1C. Modified Figure from [93].

The acquisition and reconstruction scheme illustrated in Figure 6.1 was used for all experiments in this work. Each of the so-called IR frames consists of the following steps:

1. Global inversion pulse, followed by a very short time period of pure $T_1$ relaxation before the application of the first RF excitation pulse (blue background in Fig. 6.1a).
2. Radial IR-LL FLASH acquisition of $T_1^*$ relaxation (red background in Fig. 6.1a).
3. Waiting period of pure $T_1$ relaxation (blue background in Fig. 6.1a) before the next IR pulse initiates the next IR frame.

After data collection, the IR-MAP algorithm (see chapter 5) was applied separately to the radial IR-LL FLASH datasets of all IR frames to obtain $M_A$, $M_B$ and $T_1^*$ in every pixel (Fig. 6.1c). While an adjusted Eq. 2.9

$$T_1 = T_1^* \cdot \left[ (M_A - M_B)/M_A - 1 \right] . \tag{6.1}$$

with $M_0^* \to M_A$ and $M_0 \to -M_B$ was used to obtain a $T_1$ map of the first IR frame, the T1C correction presented in section 2.8 was applied to the parameter sets $(M_A, M_B, T_1^*)$ of the remaining IR frames to correct for errors caused by insufficient relaxation. The result was a set of $T_1$ maps containing the $T_1$ dynamic of the acquisition (Fig. 6.1d).

### 6.2.3 Determination of the Quality of Inversion *K*

In the $T_1$ correction described in chapter 2.8, a parameter $K$ was introduced that describes the quality of the inversion pulse (0: no inversion, 1: perfect inversion), and that is required for the T1C correction. To avoid a separate measurement for determining $K$, a method for the estimation of $K$ was developed. It was assumed that the magnetization is at equilibrium before this first inversion pulse and that no $T_1$ changes occur between the first two acquired IR frames. First, $T_1$ of the first IR frame was obtained using IR-MAP and Eq. 6.1, as no correction had to be carried out. Next, IR-MAP was applied to the second IR frame, followed by the iterative T1C method for $T_1$ correction. To see the influence of different $K$ values on T1C, the correction was performed for different inversion coefficients $K$ ranging from 0.7 to 1.0. The K values leading to the smallest $T_1$ difference between the first and the second IR frame best describe the efficiency of the inversion pulse used in the particular setup. Therefore, a map describing the inversion efficiency $K$ can be generated by performing this comparison for all pixels. As the inversion coefficient was expected to have a continuous behavior, a $3 \times 3$ median filter was applied to smoothen the $K$ map before any corrections were carried out. Using this $K_{\text{smooth}}$ map, $T_1$ was corrected for all IR frames affected by insufficient relaxation, that is all but the first IR frame.

### 6.2.4 Validation Study: Phantom

A validation study was performed using a phantom consisting of 7 vials with different CA (Resovist®, Bayer Schering Pharma AG, Germany) concentrations. A set of 5 subsequent IR frames was acquired (FoV: $200 \times 200 \times 4\,\mathrm{mm}^3$, $T_R$: 6 ms, $T_E$: 2.5 ms, $\alpha$: 7°, projections: 1000, readout points: 128, acquisition period: 6 s, waiting period: 3 s, $T_{\mathrm{IR}}$: 9 s) using the 12 channel coil for signal reception. After data collection, the first two IR frames were used to estimate the inversion efficiency $K_{\mathrm{smooth}}$. Subsequently, 50 IR-MAP iterations, followed by 100 iterations of the T1C correction (for all but the first IR frame) were applied to obtain one $T_1$ map for each IR frame. The acquisition period of 6 s combined with the waiting period of 3 s resulted in a temporal resolution of one $T_1$ map every 9 s.

To illustrate the errors caused by the insufficient relaxation period, $T_1$ values simply calculated using Eq. 6.1 were compared to the values after T1C correction. This was achieved by a RoI analysis of the first (without correction) and the fifth IR frame (before and after correction). In each of the compartments, mean values ($\mu$), standard deviations ($\sigma$) and relative errors ($\sigma/\mu$) were determined. Additionally, the percentage difference was calculated between the undisturbed first IR frame and the two $T_1$ maps of the fifth IR frame affected by insufficient relaxation.

### 6.2.5 Validation Study: Healthy Volunteer

To validate the technique in vivo, $T_1$ maps of the brains of 7 healthy volunteers aged between 23 and 30 years were acquired using the same sequence as in the phantom study with a FoV ranging from $200 \times 200\,\mathrm{mm}^2$ to $220 \times 220\,\mathrm{mm}^2$. Again, the 12 channel coil was used for signal reception. After IR-MAP reconstruction and T1C correction (performed exactly as in the phantom validation study), the functionality of the $T_1$ correction was validated by a RoI analysis in WM, GM and CSF of the first (without correction) and the fifth IR frame (after 100 iterations of the T1C correction).

### 6.2.6 Clinical DCE-MRI Examination

To test the dynamic $T_1$ mapping technique in a clinical setting, a DCE-MRI experiment was performed on a patient with primary lymphoma using the 32 channel coil for signal reception. This time, 33 IR frames were acquired with the described acquisition (FoV: $230 \times 230 \times 3\,\mathrm{mm}^3$, $T_R$: 6 ms, $T_E$: 2.5 ms, $\alpha$: 7°, projections: 1000, readout points: 128, acquisition period: 6 s, waiting period: 3 s, $T_{\mathrm{IR}}$: 9 s) to track $T_1$ changes after the intravenous injection of CA (Gadovist®, Bayer Schering Pharma AG, Germany).

After five IR-MAP iterations, the $T_1$ maps before and after 100 iterations of the T1C correction were compared. Additionally, a RoI analysis was performed in normal WM, in the tumor regions and in the vein to visualize the effect of the T1C correction for the dynamic $T_1$ series.

## 6.3 Results

### 6.3.1 Validation Study: Phantom

Figure 6.2 shows results of the phantom experiment. In the first column (a), a $T_1$ map of the first IR frame (top) as well as the areas used for the RoI analysis (bottom) are depicted. The second column (b) shows the uncorrected $T_1$ map of the fifth IR frame (top) as well as a two-fold difference from the undisturbed first IR frame (bottom). In the third column (c), the $T_1$ map of the fifth IR frame after the T1C correction (top) and a two-fold difference from the undisturbed first IR frame (bottom) are displayed. While differences from the undisturbed $T_1$ map of the first IR frame are clearly visible in the uncorrected $T_1$ map of the fifth IR frame especially in vials of large $T_1$ values (vials E-G), they are considerably reduced by the $T_1$ correction. This observation is further illustrated in the difference images. While there are clearly visible deviations before the $T_1$ correction in vials D-G, the differences are greatly reduced by the $T_1$ correction.

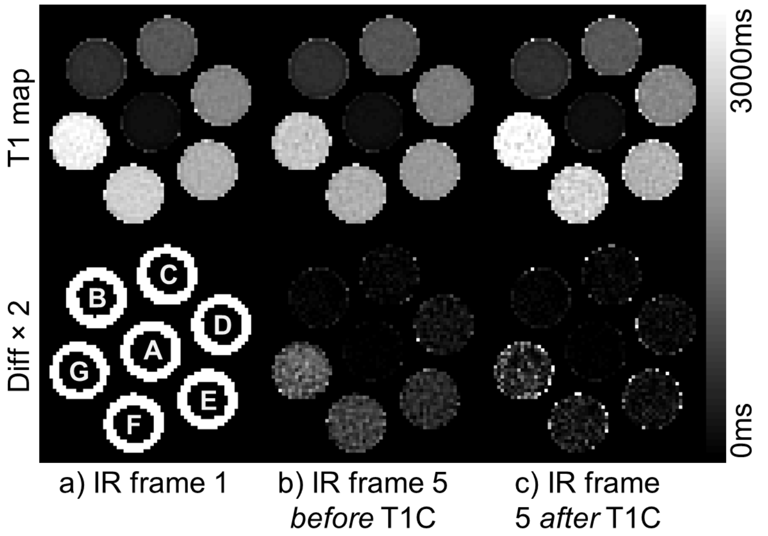

**Figure 6.2:** Phantom validation study. $T_1$ maps of the undisturbed first IR frame (a) and the uncorrected (b) as well as the corrected fifth IR frame (c) obtained in the phantom are shown in the upper part. In the lower part, the areas of vials A-G used for the RoI analysis are depicted and a two-fold difference for (b) and (c) with respect to (a) is given.

Figure 6.3a plots the $T_1$ values of the first IR frame against the $T_1$ values of the fifth IR frame before (red, top) and after (blue, bottom) the T1C correction. Before the correction, a systematic underestimation of $T_1$ increasing with the absolute value of $T_1$ can be observed. This systematic deviation is considerably reduced using the T1C correction. However, a slight overestimation is introduced by T1C for some of the higher $T_1$ values.

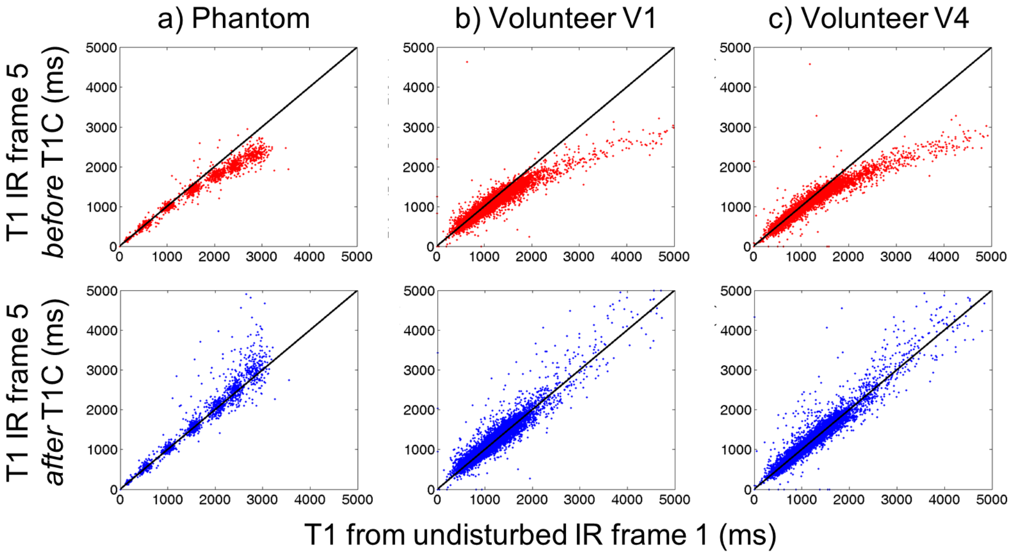

**Figure 6.3:** Functionality of the T1C correction. Shown are plots of the undisturbed $T_1$ values of the first IR frame (horizontal axis) against the uncorrected (red, top) and corrected (blue, bottom) $T_1$ values for the phantom experiment (a) as well as for two exemplary volunteers V1 (b) and V4 (c).

Finally, the inversion coefficient $K_{\text{smooth}}$ is depicted in Figure 6.4a. It shows a good inversion efficiency of ~ 100 % across the entire phantom.

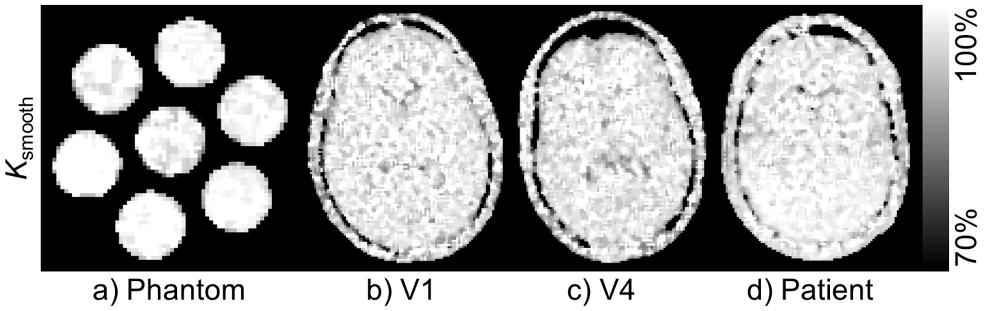

**Figure 6.4:** Quality of inversion. Shown are the inversion coefficients $K_{\text{smooth}}$ smoothened using a $3 \times 3$ median filter obtained for the phantom experiment (a) as well as for two exemplary volunteers V1 (b) and V4 (c) and the patient (d).

The RoI analysis in Table 6.1 underlines the good accordance between the $T_1$ maps of the undisturbed first IR frame and the T1C-corrected fifth IR frame. While the uncorrected $T_1$ maps show percentage differences of up to 19.8 % for the largest $T_1$ in the order of 3 s (vial G), they can be reduced to less than 4.2 % by the $T_1$ correction. For very small $T_1$ values around 200 ms, the correction has only little effect, with a difference remaining at 1.0 %. The reconstruction exhibits a good visual quality, which is underlined by an average relative error of less than 4.6 % in the individual RoIs. Despite a small increase of the standard deviation within the RoIs in the process of the T1C correction, the average relative error over all vials remains at an acceptable amount of 6.3 % after the correction.

| | IR frame 1 | | IR frame 5 before T1C | | | IR frame 5 after T1C | | |
|---|---|---|---|---|---|---|---|---|
| Vial | $\mu \pm \sigma$ (ms) | $\sigma/\mu$ (%) | $\mu \pm \sigma$ (ms) | $\sigma/\mu$ (%) | diff (%) | $\mu \pm \sigma$ (ms) | $\sigma/\mu$ (%) | diff (%) |
| A | $202 \pm 15$ | 7.3 | $200 \pm 15$ | 7.6 | 1.0 | $200 \pm 15$ | 7.6 | 1.0 |
| B | $573 \pm 38$ | 6.7 | $568 \pm 31$ | 5.5 | 0.9 | $569 \pm 31$ | 5.5 | 0.8 |
| C | $1047 \pm 46$ | 4.4 | $1019 \pm 43$ | 4.3 | 2.7 | $1041 \pm 49$ | 4.7 | 0.6 |
| D | $1574 \pm 57$ | 3.6 | $1465 \pm 54$ | 3.7 | 6.9 | $1573 \pm 74$ | 4.7 | 0.1 |
| E | $2064 \pm 61$ | 3.0 | $1807 \pm 62$ | 3.4 | 12.5 | $2068 \pm 106$ | 5.1 | 0.2 |
| F | $2430 \pm 71$ | 2.9 | $2043 \pm 91$ | 4.4 | 15.9 | $2476 \pm 173$ | 7.0 | 1.9 |
| G | $2868 \pm 118$ | 4.1 | $2299 \pm 121$ | 5.2 | 19.8 | $2988 \pm 288$ | 9.6 | 4.2 |
| **AVG** | - | **4.6** | - | **4.9** | - | - | **6.3** | - |

**Table 6.1:** Phantom experiments. Shown are means ($\mu$), standard deviations ($\sigma$) and the relative error ($\sigma/\mu$) of $T_1$ in vials A-G of the phantom. The columns contain $T_1$ values obtained from IR frame 1 and IR frame 5 before as well as after the T1C correction. Additionally, the percentage difference between the uncorrected and the corrected means is given.

### 6.3.2 Validation Study: Healthy Volunteers

Results of the in vivo validation experiment are depicted in Figure 6.5. Again, the $T_1$ map of the undisturbed first IR frame (a) is depicted together with the $T_1$ maps of the fifth IR frame before (b) and after the $T_1$ correction (c) for two exemplary volunteers V1 and V4. As in the phantom experiment, substantial differences before the $T_1$ correction occur especially for large $T_1$ values such as the CSF but also the GM. Again, they are greatly reduced by the $T_1$ correction, leaving recognizable differences only in small areas of the CSF.

As in the phantom experiment, Figures 6.3b-c plot the correlation between the $T_1$ values of the first IR frame and the $T_1$ values of the fifth IR frame before (red, top) and after the T1C correction (blue, bottom) for the same volunteers. Again, the initial systematic deviation can be considerably reduced using the T1C correction.

As expected, the corresponding inversion coefficients $K_{\text{smooth}}$, which are depicted in Figures 6.4b-c show a good inversion efficiency of ~ 100 % over the major part of the object.

The RoI analysis shown in Table 6.2 provides a quantitative proof of these observations. It shows means and standard deviations for $T_1$ of the first IR frame and the fifth IR frame before and after T1C correction in WM, GM and CSF areas of all 7 volunteers.

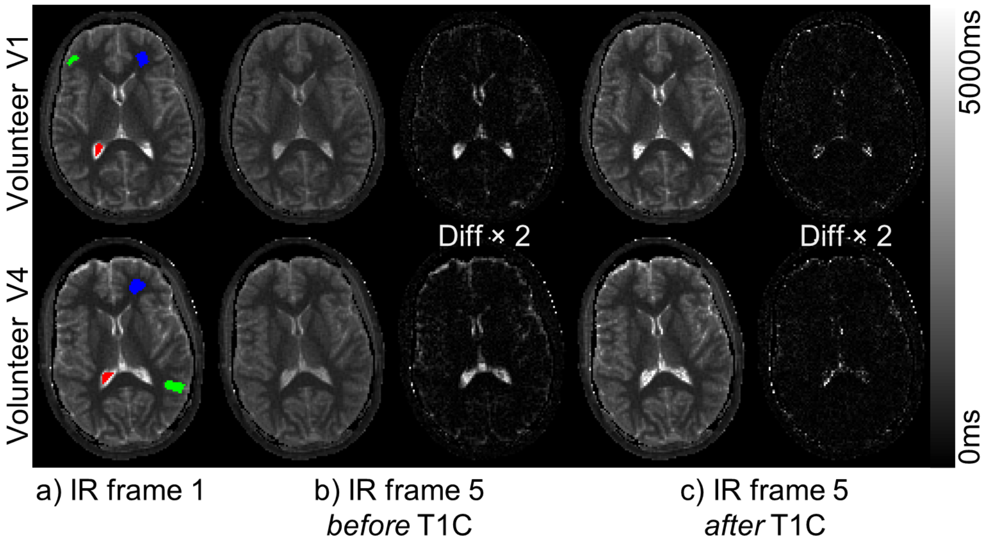

**Figure 6.5:** In vivo validation study. Shown are the $T_1$ maps of the undisturbed first IR frame (a) and the uncorrected (b) as well as the corrected fifth IR frame (c) obtained for volunteers V1 and V4. Additionally, a two-fold difference to (a) is given. The areas of WM (blue), GM (green) and CSF (red) used for the RoI analysis are indicated in (a).

While the average percentage difference over all volunteers remains almost unchanged for WM before (1.7 %) and after the correction (1.8 %), it can be considerably reduced in GM (7.4 % to 3.6 %) as well as in the CSF (37.7 % to 7.5 %).

### 6.3.3 Clinical DCE-MRI Examination

Results of the dynamic contrast-enhanced $T_1$ mapping experiment are shown in Figure 6.6. It depicts the $T_1$ dynamic in the brain of the examined patient with a temporal resolution of one $T_1$ map every 9 s. $T_1$ maps before (a) and after the $T_1$ correction (b) are depicted for the first 12 IR frames. In the exceptional case of the undisturbed first IR frame (at 0 s), both the top as well as the bottom part show the same uncorrected $T_1$ map. As in the validation study, there is a systematic difference between the uncorrected and the corrected $T_1$ maps for all subsequent IR frames growing with the order of $T_1$. This error is best visible between the undisturbed first IR frame (at 0 s) and the second IR frame (at 9 s). After the T1C correction, no visible deviations remain. The effect of the CA on $T_1$ becomes noticeable after about 45 s with a decrease in $T_1$ in areas permeated by the CA.

A RoI evaluation of the temporal $T_1$ changes is shown in Figure 6.7. The upper left part (a) shows $T_1$ maps of the first and the last acquired IR frame with the RoIs indicated in different colors, while the other parts (b-f) depict the $T_1$ dynamic in these RoIs before (crosses) and after T1C correction (solid lines). While the signal in the area of normal WM (c: blue) remains in a similar range over the entire time series, a clear $T_1$ reduction

| Region of Interest | | IR frame 1 | IR frame 5 before T1C | | IR frame 5 after T1C | |
|---|---|---|---|---|---|---|
| | | $\mu \pm \sigma$ (ms) | $\mu \pm \sigma$ (ms) | diff (%) | $\mu \pm \sigma$ (ms) | diff (%) |
| WM | V1 | 738 ± 85 | 752 ± 83 | 1.9 | 755 ± 87 | 2.3 |
| | V2 | 726 ± 91 | 741 ± 117 | 2.1 | 745 ± 122 | 2.6 |
| | V3 | 735 ± 68 | 725 ± 56 | 1.3 | 727 ± 57 | 1.0 |
| | V4 | 714 ± 86 | 721 ± 85 | 1.0 | 723 ± 87 | 1.3 |
| | V5 | 680 ± 54 | 680 ± 75 | 0.1 | 682 ± 76 | 0.4 |
| | V6 | 703 ± 81 | 716 ± 91 | 1.9 | 718 ± 93 | 2.2 |
| | V7 | 783 ± 74 | 755 ± 64 | 3.5 | 758 ± 66 | 3.2 |
| | **AVG** | **725 ± 77** | **727 ± 81** | **1.7** | **730 ± 84** | **1.8** |
| GM | V1 | 1386 ± 205 | 1286 ± 139 | 7.2 | 1331 ± 168 | 4.0 |
| | V2 | 1373 ± 106 | 1301 ± 112 | 5.3 | 1357 ± 135 | 1.2 |
| | V3 | 1318 ± 241 | 1239 ± 203 | 6.0 | 1286 ± 237 | 2.4 |
| | V4 | 1376 ± 211 | 1267 ± 162 | 7.9 | 1325 ± 198 | 3.7 |
| | V5 | 1381 ± 280 | 1279 ± 203 | 7.4 | 1334 ± 244 | 3.4 |
| | V6 | 1427 ± 110 | 1278 ± 85 | 10.4 | 1331 ± 101 | 6.7 |
| | V7 | 1409 ± 151 | 1301 ± 113 | 7.6 | 1357 ± 139 | 3.7 |
| | **AVG** | **1381 ± 186** | **1279 ± 145** | **7.4** | **1332 ± 175** | **3.6** |
| CSF | V1 | 4183 ± 723 | 2572 ± 304 | 38.5 | 4288 ± 851 | 2.5 |
| | V2 | 4428 ± 609 | 2696 ± 334 | 39.1 | 4821 ± 810 | 8.9 |
| | V3 | 3704 ± 880 | 2395 ± 401 | 35.3 | 3757 ± 1032 | 1.5 |
| | V4 | 4157 ± 434 | 2476 ± 182 | 40.4 | 3765 ± 592 | 9.4 |
| | V5 | 4317 ± 1043 | 2658 ± 579 | 38.4 | 4903 ± 1149 | 13.6 |
| | V6 | 4001 ± 417 | 2552 ± 113 | 36.2 | 3845 ± 429 | 3.9 |
| | V7 | 4081 ± 715 | 2625 ± 405 | 35.7 | 4596 ± 923 | 12.6 |
| | **AVG** | **4124 ± 689** | **2568 ± 331** | **37.7** | **4282 ± 827** | **7.5** |

**Table 6.2:** In vivo validation study. Shown are means ($\mu$) and standard deviations ($\sigma$) of $T_1$ in WM, GM and CSF regions of volunteers V1-V7. The columns contain $T_1$ values obtained from IR frame 1 and IR frame 5 before as well as after the T1C correction. Additionally, the percentage difference between the means of the undisturbed first IR frame and the uncorrected and corrected fifth IR frame is given. The last row contains the averages (AVG) over all 7 volunteers.

can be seen in the tumor regions (b: red, d: green, f: cyan). In the vein (e: magenta), $T_1$ is greatly reduced by the CA. As already observed in the validation studies, the uncorrected $T_1$ only slightly decreases in areas of relatively small $T_1$ such as the WM. This decrease becomes significantly larger for regions of higher $T_1$ such as the GM. In these regions, the effect of the T1C correction is most apparent as it successfully restores the $T_1$ plateaus before the CA inflow after about 45 s.

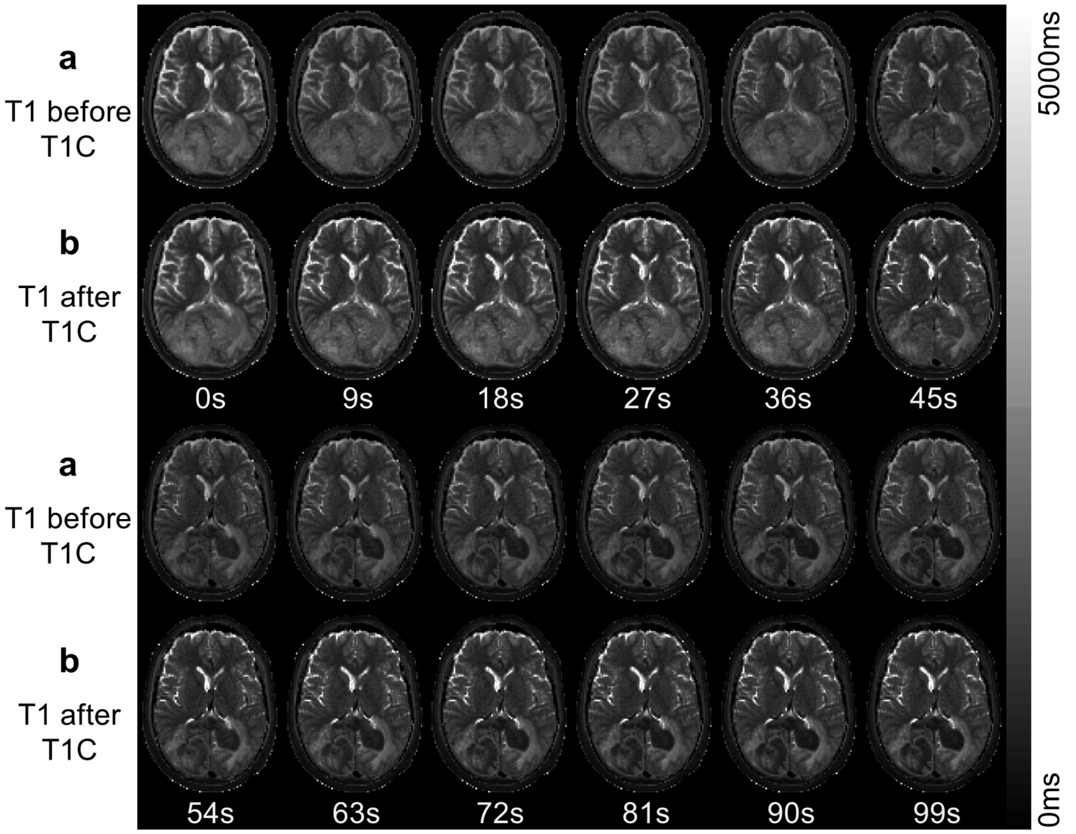

**Figure 6.6:** Clinical DCE-MRI example. Depicted are the first 12 IR frames of a dynamic $T_1$ mapping experiment performed on a patient with primary lymphoma. Shown are the uncorrected $T_1$ maps after the IR-MAP reconstruction (a) as well as the corrected $T_1$ maps after the application of T1C (b). Modified Figure from [93].

## 6.4 Discussion

### 6.4.1 Validation Study: Phantom

The results of the phantom validation study clearly indicate the functionality of the proposed method for dynamic $T_1$ mapping. Most importantly, the parameter maps obtained in the model-based IR-MAP reconstruction were of a good visual quality, which is underlined by an average standard deviation of less than 4.6 % in the individual RoIs. Also, the systematic error in $T_1$ which is caused by the insufficient relaxation time between two subsequent inversions and which is most clearly illustrated by the correlation plot in Figure 6.3a was greatly reduced by the T1C correction. In the most extreme case of vial G containing the liquid with the largest $T_1$ value, the error was reduced from 19.8 % before the correction to 4.2 % after the correction. Despite a minimal increase of the relative error within the RoIs in that process, its average over all vials remains at an acceptable amount of 6.3 % after the correction (before: 4.6 %).

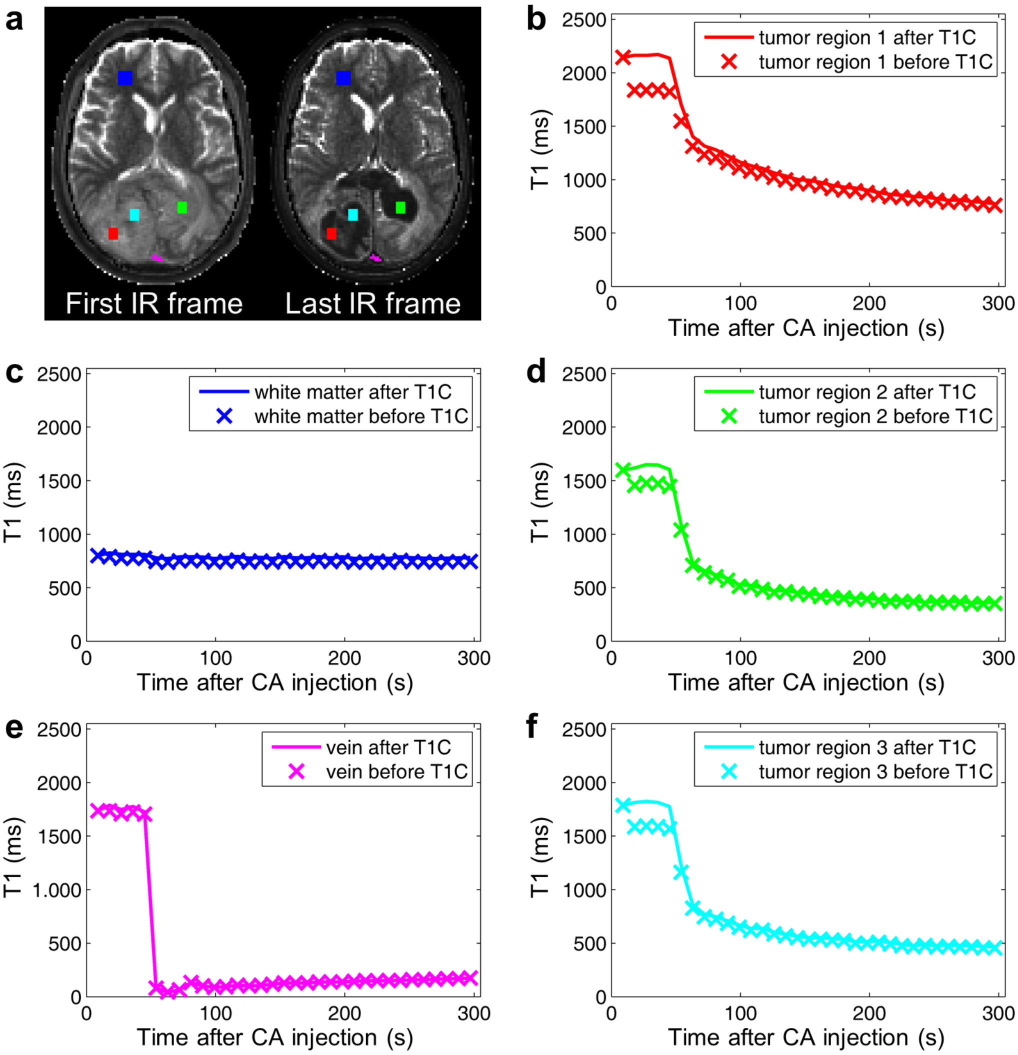

**Figure 6.7:** RoI analysis of the clinical DCE-MRI experiment. a: $T_1$ maps of the first and the last acquired IR frame with the positioning of the RoIs in tumor regions (red, green, cyan), in WM (blue) and in the vein (magenta) indicated. b-f: Dynamic of the mean $T_1$ values in the selected RoIs before (crosses, circles and diamonds) and after the T1C correction (solid line). Modified Figure from [53].

### 6.4.2 Validation Study: Healthy Volunteer

Similar to the phantom experiments, the results of the vivo validation study clearly suggest the functionality of the proposed method for in vivo measurements. Again, the $T_1$ maps obtained by IR-MAP are of a good visual quality with only an acceptable noise enhancement caused by the high acceleration. Additionally, the fact that the average difference to the undisturbed first IR frame was effectively reduced especially in areas of large $T_1$ underlines the capability of the T1C correction. As in the phantom experiments, this is most apparent in the correlation plots in Figure 6.3, but also from the percentage differences listed in Table 6.2. The average difference between the undisturbed first IR frame and the fifth IR frame affected by insufficient relaxation was reduced from up to 37.7 % before the correction to a maximum of 7.5 % after the application of T1C.

### 6.4.3 Clinical DCE-MRI Examination

The results of the clinical DCE-MRI measurement successfully demonstrate the capability of the proposed method for dynamic $T_1$ mapping. The effect of the insufficient relaxation time is nicely illustrated before the injection of the CA after about 45 s. Although no change in $T_1$ should be visible before that time point, $T_1$ is significantly altered between the first (0 s) and the second IR frame (9 s). As observed in the results section, this effect is most apparent in the $T_1$ time courses in Figures 6.7b,d,f, where the T1C correction successfully restores the $T_1$ plateaus in the tumor regions before the inflow of the CA. The injection of the CA is clearly visible in the vein (Fig. 6.7e). As soon as the CA is injected, it dissolves in the blood, significantly reducing its $T_1$ relaxation time and leading to an instant $T_1$ drop-off after about 45 s. Although a much higher reduction in $T_1$ is to be expected in the vein over a very short period of time, it is not visible in the time course due to an insufficient temporal resolution of 9 s between two $T_1$ maps. As the inverted blood is completely replaced by inflowing blood of an equilibrium magnetization between two IR frames, the effect of the inversion pulses of all previous IR frames is greatly reduced in these voxels of the FoV. Consequently, no changes due to an insufficient relaxation occur e.g. in the vein. As expected, $T_1$ in areas where the CA accumulates (such as the lymphoma) is significantly lowered after the CA injection.

### 6.4.4 Limitations of the Presented Combination of IR-MAP and T1C

A high functionality of the proposed combination of IR-MAP for $T_1$ mapping followed by the application of T1C to correct for $T_1$ errors due to an insufficient relaxation was demonstrated for all experiments performed in this work. There are, however, some difficulties and limitations of the approach which have to be considered before its application.

First of all, motion of the object during the acquisition of one IR frame can lead to errors in the reconstructed $T_1$ maps [94]. Similarly, motion between two IR frames can lead to inconsistencies in the mathematical descriptions of the relaxation process of two consecutive IR frames, potentially causing errors in the T1C correction. In DCE-MRI of the brain, however, the combination of little motion of the object and an acquisition time of 15 s for two consecutive IR frames is expected to cause little motion-related errors. Although only little motion should occur between two consecutive IR frames, changes in the object's position between the first and subsequent IR frames can lead to errors due to the inversion efficiency map $K$ which is calculated in each pixel of the FoV using only the first and the second IR frame. This problem is addressed by the application of a $3 \times 3$ median filter which smoothens the $K$ maps over several pixels and reduces the effects of sharp changes in the inversion efficiency, as they can e.g. occur in areas of low SNR, on the T1C correction.

Lastly, contrast differences between two IR frames caused by the CA injection in DCE-MRI can lead to errors in the T1C correction. In DCE-MRI measurements of brain tumors, however, contrast changes in the regions of interest where CA accumulates (such as the lymphoma in our patient) experience a very slow decrease in $T_1$ compared to the temporal resolution of 9 s per IR frame. Therefore, such errors can be expected to remain negligible for the DCE-MRI measurement in this chapter.

### 6.4.5 Temporal Resolution of the Presented Technique

In the presented implementation, the temporal resolution of 9 s was defined by an acquisition period of 6 s followed by a waiting period of 3 s. Either of these time periods could be shortened in order to obtain a higher temporal resolution.

### 6.4.6 Advantages of the Proposed Approach over Existing $T_1$ Mapping Techniques

As described in section 5.5.6, there is a variety of $T_1$ mapping techniques, some of which achieve full brain coverage with 1 mm in-plane resolution and up to 1 mm slice thickness in less than 8 min. However, segmented 3D acquisitions have to be used to achieve such high resolutions, in turn leading to low temporal resolutions that are insufficient for dynamic $T_1$ mapping. The segmentation also prevents a correction of insufficient relaxation delays similar to the T1C method. Instead, other approaches have to be used to shorten the waiting period between subsequent inversions.

For LL-based methods, saturation pulses combined with an appropriate delay can be applied prior to the global inversion pulse of each segment [67, 82], unfortunately also lowering the SNR of the acquisition (see section 2.6). Alternatively, slice-selective inversion pulses can be used to shorten the waiting period, requiring a thorough assessment of the inversion efficiency [19]. Both approaches offer whole brain coverage with a slice thickness of up to 2 mm and an in-plane resolution of 1 mm with a total acquisition time of less than 10 min, leading to an effective acquisition time of about 20 s per slice. However, each image representing one specific contrast of the relaxation process consists of data collected after multiple inversions and the temporal resolution of a dynamic $T_1$ mapping experiment using these techniques would therefore correspond to the total acquisition time, which is inappropriate for dynamic $T_1$ mapping.

Techniques based on the VFA approach (see section 2.7) enable the 3D acquisition of a whole brain $T_1$ map with 1 mm$^3$ isotropic voxels in less than 8 min [22]. As in the LL-based approaches, however, the temporal resolution of two subsequent $T_1$ maps would be equal to the acquisition time of the entire 3D volume, which is likewise inappropriate for DCE-MRI. In addition to the susceptibility to $B_1$ field inhomogeneities, which was already mentioned in section 5.5.6, the performance of VFA methods that use spoiled gradient echo acquisitions is dependent on the value of the RF increment used for RF spoiling (see section 2.1), which has to be corrected for [74].

In contrast, the proposed technique has a slightly lower spatial resolution of $1.6\,\text{mm} \times 1.6\,\text{mm} \times 3\,\text{mm}$, but no segmentation is necessary in the acquisition, enabling a self-contained acquisition of a single-slice $T_1$ map in 6 s. Therefore, only the presented combination of IR-MAP and the subsequent $T_1$ correction for insufficient relaxation offers a temporal and spatial resolution sufficient for dynamic $T_1$ mapping.

# 7 MAP for Arterial Spin Labeling Perfusion MRI in Small Animals

## 7.1 Introduction

As described in section 2.16, ASL performed with an ECG-triggered FAIR-LL FLASH sequence can be used for quantification of myocardial perfusion in small animals. In these acquisitions, varying heart rates as well as missed ECG-trigger pulses usually lead to variations in the inversion times $T_I$ of different phase encoding steps. This behavior is illustrated in the histogram in Figure 7.1, which depicts the logged inversion times of the first 3 s of a FAIR-LL FLASH acquisition performed on a healthy mouse (temporal bin size: 20 ms). Each color indicates the inversion times of all phase encoding steps that were used for reconstructing one image of the relaxation process.

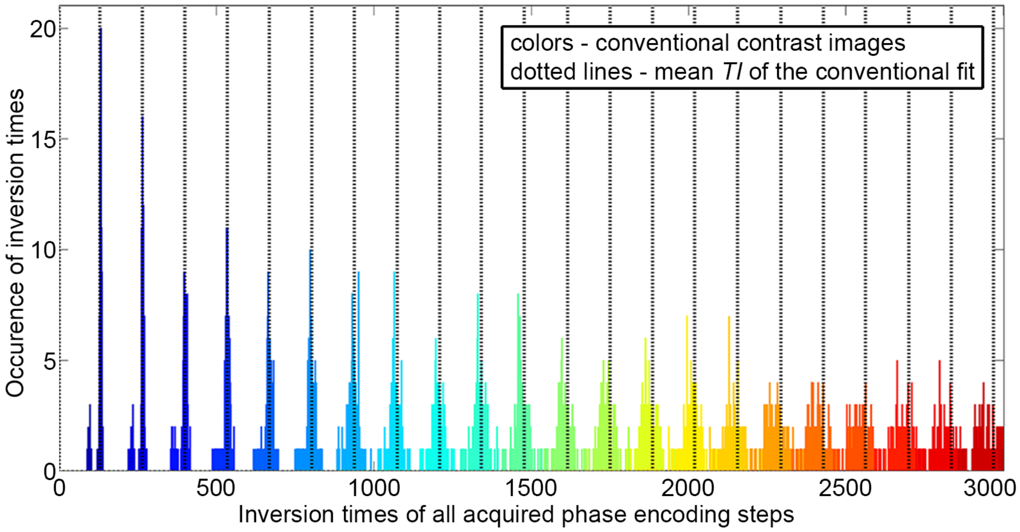

**Figure 7.1:** Partial histogram of all inversion times $< 3$ s logged in an ECG-gated, FAIR prepared LL FLASH acquisition. Figure from [95].

Variations in the heart rate occurring during the 20-25 min of acquisition lead to a $T_I$ distribution rather than a clearly defined single inversion time for each image of the relaxation process. The width of these distributions increases with the temporal distance to the inversion pulse, leading to a deterioration of the temporal resolution of the images with the inversion time. The use of averaged $T_I$ (dotted lines in Fig. 7.1) as it is performed in the conventional reconstruction is a source of error in the $T_1$ fit and therefore in the resulting perfusion values.

In this chapter, the MAP algorithm introduced in chapter 3 is adjusted for FAIR acquisitions to improve the temporal resolution of the image series of the relaxation process and the precision of the $T_1$ fit. For this purpose, the exact inversion time of each acquired phase encoding step was recorded during the experiment. Based on this time log, all phase encoding steps were assigned to bins of a temporal resolution of 20 ms. The result was a set of highly undersampled k-spaces which is illustrated in Figure 7.2. A modified version of the MAP algorithm was then used to reconstruct a full k-space for each of these undersampled k-spaces.

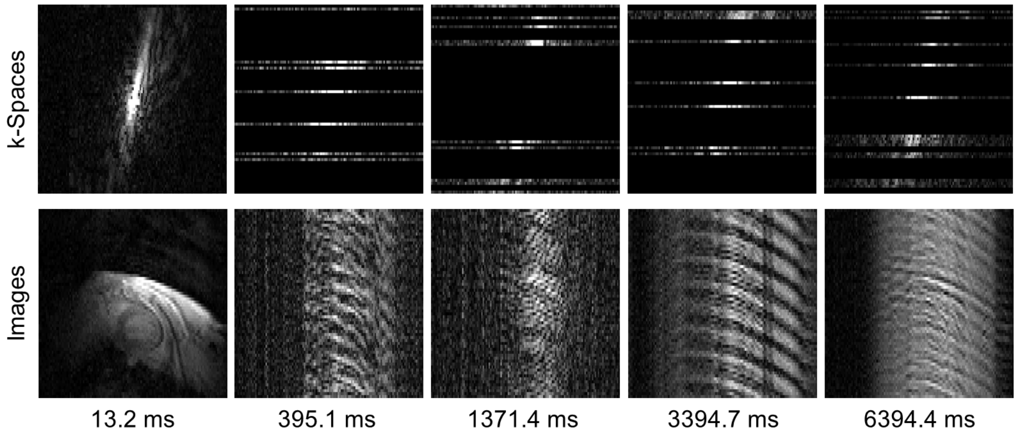

**Figure 7.2:** Undersampled k-spaces (top) and images (bottom) corresponding to different inversion time bins of 20 ms obtained in the GL acquisition of a Cartesian FAIR-LL FLASH measurement with the mean inversion times indicated. Each of these images and k-spaces was individually windowed for a clear appearance.

This approach offers the following two major benefits:

1. The ability to take into account any variations of $T_I$ that are caused i.e. by the long scan time associated with variable heart rates during the acquisition.
2. To provide a possibility to apply k-space undersampling for eventually reducing the total acquisition time.

The method was developed in cooperation with Dr. Thomas Troalen and Dr. Frank Kober at the *Centre de Résonance Magnétique Biologique et Médicale (CRMBM), Faculté de Médecine, Aix-Marseille Université, Marseille, France.*

Some of the material in this chapter has been published in [95]. The permission to reuse images and text from this publication was granted by the *International Society for Magnetic Resonance in Medicine.* Reused images are marked in the image caption.

## 7.2 Implementation of ASL-MAP

A FAIR-LL FLASH dataset consists of two LL datasets, acquired after a SS and a GL inversion. Each of these LL datasets consists of $n_{\mathrm{TI}}$ (inversion times) × $n_p$ (phase encoding steps) × $n_r$ (readout points) can be processed separately. Using a time log, each of the phase encoding steps is assigned to a temporal bin (size: 20 ms), resulting in a set of $n_{\#\mathrm{bins}}$ undersampled k-spaces with inversion times corresponding to the mean over the $T_I$ within the individual bins. The undersampling factor of each of the bins depends on the $T_I$ variation during the entire acquisition, which is in turn dependent on the heart rate of the animal.

These $n_{\#\mathrm{bins}}$ k-spaces were used as initial estimates $\widehat{K}_0(x,t)$ for the first iteration of the MAP algorithm. As only one receiver coil was used for all acquisitions, no coil combination had to be included in the reconstruction. The changes in each step of the reconstruction scheme described in section 3.2 will be pointed out in the following. Again, the pixel index $x$ will be omitted for reasons of clarity:

1. As before, the current consistent model k-spaces $\widehat{K}(t)$ were Fourier transformed to obtain consistent model images $\widehat{M}(t)$.
2. Before the pixel-wise fit, a real-valued relaxation curve in each voxel was calculated by taking the real part of the complex-valued magnetization $\widehat{M}(t)$ after a rotation to the real axis (Eq. 2.23 with $I \to \widehat{M}$):

   $$\widehat{M}_{\mathrm{Real}}(t) = \mathrm{Real}\left\{\widehat{M}(t) \cdot \exp(-i\varphi)\right\} \ . \tag{7.1}$$

   As the phase is changing at the zero-crossing of an inversion recovery experiment, the phase map $\varphi$ was calculated as an average over the phase of the last 80 % of the $n_{\mathrm{TI}}$ conventionally reconstructed images, that is after the inversion pulse. A pixel-wise model fit of Eq. 2.8 for an IR-LL FLASH relaxation process was applied to obtain model images $M(t)$.
3. The model images $M(t)$ were transformed back to the complex plane by a multiplication with the phase $\exp(i\varphi)$ and Fourier transformed to obtain model k-spaces $K(t)$.
4. As before, the data consistency was ensured by substituting the measured data for the model data separately for all undersampled k-spaces resulting in consistent model k-spaces $\widehat{K}(t)$.

## 7.3 Methods

The experiments were conducted according to a protocol approved by the animal experimentation committee of the *University of Marseille*, and conformed with European guidelines for the care and use of laboratory animals.

All imaging experiments were performed at the *CRMBM, Marseille, France* on a Bruker Biospin 4.7T imager (Ettlingen, Germany). The animals were positioned prone on an actively decoupled surface coil (Rapid Biomedical, Würzburg, Germany).

All post-processing was performed on a standard desktop PC equipped with an Intel Core i7-2600 CPU (3.4 GHz) using MATLAB (The MathWorks, Natick, MA) and an IDL environment (RSI, Boulder, CO).

To validate the proposed method, a conventional FAIR-LL FLASH experiment was performed with a healthy C57Bl6J mouse. As described in [54], every repetition started with an ECG- and respiratory-gated IR pulse, followed by the acquisition of $n_{\mathrm{TI}} = 55$ ECG-gated gradient echoes. This was repeated for all $n_p = 64$ phase encoding steps ($n_r = 128$) with an additional repetition delay of 3 s for relaxation between successive IR pulses. Post-processing was performed in three different ways:

- **A**: The complete dataset including all 55 acquired images of the relaxation process was used for a conventional reconstruction of the SS and the GL measurement.
- **B**: First, the same reconstruction as in A was performed. Next, all images visibly affected by respiratory motion were excluded for the evaluation of the perfusion.
- **C**: The phase encoding steps were assigned to bins of 20 ms, and the MAP algorithm was applied to the $n_{\#\mathrm{bins}}$ resulting undersampled k-spaces for both the SS and the GL measurement (5 examplary k-spaces and the corresponding images for the GL case are given in Fig. 7.2). The result is a set of $n_{\#\mathrm{bins}}$ model images or, equivalently, a set of parameters $M_0$, $M_0^*$ and $T_1^*$ for every pixel for both acquisitions. These parameters were used with the $T_I$ mean values of the conventional reconstruction (dotted lines in Fig. 7.1) to calculate a series of 55 model images, which was subsequently used for post-processing.

After the image reconstruction, perfusion maps were calculated separately for A-C as described in [54].

## 7.4 Results

The binning resulted in a set of $n_{\#\mathrm{bins}} = 357$ undersampled k-spaces for both the GL and the SS inversion that were passed on to the MAP reconstruction. Figure 7.3 shows 5 exemplary contrasts of the relaxation process after the GL (a) and the SS (b) inversion reconstructed by the conventional reconstruction (A) and using the MAP algorithm (C) with the mean inversion times of the conventional reconstruction indicated. In the conventional reconstruction, artifacts caused by respiratory motion are clearly visible (red arrows). These artifacts are considerably reduced by the model-based reconstruction.

A RoI analysis of the anterior myocardium is depicted in Figure 7.4. It shows relaxation curves of the SS (blue) and GL (purple) acquisition obtained by the three reconstruction methods as well as the $T_1$ values obtained by the three-parameter fit of Eq. 2.8. The

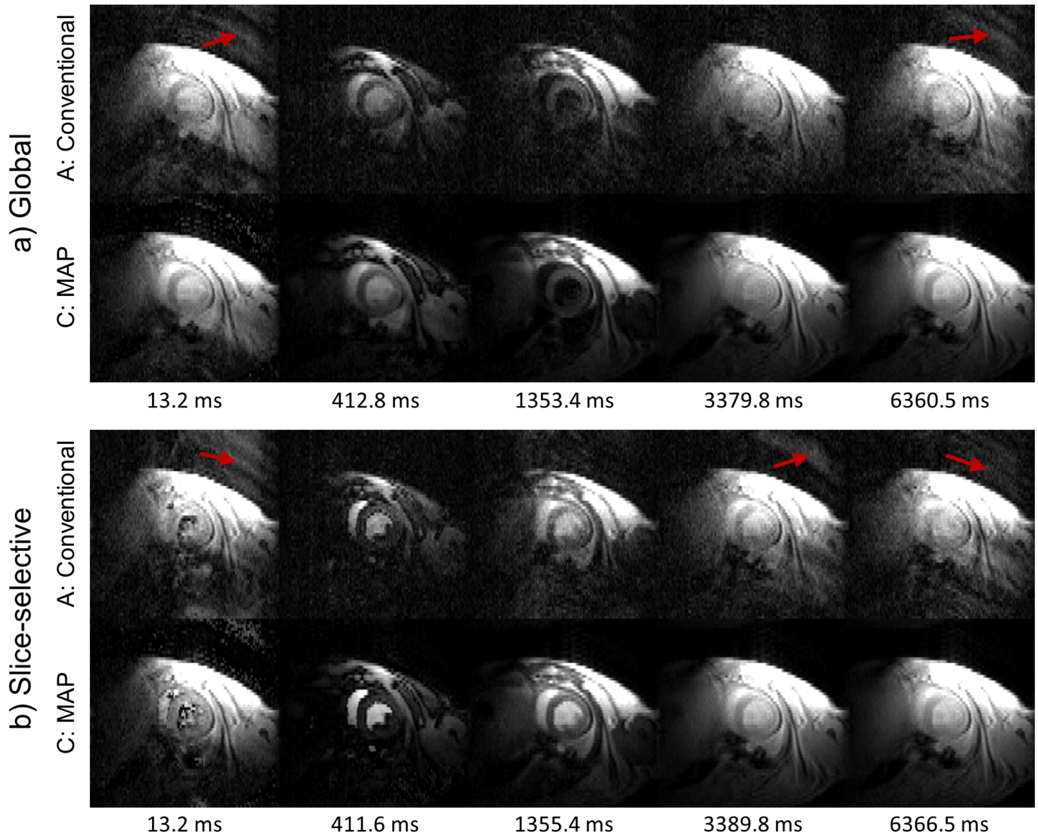

**Figure 7.3:** Exemplary contrasts of the relaxation process after global (a) and the slice-selective (b) inversion reconstructed by the conventional reconstruction (A) and the MAP algorithm (C) with the mean inversion times of the conventional reconstruction indicated. Respiratory artifacts are highlighted by the red arrows.

images in A which are affected by respiratory motion are indicated in orange. They were omitted in reconstruction B, leading to a different curve fits and relaxation times. C shows the images reconstructed using the model-based reconstruction, which is why the reconstructed images match the fitted curves.

Figure 7.5 shows the three perfusion maps obtained from the different post-processing techniques A-C. Although the perfusion values of A especially in the myocardium are higher than in the corresponding areas of the model-based reconstruction C, the perfusion map C more closely resembles the conventional reconstruction B without images affected by respiratory motion. This can be best observed in areas affected by respiratory motion such as the anterior and lateral myocardium.

This observation is confirmed by the perfusion values which are listed in Table 7.1. It includes perfusion values obtained from different myocardial regions (anterior and lateral) as well as the entire myocardium and the chest muscle. Again, good concordance was found between myocardial perfusion assessed after excluding images affected by

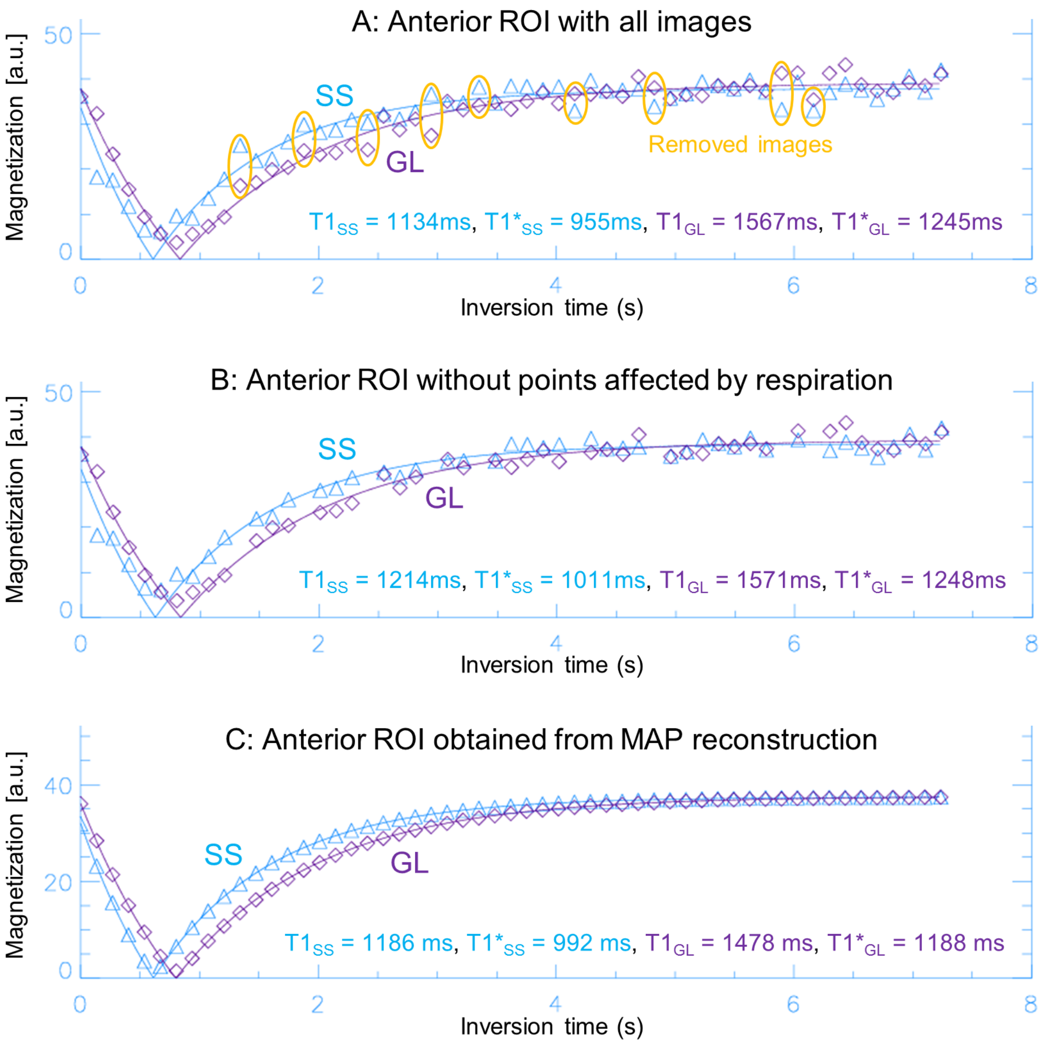

**Figure 7.4:** Relaxation curves in an anterior RoI obtained from the reconstruction methods A (all images), B (no images affected by respiratory motion) and C (MAP reconstructed images. The $T_1$ values obtained in the fit are listed in the bottom of the respective curves.

respiratory motion (B) and the model-based reconstruction (C).

## 7.5 Discussion

An extension of the MAP algorithm for a model-based reconstruction of FAIR-LL FLASH datasets is presented. In conjunction with a time log of all acquired PE steps, this allows taking into account any variations in $T_I$, which can be caused by variable heart rates or imperfect R-wave detection during the acquisition. Sorting the acquired data prior to the reconstruction leads to an excellent temporal resolution $< 20\,\text{ms}$ for the model-based

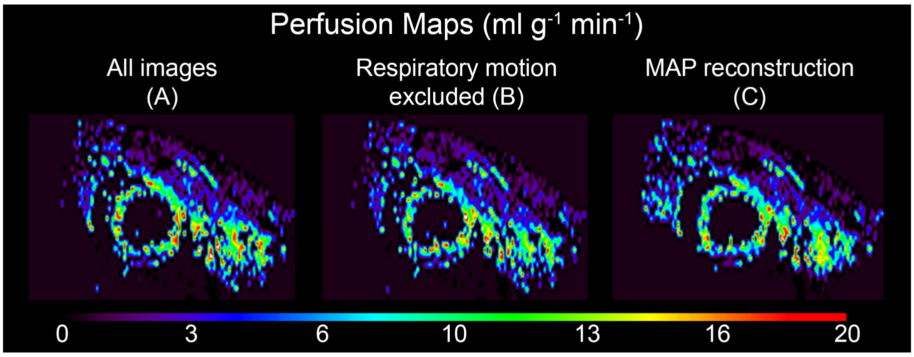

**Figure 7.5:** Perfusion maps. Figure from [95].

| Region | Conventional Reconstruction | | MAP (C) |
|---|---|---|---|
| | All images (A) | Respiration excluded (B) | |
| Anterior myocardium | $10.4 \pm 5.2$ | $8.6 \pm 5.5$ | $8.0 \pm 5.9$ |
| Lateral myocardium | $12.0 \pm 4.3$ | $7.4 \pm 5.5$ | $7.5 \pm 6.2$ |
| Global myocardium | $10.3 \pm 5.0$ | $8.1 \pm 5.8$ | $8.1 \pm 5.8$ |
| Chest muscle | $0.3 \pm 1.5$ | $0.3 \pm 1.5$ | $0.4 \pm 1.7$ |

**Table 7.1:** Perfusion values in ml $g^{-1}$ $min^{-1}$. Data are represented as mean ± standard deviation within the respective RoI. Table from [95].

fit. This represents a clear improvement in comparison with the average images over a wide range of inversion times, as it was done in the former implementation [54].

Previous attempts of minimizing respiratory artifacts for ASL studies in small animals included controlling the respiration using a mechanical ventilator [5,101–105], the use of velocity-compensated gradients, signal averaging, and higher levels of isoflurane [66,89] or the exclusion of images affected by respiratory motion [54] as it was performed as a reference in this study. While mechanical ventilation is technically very challenging in mice and cannot be routinely performed, the visual identification of images with respiratory artifact is typically performed manually, which is not feasible for larger studies. Additionally, the respiratory cycle usually varies over the course of an ASL experiment, leading to a distribution of motion artifacts over the entire relaxation curve. By enforcing a model of the relaxation process to the relaxation dataset, respiratory artifacts were successfully suppressed without any further changes in the setup of the measurement. Although the three perfusion maps seem visually similar, perfusion is overestimated if images affected by respiratory motion are not excluded from the $T_1$ fit (A vs. B). By using the constraint of a mono-exponential relaxation, the MAP algorithm automatically suppresses respiratory artifacts. To further minimize respiratory artifacts and to improve the accuracy of the fit, a time log of the respiratory motion of the animals could additionally be included in the post-processing, and phase encoding steps affected by respiratory motion could be removed before the model-based reconstruction.

Finally, the new technique holds the potential for a quantification of myocardial perfusion from further undersampled k-spaces, promising shorter scan times in the future. Although the initial k-spaces used in the model-based reconstruction were each undersampled with respect to a Nyquist sampled k-space for the desired FoV, the model-based reconstruction C was obtained from the same dataset as the fully sampled reconstructions A and B. The reduction of the data used for the undersampled k-spaces of C was limited by the SNR in our experiment. To enable a quantification of the perfusion from less data or, equivalently, reduce the acquisition time, data collection would have to be performed with multiple receiver channels or at higher field strengths to obtain a better SNR.

# 8 Consideration of Slice Profiles (CSP) in IR-LL $T_1$ Mapping

## 8.1 Introduction

As already mentioned in the theory chapter, numerous $T_1$ mapping techniques make use of the Look-Locker concept [59]. After a suitable magnetization preparation, excitation pulses are applied continuously to acquire a set of images along the relaxation curve (Fig. 8.2). After an inversion recovery magnetization preparation, the three-parameter model of Eq. 2.8 is typically used for describing the relaxation curve. The effect of the repeated application of RF pulses is respected by introducing an effective magnetization $M_0^*$ as well as an effective longitudinal relaxation parameter $T_1^*$. After fitting, these parameters can be used to derive the true longitudinal relaxation parameter $T_1$ using Eq. 2.9.

The accuracy of the $T_1$ obtained in these measurements is highly dependent on experimental conditions. Systematic errors can for example be caused by the transmit coil's $B_1$ inhomogeneity [19] or inaccurate preparation pulses [52]. A further source of error is the quality of the pulse profile used for slice selection. Especially for fast imaging sequences, short excitation pulses are frequently used, leading to a blurred slice profile as well as a broad distribution of flip angles in the direction of the slice selection. The latter problem has been addressed for $T_1$ mapping using 2D inversion recovery steady-state free precession sequences [17]. In [83], a local flip angle correction for $T_1$ mapping using 3D IR-LL FLASH sequences has been presented. This 3D specific technique assumes one single flip angle in each voxel determined by the position of the voxel along the slice direction without taking into account the shape of the RF excitation pulses.

In contrast to the previous chapters, which describe various implementations and applications of the MAP algorithm, this chapter introduces a new way of modeling the relaxation process in a 2D IR-LL FLASH measurement, taking into account the flip angle distribution caused by finite slice excitation pulses. This model will be called **C**onsideration of **S**lice **P**rofiles (CSP) relaxation model in the following.

A majority of the content of this chapter has been published in [97]. The permission to reuse images and text from this publication was granted by *Elsevier*. Reused images are marked in the image caption.

## 8.2 The CSP Model

As described in section 2.9, the RF pulses that are usually applied for slice selection lead to a $z$-dependent distribution of different flip angles $\alpha(z)$. It can be derived using a Fourier transform of the excitation pulse $A(t)$ according to Eq. 2.18.

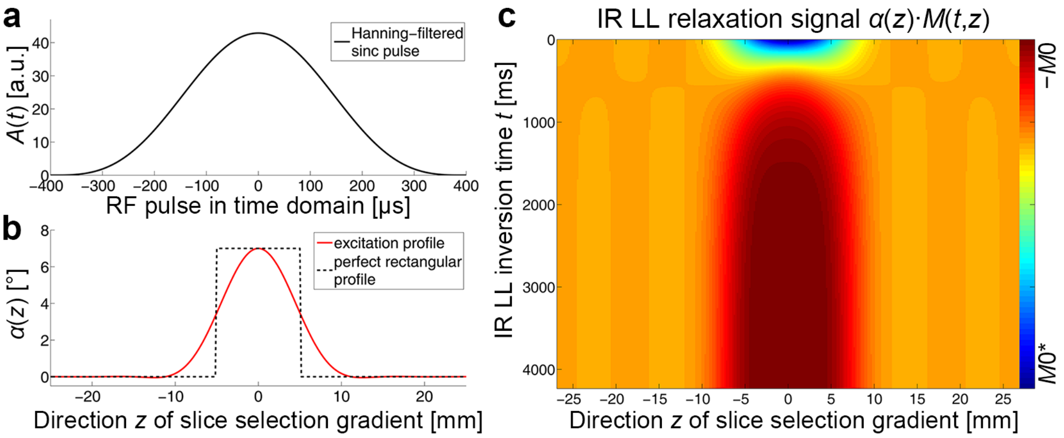

**Figure 8.1:** a: Hanning-filtered sinc pulse of 800 $\mu$s duration in the time domain. b: Corresponding excitation profile obtained by a Fourier transform (red line) and the desired perfect rectangular profile for a nominal flip angle of $\alpha_0 = 7°$, a repetition time of $T_R = 4.24\,\text{ms}$ and slice thickness 10 mm (black dashed line). c: Corresponding IR-LL relaxation signal $M(t, z)$ for $T_1 = 800\,\text{ms}$ weighted with the excitation profile $\alpha(z)$. Figure from [97].

As an example, a Hanning-filtered sinc pulse according to Eq. 2.17 with a duration of 800 $\mu$s and a sampling rate of 0.1 $\mu$s (i.e. 8000 samples) and the corresponding flip angle distribution $\alpha(z)$ across the excited slice for a nominal flip angle of $\alpha_0 = 7°$ is depicted in Figure 8.1a-b. To derive an expression for an $\alpha_0$-dependent relaxation model, the distribution $\alpha(z)$ was included in the inversion recovery Look-Locker relaxation model described by Eq. 2.8. This leads to a $z$-dependent relaxation curve:

$$M(t, z) = M_0^* (\alpha(z)) - (M_0 + M_0^* (\alpha(z))) \cdot \exp\left(-t/T_1^* (\alpha(z))\right) . \tag{8.1}$$

To simulate the effect of an RF excitation of angle $\alpha$, these relaxation curves have to be weighted with $\sin(\alpha)$. The result is a $z$-dependent distribution $S(t, z)$ of relaxation curves over the excited slice:

$$S(t, z) \propto \sin(\alpha(z)) \cdot M(t, z) \approx \alpha(z) \cdot M(t, z) . \tag{8.2}$$

The last approximation only holds for small flip angles. Finally, the relaxation curve of the entire voxel can be calculated by an integral of these relaxation signals over the all locations $z$ within the excited slice:

$$M(t) \propto \int_{\text{slice}} S(t, z)\, dz \approx \int_{\text{slice}} \alpha(z) \cdot M(t, z)\, dz . \tag{8.3}$$

The relaxation curves described by this model include the slice profile of the excitation pulse in the IR-LL relaxation model. They will be called CSP relaxation curves henceforth. Figure 8.1c shows the relaxation distribution $S(t, z)$ for the exemplary Hanning-filtered sinc pulse.

## 8.3 Methods

All imaging experiments were carried out on a 3 T whole-body scanner (MAGNETOM Trio, Siemens AG Healthcare Sector, Erlangen, Germany) employing a 12 channel phased-array head coil for signal reception.

All post-processing was performed on a standard desktop PC equipped with an Intel Core i7-2600 CPU (3.4 GHz) using MATLAB (The MathWorks, Natick, MA).

For all simulations and measurements performed in this work, Hanning-filtered sinc pulses described by Eq. 2.17 with $-1 < t < 1$ were used for excitation. The Hanning filter ensures a smooth excitation profile with a relatively broad, flat top [19].

To simulate a highly resolved flip angle distribution, a pulse with 8000 sample points was created according to Eq. 2.17 and zero-filled to a size of $2 \cdot 10^5$. As described in the theory section 2.9, the resulting excitation pulse $A(t)$ was Fourier transformed (Eq. 2.18) and the real part of the resulting distribution $\widetilde{p}(\omega)$ was reparametrized and rescaled to obtain $\alpha(z)$. This distribution was inserted in Eqs. 8.1, 8.2 and 8.3 to obtain CSP relaxation curves.

A dictionary-based fitting approach as described in section 2.10 was used to find the CSP relaxation curve best describing a measured signal. The atoms of the dictionary were precalculated for various sets of underlying parameters ($T_1$, $\alpha_0$, $T_R$). It included 1000 different $T_1$ values between 5 ms and 5000 ms. In-plane variations of the flip angle were taken into account by including flip angles in the interval $[3°, 4°, \ldots, 16°]$. $T_R$ is known very precisely and a variation was not considered in the dictionary. The equilibrium magnetization $M_0$ represents a scaling factor in Eq. 8.3 that will be obtained by the fitting process. The model curves were thus calculated using $M_0 = 1$. First, the Hanning-filtered sinc pulse given by Eq. 2.17 was used with a nominal flip angle $\alpha_0$ to calculate a flip angle distribution $\alpha(z)$ as described in section 2.9. Next, $\alpha(z)$ and the nominal relaxation time $T_1$ were used in conjunction with Eqs. 2.5 and 2.6 to calculate $T_1^*$ and $M_0^*$ distributions for the initial parameter set $[T_1, \alpha_0]$. These were in turn used in Eqs. 8.1 and 8.2 to obtain a signal distribution across the excited slice. Finally, an integration as in Eq. 8.3 delivered the CSP prototype belonging to the initial parameter set $[T_1, \alpha_0]$. Additionally, a constant was added as prototype for pixels not following an exponential relaxation. The resulting dictionary was used in conjunction with an OMP algorithm [78] to find the CSP curve best describing the measured signal and thus the corresponding parameter set $[T_1, \alpha_0]$.

### 8.3.1 Numerical Simulations

To investigate the accuracy of the conventional three-parameter relaxation model, a set of CSP relaxation curves for 80 $T_1$ values between 50 ms and 4000 ms for different combinations of $T_R = [4.24\,\text{ms}, 7.00\,\text{ms}]$ and $\alpha_0 = [6°, 12°]$ was calculated. The thermal equilibrium magnetization was set to $M_0 = 1$. The maximum inversion time was set to 15 s to make sure that the relaxation curve always covered the saturation magnetization $M_0^*$. A conventional mono-exponential fit was applied to these CSP curves and the results were compared to the initial relaxation parameters $T_1$ for every set of parameters $[T_1, T_R, \alpha_0]$. As a fit of the CSP model to the simulated curves leads to exactly the initial $T_1$ values, these results are not shown.

Additionally, the influence of the temporal coverage of the relaxation signal (which will be called maximum inversion time $\text{TI}_{\text{max}}$ in the following) on the mono-exponential fit was simulated for different parameter sets $[T_1, \alpha_0]$ using different values of $\text{TI}_{\text{max}}$ between 1 s and 6 s.

### 8.3.2 Phantom Experiments

A validation study was performed with a phantom consisting of 7 vials with different concentrations of CA (Resovist®, Bayer Schering Pharma, Berlin, Germany) and copper sulphate ($CuSO_4$) using an IR-LL FLASH sequence (FoV: $250{\times}250{\times}10\,\text{mm}^3$, $T_E$: 1.9 ms, $T_R$: [4.24 ms, 7.00 ms], $\alpha_0$: [6°, 12°]) with a non-selective, adiabatic IR pulse and a Golden Ratio [108] radial k-space trajectory (1000 projections, 128 readouts points). A Hanning-filtered sinc pulse according to Eq. 2.17 was used for slice excitation. To obtain a Nyquist sampled k-space for every inversion time, the measurement was segmented into 202 consecutive IR magnetization preparations, each of them with a different order of projections. A schematic illustration of the segmentation is given in Figure 8.2. Each of these acquisitions was followed by a delay of 30 s to allow for a complete relaxation, leading to a total scan time of ~ 2 h varying slightly with $T_R$. Reordering the acquired projections according to their inversion time resulted in 1000 Nyquist sampled k-spaces each consisting of 202 projections - the Nyquist limit for a radial k-space with 128 readout points per projection. Each of these images describing the contrast at different inversion times of the relaxation process was separately gridded using self-calibrating GROG (see section 2.2). After a Fourier transform, the images of the individual coils were combined using the SoS. To take into account the sign change of the relaxation curve after inversion, the sign of the individual coil entries was respected in that process (see section 2.11).

The dictionary look-up CSP evaluation described above was used in a pixel by pixel fashion to obtain a $T_1$ map from the acquired segmented IR-LL relaxation process. For comparison to the conventional signal model as described by Eq. 2.8, an mono-**EXP**onential three-parameter fit (EXP) was additionally applied.

As in the numerical simulations, the dependence of both fitting methods on the coverage of the relaxation process used for the fit was examined. For this purpose, the $\text{TI}_{\text{max}}$ value

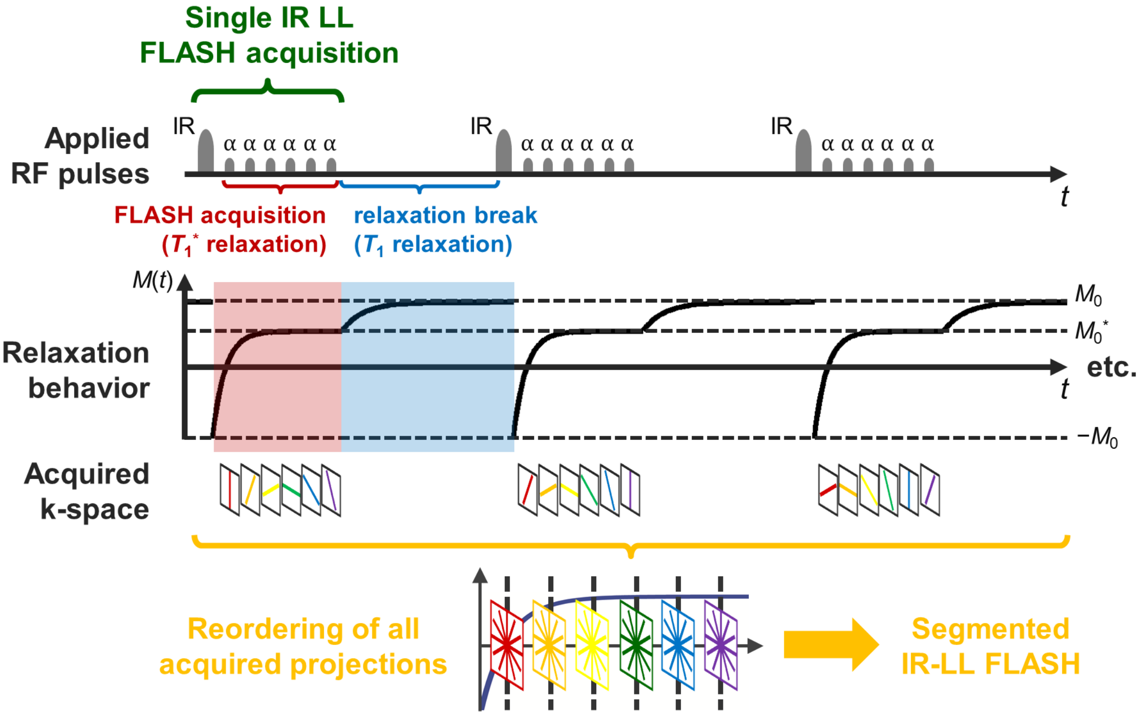

**Figure 8.2:** Schematic illustration of an IR-LL FLASH acquisition. After the application of an inversion pulse, multiple RF pulses are applied to monitor the relaxation behavior ($T_1^*$ relaxation indicated in red). In a segmented acquisition, this acquisition period is followed by a relaxation break ($T_1$ relaxation indicated in blue) before the next IR-LL FLASH acquisition is carried out. By segmenting the k-space to be acquired into multiple IR-LL FLASH acquisitions, a well-resolved time-series of the $T_1^*$ relaxation process can be obtained in every voxel. Figure from [97].

of the reference IR-LL FLASH dataset was artificially reduced to sampling times of 2 s, 3 s and 4 s before the application of the CSP or the mono-exponential fit.

Ground truth $T_1$ values were obtained using a segmented inversion recovery sequence as described in section 2.4. Here, only one RF pulse was applied after each non-selective IR pulse and a delay of 30 s was added prior to the next inversion to ensure a complete relaxation. This was repeated for incremented projection angles and inversion times such that a Nyquist sampled image was obtained for 13 different contrasts corresponding to inversion times between 2 ms and 8000 ms. A fit of Eq. 2.2 delivered a ground truth $T_1$ map that was used to evaluate the accuracy of the CSP as well as the mono-exponential fit.

### 8.3.3 In Vivo Measurements

All human in vivo studies were approved by our local ethics committee. They were performed on 7 healthy volunteers aged between 21 and 26 years, and written informed consents were obtained from the subjects prior to scanning. Measurements of the human brain were carried out with the same IR-LL FLASH sequence as in the phantom experiments (FoV: $250\times250\times8\,\mathrm{mm}^3$, $T_E$: 1.9 ms, $T_R$: 4.24 ms, $\alpha_0$: 12°, projections: 1000, readout points: 128). For time efficiency, the number of segments was reduced to 101 corresponding to a two-fold undersampling of the resulting segmented datasets, and the delay between two consecutive segments was reduced to 15 s, leading to a total scan time of ~ 0.5 h. The same post-processing as in the phantom experiments was used to obtain $T_1$ with both the conventional and the new method.

To examine the dependency of the accuracy of the CSP model and the EXP model on the inversion time TI, the **N**ormalized **R**oot-**M**ean-**S**quare **E**rror (NRMSE)

$$\mathrm{NRMSE}(t) = \sqrt{\frac{\sum_{x=1}^{N}\left[|S_{\mathrm{measured}}(x,t)| - |S_{\mathrm{model}}(x,t)|\right]^2}{\sum_{x=1}^{N}|S_{\mathrm{measured}}(x,t)|^2}} \tag{8.4}$$

of the model images $S_{\mathrm{model}}$ (obtained using CSP and EXP) with respect to the measured images $S_{\mathrm{measured}}$ (simply gridded without any fitting) was calculated. $N$ represents the number of image pixels.

Again, the dependence of CSP as well as EXP fitting on the coverage of the relaxation process used for the fit was examined. As in the phantom study, the $\mathrm{TI}_{\mathrm{max}}$ values of the reference IR-LL FLASH dataset were artificially reduced to sampling times of 2 s, 3 s and 4 s before the application of the CSP or the mono-exponential fit. With the resulting $T_1$ maps, a RoI analysis was performed in WM, GM and CSF regions of all 7 volunteers.

## 8.4 Results

### 8.4.1 Numerical Simulations

Figure 8.3 shows the results of the numerical simulations. A comparison of the simulated CSP relaxation curves (green dashed lines) and the fitted mono-exponential relaxation curves (red dash-dot lines) for $T_1 = [200\,\mathrm{ms}, 1000\,\mathrm{ms}, 2500\,\mathrm{ms}]$ is shown in Figures 8.3a-b. For a better illustration of deviations between the two models, Figures 8.3c-d depict the differences between the CSP curve and the corresponding mono-exponential fit for the same $T_1$ values. For very short inversion times, the EXP model noticeably overestimates the CSP curves (see negative differences). For rising inversion times, the mono-exponential model alternately over- and underestimates the simulated CSP curves. As the signal approaches the saturation value, the fit underestimates the CSP signal for all combinations of $[T_1, T_R, \alpha_0]$. This behavior becomes more prominent, the shorter $T_R$ and the larger $T_1$ as well as $\alpha_0$.

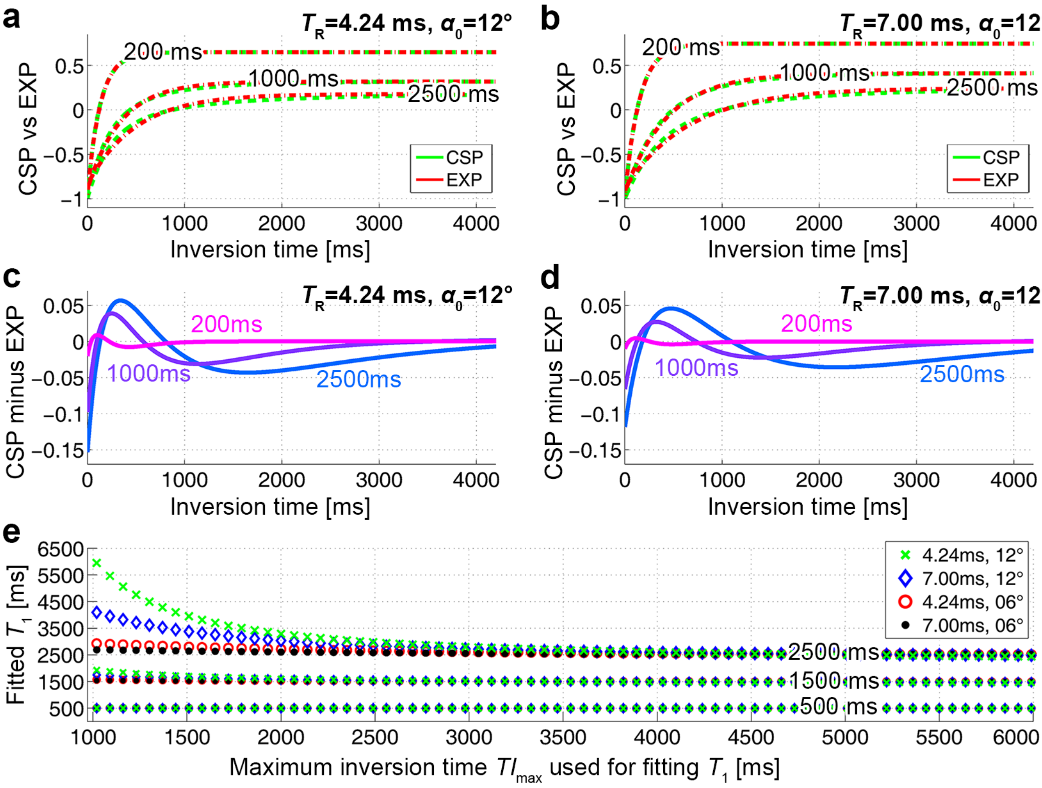

**Figure 8.3:** Numerical simulations. a-b: Simulated CSP relaxation curves (green dashed lines) and the curves obtained from a mono-exponential fit (red dash-dot lines) for different combinations of relaxation time $T_1$, repetition time $T_R$ and flip angle $\alpha_0$. c-d: Differences between the CSP and the EXP curves shown in Figures 8.3a-b. e: Influence of the maximum inversion time $\mathrm{TI}_{\mathrm{max}}$ on the accuracy of the EXP fit for different parameter sets and $T_1$ values of 500 ms, 1500 ms and 2500 ms. Figure from [97].

Figure 8.3e demonstrates the influence of the coverage of the relaxation process on the results of the EXP fit for exemplary $T_1$ values of 500 ms, 1500 ms and 2500 ms (vertical axis). It can be clearly seen that the accuracy of the mono-exponential fit strongly depends on $\mathrm{TI}_{\mathrm{max}}$ (horizontal axis). While there is a good agreement of all fitted values for the shortest $T_1$ of 500 ms, there is a systematic overestimation of $T_1$ by the mono-exponential fit increasing with the absolute value of $T_1$. For the highest $T_1$ value of 2500 ms, these deviations already start for $\mathrm{TI}_{\mathrm{max}}$ values of about 4 s. All observations made in Figures 8.3a-d regarding the influence of the flip angle and the repetition time on the systematic deviations of the EXP model are confirmed by Figure 8.3e. Again, the overestimation of the fitted $T_1$ values increases with larger $\alpha_0$ while it decreases with longer $T_R$.

### 8.4.2 Phantom Experiments

A mono-exponential fit of 100 pixels using standard MATLAB (The MathWorks, Natick, MA) routines took 3 s, the implemented CSP dictionary look-up for 100 pixels lasted 2.3 minutes on one single core of a standard desktop PC equipped with an Intel Core i7-2600 CPU (3.4 GHz).

Results of the phantom experiments are shown in Figures 8.4 and 8.5. Figures 8.4a-b depict exemplary voxels of the relaxation process in 3 different vials (black solid lines) as well as model curves obtained from both the CSP (green dashed lines) and EXP approach (red dash-dot lines). The associated vials are indicated in Figure 8.5b. Figures 8.4c-d show differences between the measured relaxation curve and the CSP (green) as well as the EXP (red) model curves for vial C and parameter combinations corresponding to Figures 8.4a-b.

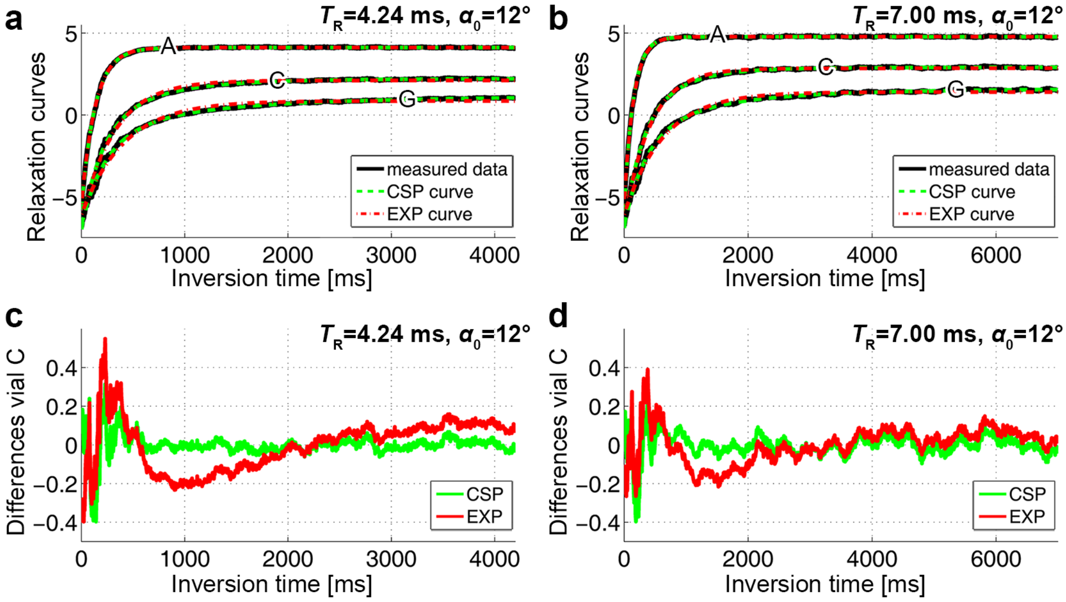

**Figure 8.4:** Phantom experiments. a-b: Measured relaxation curves (black solid lines), CSP model curves (green dashed lines) and EXP model curves (red dash-dot lines) for exemplary voxels and different sets of parameters $[T_R, \alpha_0]$. c-d: Differences between measured relaxation curve and CSP (green) as well as mono-exponential (red) curve for vial C. The parameter combinations correspond to Figures 8.4a-b. Figure from [97].

In all cases, the CSP relaxation curves represent an accurate model for the measured relaxation curves. On the contrary, the similar shapes of the curves in Figures 8.4c-d and Figures 8.3c-d confirm the systematic errors introduced by the EXP model which were already observed in the simulations. Again, an extension of $T_R$ reduces the deviations (see Fig. 8.3d). These differences are significantly lower for the CSP model.

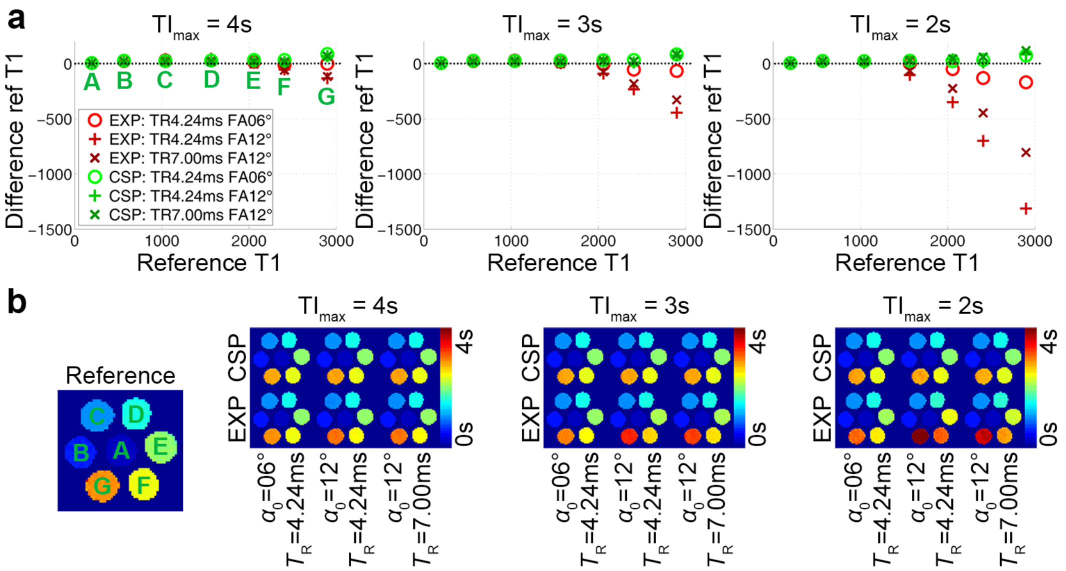

**Figure 8.5:** Phantom experiments. Influence of the maximum inversion time $\mathrm{TI}_{\mathrm{max}}$ on both fitting methods. From left to right, $\mathrm{TI}_{\mathrm{max}}$ values of 4 s, 3 s and 2 s are shown. a: Difference between the $T_1$ values obtained from the ground truth segmented IR experiment and the $T_1$ values obtained from the CSP (green) as well as the EXP fit (red) for different parameter sets. b: Reference $T_1$ map and $T_1$ maps obtained by the CSP (top) as well as the EXP fit (bottom) for values of $\mathrm{TI}_{\mathrm{max}}$ decreasing from left to right. Figure from [97].

Figure 8.5 shows the influence of the maximum inversion time $\mathrm{TI}_{\mathrm{max}}$ covered by the acquired data on both fitting methods. From left to right, sampling times $\mathrm{TI}_{\mathrm{max}}$ of 4 s, 3 s and 2 s were used for the fit. In the top row, Figure 8.5a depicts the difference between the reference $T_1$ values obtained in the ground truth experiment and the CSP fit (green) as well as the mono-exponential fit (red) for different combinations of $[T_R, \alpha_0]$. Each point represents the mean over a RoI in the vials indicated in green in Figure 8.5b. For relatively short $T_1$ values, both models are in good agreement with the reference regardless of $\mathrm{TI}_{\mathrm{max}}$. As $T_1$ increases, a systematic deviation can be observed for the mono-exponentially fitted values, strongly increasing with the reduction of $\mathrm{TI}_{\mathrm{max}}$. As predicted by the simulations, the error increases with the flip angle $\alpha_0$ and decreases with the repetition time $T_R$. For a parameter set of $T_R = 4.24\,\mathrm{ms}$, $\alpha_0 = 12°$, $\mathrm{TI}_{\mathrm{max}} = 2\,\mathrm{s}$ and a $T_1$ of about 3000 ms, the difference in $T_1$ reaches values of more than 1000 ms. On the contrary, despite a slight overestimation of $T_1$ for high relaxation times of about 3000 ms, the CSP model delivers accurate $T_1$ values for all ranges of $T_1$. More importantly, the $T_1$ results of the CSP model, in contrast to the EXP model, are virtually independent of the $\mathrm{TI}_{\mathrm{max}}$ value used for the fit.

Figure 8.5b shows the corresponding $T_1$ maps obtained from the ground true reference as well as the CSP (top) and the EXP fit (bottom). Again, $\mathrm{TI}_{\mathrm{max}}$ values of 4 s, 3 s and 2 s were used from left to right. The maps confirm the observation that the CSP model results in accurate $T_1$ values independent of the total sampling time while the accuracy of the values obtained from the EXP fit is strongly influenced by $\mathrm{TI}_{\mathrm{max}}$ (especially visible in the red vials of the $T_1$ maps).

### 8.4.3 In Vivo Measurements

Figure 8.6a shows the measured relaxation curves for two representative voxels (indicated in Fig. 8.6e) of the brain of volunteer V2 (black solid lines) as well as the corresponding model curves obtained from both the conventional mono-exponential fit (red dash-dot lines) and the dictionary-based CSP approach (green dashed lines). As in the numerical simulations and the phantom experiments, there is an overestimation of the mono-exponential model for very short inversion times and an underestimation of the saturation magnetization for long inversion times. For a better visualization of these systematic errors, differences between the measured curve and the CSP (green) as well as the EXP model (red) are shown for the same two exemplary voxels A (Fig. 8.6b) and B (Fig. 8.6c). Although differences occur for both models, they remain significantly smaller for the CSP model. Again, a higher absolute value of $T_1$ leads to higher deviations (see Fig. 8.6c). Additionally, the deviations between the measured image spaces and the CSP (top) and the EXP model (bottom) are depicted in Figure 8.6d for exemplary inversion times as indicated in blue in Figure 8.6a. A notable difference is present in both models especially for the shortest inversion times. These deviations decrease with longer inversion times. However, it remains considerably lower for the CSP model than for the mono-exponential model over the entire time course.

Again, the influence of $\mathrm{TI}_{\mathrm{max}}$ on the accuracy of the $T_1$ fit was investigated. Figure 8.6e shows the results of the CSP (top row) and the EXP fit (bottom row) for $\mathrm{TI}_{\mathrm{max}}$ values of 2 s, 3 s and 4 s. For a better visualization of the differences, a three-fold difference between the longest temporal coverage (4 s) and the two others is depicted additionally to the $T_1$ maps. While the $T_1$ maps of the CSP fit remain unchanged for all values of $\mathrm{TI}_{\mathrm{max}}$, the results of the EXP fit especially in regions of high $T_1$ values such as the CSF are highly dependent on $\mathrm{TI}_{\mathrm{max}}$.

The investigation of the NRMSE is shown in Figure 8.7. While Figure 8.7a shows the temporal evolution of the NRMSE between the measured images and the EXP model image (solid lines) and the CSP model image (dotted lines) for 3 exemplary volunteers, Figure 8.7b shows the mean over all volunteers V1-V7. All temporal courses show systematic deviations similar to the observations made in the simulations and the phantom experiments. However, as the NRMSE is positively defined (compare Eq. 8.4), no negative deviations can occur and the previously observed curves are reflected to the positive part of the vertical axis. Although there are deviations for both models, they remain significantly lower for the CSP model, which is demonstrated by a maximum value of 0.28 for the NRMSE of the EXP model compared to 0.12 for the CSP model.

The values of the in vivo RoI analysis are listed in Tables 8.1-8.3 for different tissue types. While the $T_1$ values obtained by the EXP model are strongly dependent on the temporal coverage $\mathrm{TI}_{\mathrm{max}}$, they are nearly independent of $\mathrm{TI}_{\mathrm{max}}$ if the CSP model is used for the

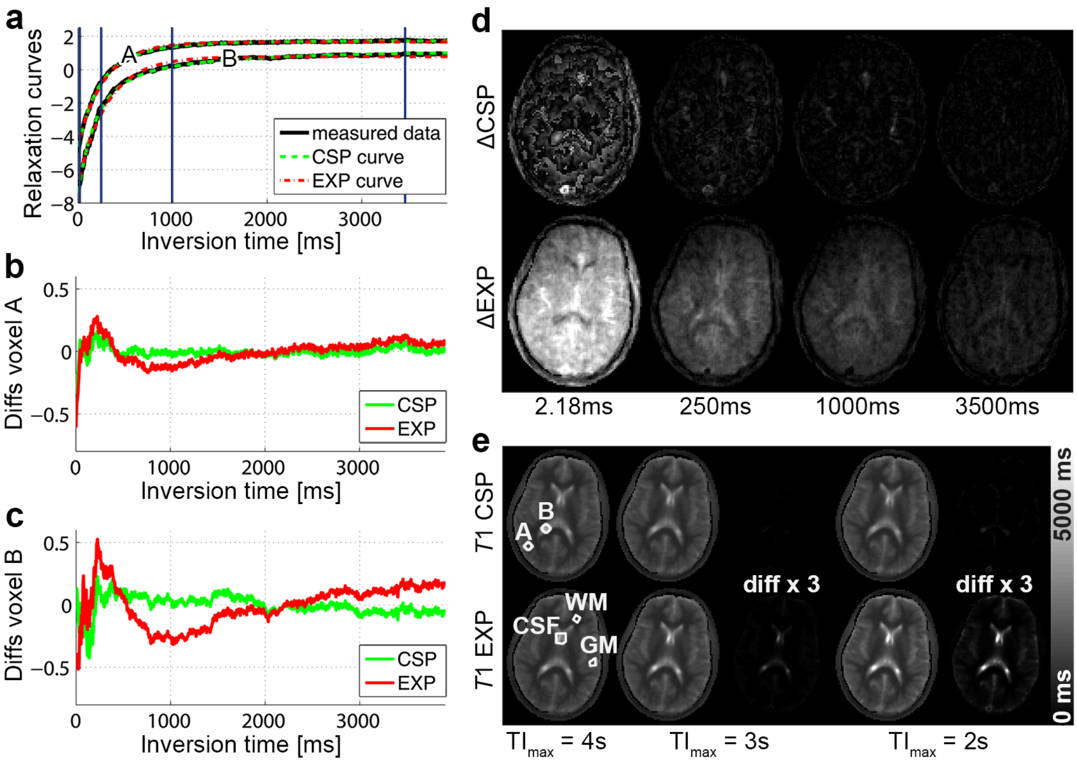

**Figure 8.6:** In vivo measurement of volunteer V2 with $T_R = 4.24\,\text{ms}$ and $\alpha_0 = 12°$. a: Measured (black solid lines) and model (green dashed and red dash-dot lines) relaxation curves at the voxels indicated in Figure 8.6e. b-c: Difference between measured relaxation curves and CSP (green) as well as EXP model (red) for voxel A (a) and B (b). d: Differences between measured and model image spaces at the inversion times indicated in blue in Figure 8.6a. e: $T_1$ maps obtained from CSP (top) and EXP fit (bottom) for $\text{TI}_{\text{max}} = [2\,\text{s}, 3\,\text{s}, 4\,\text{s}]$ as well as three-fold differences between the best temporal coverage ($\text{TI}_{\text{max}} = 4\,\text{s}$) and the poorer coverages of 3 s and 2 s. Figure from [97].

fit. This is most clearly illustrated by the maximum percentage difference between the highest $\text{TI}_{\text{max}}$ of 4 s (that is the best temporal coverage) and the other $\text{TI}_{\text{max}}$ values of 2 s and 3 s. While it stays below 0.7 % ($\text{TI}_{\text{max}} = 3\,\text{s}$) and below 1.9 % ($\text{TI}_{\text{max}} = 2\,\text{s}$) using the CSP fit, it reaches values of 14.5 % ($\text{TI}_{\text{max}} = 3\,\text{s}$) and even 54.9 % ($\text{TI}_{\text{max}} = 2\,\text{s}$) in the CSF using the EXP model. Even though the differences are considerably smaller for tissues of smaller $T_1$, differences of about 9.6 % ($\text{TI}_{\text{max}} = 2\,\text{s}$) or 2.9 % ($\text{TI}_{\text{max}} = 3\,\text{s}$) still occur in the GM using the EXP fit compared to 1.8 % ($\text{TI}_{\text{max}} = 2\,\text{s}$) or 0.5 % ($\text{TI}_{\text{max}} = 3\,\text{s}$) for the CSP model. Even in the WM, a difference of 1.8 % occurs for the smallest coverage of $\text{TI}_{\text{max}} = 2\,\text{s}$ using the EXP fit, while it remains at 0.4 % using CSP.

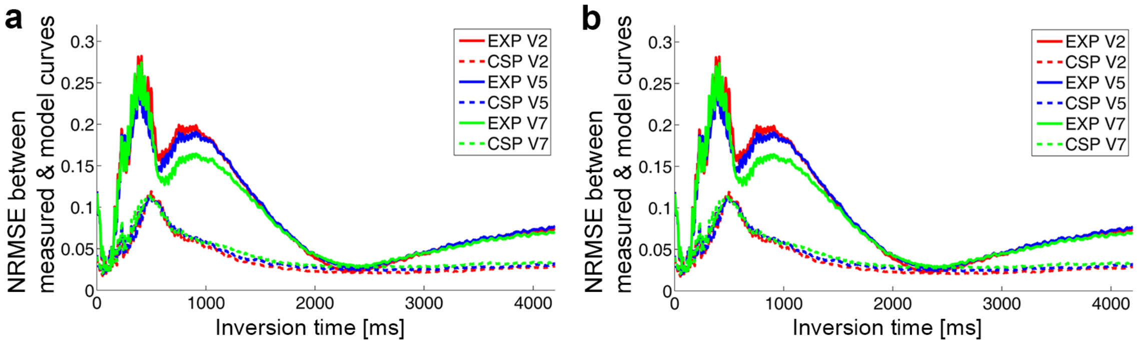

**Figure 8.7:** Temporal evolution of the NRMSE between the measured images and both models with the inversion time $T_I$ (EXP: Solid lines, CSP: Dotted lines). a: NRMSE of volunteers V2 (red), V5 (blue) and V7 (green). b: Mean NRMSE over all volunteers. Figure from [97].

| $\mathrm{TI}_{\mathrm{max}}$ | Model | | V1 | V2 | V3 | V4 | V5 | V6 | V7 |
|---|---|---|---|---|---|---|---|---|---|
| 4 s | EXP | $\mu \pm \sigma$ (ms) | 748 ± 9 | 781 ± 21 | 781 ± 10 | 716 ± 13 | 732 ± 23 | 703 ± 9 | 703 ± 8 |
| | CSP | $\mu \pm \sigma$ (ms) | 759 ± 8 | 794 ± 21 | 791 ± 10 | 724 ± 13 | 743 ± 24 | 713 ± 9 | 713 ± 8 |
| 3 s | EXP | $\mu \pm \sigma$ (ms) | 751 ± 8 | 785 ± 21 | 784 ± 10 | 718 ± 13 | 735 ± 24 | 706 ± 9 | 705 ± 8 |
| | | diff (%) | 0.4 | 0.5 | 0.4 | 0.3 | 0.4 | 0.3 | 0.3 |
| | CSP | $\mu \pm \sigma$ (ms) | 759 ± 8 | 795 ± 22 | 792 ± 10 | 725 ± 14 | 743 ± 24 | 713 ± 9 | 713 ± 8 |
| | | diff (%) | 0 | 0.1 | 0.1 | 0.1 | 0 | 0.1 | 0 |
| 2 s | EXP | $\mu \pm \sigma$ (ms) | 758 ± 9 | 795 ± 23 | 793 ± 11 | 724 ± 13 | 742 ± 24 | 711 ± 10 | 710 ± 8 |
| | | diff (%) | 1.4 | 1.8 | 1.6 | 1.2 | 1.3 | 1.1 | 1.0 |
| | CSP | $\mu \pm \sigma$ (ms) | 761 ± 9 | 797 ± 23 | 795 ± 11 | 728 ± 14 | 744 ± 23 | 715 ± 10 | 713 ± 8 |
| | | diff (%) | 0.3 | 0.3 | 0.4 | 0.4 | 0.1 | 0.2 | 0.1 |

**Table 8.1:** In vivo study. Means ($\mu$) and standard deviations ($\sigma$) of $T_1$ in WM regions obtained with EXP and CSP fitting and different temporal coverages $\mathrm{TI}_{\mathrm{max}}$ are listed for all 7 volunteers. Additionally, the percentage difference to the best temporal coverage $\mathrm{TI}_{\mathrm{max}} = 4\,\mathrm{s}$ is listed for the shorter coverages of 3 s and 2 s. Table from [97].

## 8.5 Discussion

For certain combinations of $T_1$, $T_R$ and $\alpha_0$ or a poor temporal coverage of the relaxation process, the CSP model offers an essential extension of the mono-exponential model which is widely-used for describing the relaxation behavior of an IR-LL FLASH sequence. Application areas as well as limitations of the CSP model will be discussed in the following

| TI$_{\text{max}}$ | Model | | V1 | V2 | V3 | V4 | V5 | V6 | V7 |
|---|---|---|---|---|---|---|---|---|---|
| 4 s | EXP | $\mu \pm \sigma$<br>(ms) | 1415<br>± 77 | 1393<br>± 77 | 1411<br>± 60 | 1507<br>± 77 | 1508<br>± 129 | 1499<br>± 66 | 1475<br>± 49 |
| | CSP | $\mu \pm \sigma$<br>(ms) | 1438<br>± 76 | 1421<br>± 76 | 1437<br>± 60 | 1527<br>± 73 | 1527<br>± 125 | 1516<br>± 64 | 1494<br>± 46 |
| 3 s | EXP | $\mu \pm \sigma$<br>(ms) | 1444<br>± 80 | 1427<br>± 84 | 1452<br>± 66 | 1546<br>± 82 | 1547<br>± 138 | 1539<br>± 71 | 1508<br>± 51 |
| | | diff (%) | 2.1 | 2.4 | 2.9 | 2.6 | 2.6 | 2.6 | 2.2 |
| | CSP | $\mu \pm \sigma$<br>(ms) | 1435<br>± 74 | 1423<br>± 77 | 1445<br>± 61 | 1528<br>± 74 | 1527<br>± 125 | 1523<br>± 65 | 1495<br>± 47 |
| | | diff (%) | 0.2 | 0.1 | 0.5 | 0 | 0 | 0.4 | 0.1 |
| 2 s | EXP | $\mu \pm \sigma$<br>(ms) | 1514<br>± 95 | 1512<br>± 101 | 1546<br>± 79 | 1642<br>± 101 | 1640<br>± 163 | 1641<br>± 85 | 1602<br>± 63 |
| | | diff (%) | 7.1 | 8.6 | 9.6 | 8.9 | 8.7 | 9.5 | 8.6 |
| | CSP | $\mu \pm \sigma$<br>(ms) | 1437<br>± 77 | 1430<br>± 78 | 1460<br>± 64 | 1540<br>± 85 | 1531<br>± 127 | 1543<br>± 64 | 1513<br>± 54 |
| | | diff (%) | 0.1 | 0.6 | 1.6 | 0.8 | 0.3 | 1.8 | 1.3 |

**Table 8.2:** In vivo study. Means ($\mu$) and standard deviations ($\sigma$) of $T_1$ in GM regions obtained with EXP and CSP fitting and different temporal coverages TI$_{\text{max}}$ are listed for all 7 volunteers. Additionally, the percentage difference to the best temporal coverage TI$_{\text{max}} = 4$ s is listed for the shorter coverages of 3 s and 2 s. Table from [97].

section.

### 8.5.1 Limitations of the Mono-exponential Relaxation Model

Numerical simulations and phantom experiments show that the ability to adequately describe the relaxation process using the mono-exponential model largely depends on the choice of $T_R$ and $\alpha_0$ as well as on the $T_1$ value. If, especially for long $T_1$ relaxation times, $T_R$ becomes too short or $\alpha_0$ too large, there is an increasing deviation between the EXP model and the measured relaxation curve. It therefore seems advisable to optimize the parameter set $[\alpha_0, T_R]$ depending on the quality of the excitation pulse applied or alternatively use accurately defined slice profiles in cases where large $\alpha_0$ and short $T_R$ are inevitable.

Additionally, the accuracy of the conventional model depends on the relaxation parameter $T_1$. As $T_1$ increases, the difference to the actual relaxation curve grows. Despite clear deviations of the mono-exponential model from the actual relaxation curves, the error in the determination of $T_1$ stays acceptably low for most in vivo applications. However, in model-based reconstruction algorithms [8, 25, 90, 94], the underlying model is iteratively enforced to the acquired data and the systematic error of the conventional EXP model would therefore be enhanced within each iteration (see chapters 3, 5 and 4). In these cases where a very precise modeling of the course of the relaxation is of importance,

| $\mathrm{TI}_{\mathrm{max}}$ | Model | | V1 | V2 | V3 | V4 | V5 | V6 | V7 |
|---|---|---|---|---|---|---|---|---|---|
| 4 s | EXP | $\mu \pm \sigma$ (ms) | 3052 ± 884 | 2460 ± 547 | 2832 ± 624 | 2731 ± 574 | 2985 ± 626 | 2421 ± 459 | 2427 ± 371 |
| | CSP | $\mu \pm \sigma$ (ms) | 2826 ± 637 | 2397 ± 445 | 2687 ± 484 | 2613 ± 447 | 2807 ± 460 | 2373 ± 393 | 2380 ± 314 |
| 3 s | EXP | $\mu \pm \sigma$ (ms) | 3495 ± 1239 | 2706 ± 694 | 3182 ± 812 | 3064 ± 755 | 3402 ± 861 | 2659 ± 569 | 2652 ± 450 |
| | | diff (%) | 14.5 | 10.0 | 12.3 | 12.2 | 13.9 | 9.8 | 9.3 |
| | CSP | $\mu \pm \sigma$ (ms) | 2807 ± 635 | 2391 ± 435 | 2673 ± 471 | 2614 ± 443 | 2797 ± 456 | 2370 ± 389 | 2375 ± 303 |
| | | diff (%) | 0.7 | 0.2 | 0.5 | 0 | 0.4 | 0.1 | 0.2 |
| 2 s | EXP | $\mu \pm \sigma$ (ms) | 4726 ± 2490 | 3318 ± 1136 | 4103 ± 1454 | 3902 ± 1290 | 4527 ± 1677 | 3202 ± 833 | 3171 ± 653 |
| | | diff (%) | 54.9 | 34.9 | 44.9 | 42.9 | 51.6 | 32.3 | 30.7 |
| | CSP | $\mu \pm \sigma$ (ms) | 2772 ± 629 | 2386 ± 431 | 2654 ± 460 | 2608 ± 430 | 2784 ± 454 | 2358 ± 381 | 2360 ± 283 |
| | | diff (%) | 1.9 | 0.4 | 1.2 | 0.2 | 0.8 | 0.6 | 0.9 |

**Table 8.3:** In vivo study. Means ($\mu$) and standard deviations ($\sigma$) of $T_1$ in CSF regions obtained with EXP and CSP fitting and different temporal coverages $\mathrm{TI}_{\mathrm{max}}$ are listed for all 7 volunteers. Additionally, the percentage difference to the best temporal coverage $\mathrm{TI}_{\mathrm{max}} = 4\,\mathrm{s}$ is listed for the shorter coverages of 3 s and 2 s. Table from [97].

the proposed CSP model should be used instead of the conventional mono-exponential model.

Finally, the accuracy of the mono-exponential fit is strongly related to the temporal coverage of the relaxation process by the acquired signal that is used for the fit. Small $\mathrm{TI}_{\mathrm{max}}$ values lead to a strong weighting of the initial increase of the magnetization after the inversion pulse. In this case, insufficient information is available about the effective steady-state magnetization $M_0^*$ usually reached for longer inversion times. The very pronounced systematic deviations between the measured curve and the EXP model result in the observed overestimation of $T_1$. In contrast, the weighting of the exponential increase and the steady state magnetization $M_0^*$ for the typical $T_1$ range of human tissue is more balanced for larger $\mathrm{TI}_{\mathrm{max}}$ values. Despite obvious systematic errors, this leads to a better accuracy in the resulting $T_1$ values of the EXP model.

These deviations are significantly smaller for the CSP model, which was found to be largely independent of the signal coverage in all experiments performed. It therefore represents an improvement of the conventional mono-exponential fit in applications where only short sampling times are feasible.

### 8.5.2 Limitations of the CSP model

A straightforward but quite lengthy implementation of the CSP dictionary look-up was used in this work to demonstrate the functionality of the method. However, the duration of the look-up for an entire dataset can easily be shortened to a few seconds by starting with a broader spacing of the $T_1$ parameters used in the dictionary of the first look-up which is recursively reduced in multiple iterations.

In all experiments, the courses of the CSP curves were in very good agreement with the actual relaxation curves. They represent a simple extension of the mono-exponential model for modeling the IR-LL relaxation process and become essential especially if short $T_R$, large $\alpha_0$ or short $\mathrm{TI}_{\mathrm{max}}$ are used in the sequence design. The quality of the CSP model depends on the precision of the transmit coil's $B_1$ fields used for slice excitation defining the flip angle distribution $\alpha(z)$. $B_1$ inhomogeneities would result in spatial variations in the distribution, leading to differences between the expected and measured slice profile relaxation curves. Instead of re-examining the value of the nominal flip angle used in the sequence design and replacing it by a more accurate estimate as it was proposed in [19], a wide range of flip angles was used to create the CSP signal prototypes of the dictionary.

According to [19], a low inversion efficiency can introduce systematic errors in the $T_1$ evaluation using IR-LL FLASH sequences. Another source of error are off-center inversion pulses causing magnetization transfer effects leading to a reduced initial magnetization $-M_0$ and therefore errors in the calculation of $T_1$ using Eq. 2.9. Moreover, slice-selective inversion can lead to arterial spin labeling effects altering the relaxation behavior. To minimize these effects, non-selective, adiabatic inversion pulses were used for all experiments in this work. As the CSP relaxation model equally well described the relaxing signal of both the phantom as well as the in vivo experiments, it seems reasonable to assume that none of these effects were large enough to produce relevant changes in the relaxation behavior for the experiments in this chapter.

### 8.5.3 Limitations in the Assumption of a Mono-exponential Behavior in Every Voxel

Both the mono-exponential and the CSP model are based on the assumption of a single relaxation time in every voxel. As already mentioned in section 4.5.9, this assumption is no longer valid for voxels containing multiple tissues of different relaxation parameters [90, 94]. To correct for these errors in the proposed CSP model, relaxation models with multiple exponentials would have to be considered in the dictionary used for the fit. However, for most clinical situations with a sufficiently high spatial resolution, homogeneous tissue can be assumed in every voxel. As an example, spatial resolutions of up to 1 mm×1 mm×2 mm were previously achieved using segmented IR-LL techniques [19,67,82]. An evaluation of multiple relaxation times in one pixel goes beyond the scope of this work.

### 8.5.4 Comparison of the Obtained $T_1$ Values to Standard Literature

Although there is a wide range of literature WM and GM values, the $T_1$ values of GM obtained in this study (ranging from 1393 ms to 1527 ms) for relaxation curves of a good temporal coverage of the relaxation ($\mathrm{TI}_{\mathrm{max}} = 4\,\mathrm{s}$) are in agreement to many literature values [30, 65, 110] with a range from 1331 ms to 1470 ms. In contrary, $T_1$ values obtained from an EXP fit with the poorest temporal coverage of $\mathrm{TI}_{\mathrm{max}} = 2\,\mathrm{s}$ are ranging from 1512 ms to 1642 ms - a systematic error which is not in agreement with literature. Although the values of WM (ranging from 703 ms to 794 ms for both models with $\mathrm{TI}_{\mathrm{max}} = 4\,\mathrm{s}$) are smaller than many literature values for overall WM such as 832 ms in [106], they are in agreement with the value of 761 ms found in [110] for frontal WM. For these values, the coverage-dependent differences were relatively small (<1.8 %). Due to the large standard deviation within the RoIs of the CSF, these values were not compared to other literature.

### 8.5.5 Application Areas of the New Model

In most parameter mapping applications, a trade-off between spatial and temporal resolution has to be made for image reconstruction to obtain a set of images of the relaxation process. Subsequently, a pixel by pixel fit is applied to these images to obtain a $T_1$ and $M_0$ map. Despite relatively large inaccuracies in the course of the relaxation process, the conventional mono-exponential fit generally results in a sufficient accuracy of the longitudinal relaxation parameter $T_1$. If only one fit is performed, discrepancies between model and measured data do not lead to any consequential errors and the model can be used without major concerns if the previously described limitations regarding the parameters $T_R$, $\alpha_0$ and $\mathrm{TI}_{\mathrm{max}}$ are taken into account in the sequence design.

In contrast, any inaccuracies in the relaxation model can be of great importance in iterative model-based reconstruction techniques for parameter mapping such as the MAP technique presented in this thesis. These methods try to obtain parameter maps out of highly undersampled datasets by maximizing the consistency between the measured data and the applied model iteratively. Therefore, even small model violations can accumulate to considerable errors in the reconstruction. An artifact-free reconstruction is achievable only if a very accurate model is available [90]. The maximum possible reduction factor critically depends on the accuracy of the utilized model [25].

The influence of imperfect slice profiles was already addressed in the MAP implementations in chapters 5 and 6 by using a dictionary-based fitting approach. In this manner, the flip angle distribution was approximated by a linear combination of multiple relaxation curves to the relaxation data (see section 5.5.3). Although this was accurate enough for the MAP algorithm to converge, including the CSP model into the previously described implementations of MAP promises a way of further minimizing systematic model violations and improve the results of the MAP algorithm in future applications.

# 9 MAP for AIF Determination in Myocardial Perfusion MRI

## 9.1 Introduction

As described in section 2.14, myocardial first-pass DCE-MRI enables the visual assessment of myocardial perfusion from a series of $T_1$-weighted images. For a quantitative evaluation of myocardial blood flow using the linear approximation $\Delta(C) \propto T_S R_1 C$ between the change in signal intensity due to the CA injection and the CA concentration itself (Eq. 2.31), the condition $T_S R_1 C \ll 1$ must be fulfilled, and unsaturated AIF and TECs must be available (section 2.15).

As described in section 2.15, conventional methods for quantitative myocardial perfusion measurements try to separately acquire an unsaturated but low-SNR as well as a saturated but high-SNR time series for determination of an unsaturated AIF and a TEC of good SNR. Instead, a radial SR-LL FLASH acquisition can be combined with a KWIC filter (see section 2.2) for estimating $T_1$ and thus gadolinium concentration from one high dose injection [48]. Although a $T_S$ of ~ 50 ms can be reached using this technique, these saturation times can still be considerably too long for the condition $T_S R_1 C \ll 1$ to hold, especially for short $T_1$. Thus, even shorter $T_S$ would be desirable to further improve the estimation of the unsaturated AIF. Additionally, each of the KWIC-reconstructed images consists of multiple radial projections acquired at different saturation times $T_S$. Despite the application of a weighting function, their average contrast and equally the effective saturation time $T_{S,\text{eff}}$ of the resulting image is only a rough approximation of the real contrast about 50 ms after the SR pulse.

To overcome these problems, the SR-MAP algorithm (see chapter 4) is applied in this chapter for the determination of an unsaturated AIF. As described in section 2.14, myocardial perfusion imaging is usually performed separately for each heartbeat starting with an SR preparation pulse, followed by a fast imaging sequence which is limited to a temporal window of ~ 200 ms in diastole. To enable a MAP-reconstruction, a radial SR-LL FLASH sequence is applied for data collection. Next, the SR-MAP algorithm is used to reconstruct one image for each projection, with the smallest $T_{S,1}$ corresponding to the acquisition time of the first projection acquired after the SR pulse. For such short $T_S$ (typically only several milliseconds), the requirement of $T_S R_1 C \ll 1$ is very well fulfilled. By repeating this procedure for 40 consecutive heartbeats after the administration of the CA bolus, an image series of the earliest contrast $T_{S,1}$ enables the estimation of an unsaturated AIF. To verify the quality of this approach for AIF determination and thus the quantification of the MBF, the presented method was compared to a dual-bolus quantification in a volunteer study.

This part of the project was assisted by the master's candidate David Lohr. His tasks involved the segmentation of the reconstructed image series and the subsequent quantitative evaluation of the myocardial perfusion.

## 9.2 Implementation of SR-MAP

A radial dataset obtained in the single-preparation SR-LL FLASH acquisition of one single heartbeat is used as input for this implementation of MAP. As described in section 5.2, the "nearly empty" k-spaces obtained by gridding the single projections into separate k-spaces were "filled" by a linear interpolation of all acquired k-space points through time. In that process, the intensity directly after preparation was assumed to be zero ($M(t_0) = 0$) due to the saturation pulse that was used for magnetization preparation. These improved k-space estimates were used for initialization of the algorithm.

Compared to the implementation described in chapter 5.2, the following changes were made:

1. As before, the current consistent model k-spaces $\widehat{K}_\xi(x,t)$ of all individual coils were Fourier transformed to obtain consistent model images $\widehat{M}_\xi(x,t)$.
2. The signals received in the different coils $\xi$ were combined using a sign-dependent SoS as described in section 5.2. Although an SR pulse is applied for magnetization preparation, the sign of the relaxation curve was respected in that process to consider remaining longitudinal magnetization caused by imperfect saturation. As only a small number of projections (well below the Nyquist limit) is available in radial first-pass perfusion measurements, the precalculation of a phase map $\varphi_\xi(x)$ prior to the reconstruction was impossible. Instead, a new phase map $\varphi_\xi(x)$ was determined before the coil combination of each iteration using the median of the phase in the temporal dimension ($\angle(\circ)$ denotes the complex phase of $\circ$):

$$\varphi_\xi(x) = \begin{cases} \text{median}_t\left\{\angle\left(\widehat{M}_\xi(x,t)\right)\right\} \\ \qquad\qquad \text{if } -\pi/2 < \text{median}_t\left\{\angle\left(\widehat{M}_\xi(x,t)\right)\right\} < \pi/2, \\ \text{median}_t\left\{\bmod\left[\angle\left(\widehat{M}_\xi(x,t)\right)+2\pi,\ 2\pi\right]\right\} \\ \qquad\qquad \text{otherwise.} \end{cases} \tag{9.1}$$

All phase angles lie in the interval $-\pi < \varphi < \pi$. While it is sufficient to directly take the median for angles $-\pi/2 < \varphi < \pi/2$, the phase jump between $-\pi$ and $\pi$ has to be respected by adding an increment of $2\pi$ and subsequently performing a modulo operation of $2\pi$ to shift all phases to the interval $0 < \varphi < 2\pi$ before the median is calculated. This phase map was used for coil combination with Eqs. 5.1

and Eq. 5.2 to obtain $\widehat{M}_{\text{combined}}(x,t)$. Next, a dictionary-fit was used to obtain a combined model $M_{\text{combined}}(x,t)$ of all coils.

3. The re-separation into single-coil model images $M_\xi(x,t)$ was performed as before and the result was Fourier transformed to obtain single-coil model k-spaces $K_\xi(x,t)$.
4. As before, the data consistency was ensured by substituting the measured data for the model data separately for all acquired projections and all coils. Due to the highly undersampled sampling pattern, no additional zeroing was performed (as e.g. in section 5.2).

The dictionary used for the SR-MAP reconstructions in this chapter was generated as follows: As the same RF pulses as in chapter 8 were used for slice-selective excitation, the CSP relaxation curves were generated as described in section 8.3 with Eq. 8.1 for IR-prepared sequences replaced by Eq. 2.11 for SR-prepared sequences. In that equation, the nominal flip angle $\alpha$ had to be replaced by the $z$-dependent distribution $\alpha(z)$ of flip angles before the integration along the $z$-direction (Eq. 8.3). Although an acquisition window of only ~ 200 ms and therefore a very poor temporal coverage of the relaxation curve leads to a growing inaccuracy in the determination of $T_1$ using MAP, the curves can nevertheless be sufficiently modeled by a set of $T_1$ with a growing distance for $T_1 \geq 200\,\text{ms}$ (see section 4.5.4). For that reason, a set of only 60 $T_1$ values corresponding to equally spaced relaxivities of $R_1 = [0.001, 0.002, \ldots, 0.060]\ \text{ms}^{-1}$ in combination with 5 different flip angles in the interval $[\alpha - 4°, \alpha - 2°, \alpha, \alpha + 2°, \alpha + 4°]$ was used for the calculation of the CSP relaxation curves. This dictionary of $60 \cdot 5 = 300$ elements was complemented by a constant as prototype for pixels not following an exponential relaxation. In the fitting step 2 of the algorithm, an orthogonal matching pursuit algorithm [78] was used in conjunction with this dictionary of 301 elements to obtain the relaxation curve best describing the relaxation behavior in each voxel of the consistent model images $\widehat{M}_{\text{combined}}(x,t)$.

## 9.3 Methods

All imaging experiments were carried out on a 3 T whole-body scanner (MAGNETOM Trio, Siemens AG Healthcare Sector, Erlangen, Germany) employing a 32 channel cardiac array for signal reception.

All post-processing was performed on a standard desktop PC equipped with an Intel Core i7-2600 CPU (3.4 GHz) using MATLAB (The MathWorks, Natick, MA).

All human in vivo studies were approved by our local ethics committee. They were performed on healthy volunteers, and written informed consents were obtained from the subjects prior to scanning.

Myocardial first-pass perfusion measurements were performed on 4 healthy volunteers (1 male, 3 female) aged between 20 and 24 years. For an assessment of the reproducibility, 2 of these volunteers were measured twice within a period of 1 month. A dual-bolus acquisition was used to validate the proposed AIF determination method against the prebolus gold standard. The acquisition scheme had the following features:

- Imaging of a single slice (FoV: $250 \times 250\,\text{mm}^2$-$270 \times 270\,\text{mm}^2$, slice thickness: 8 mm-10 mm) in a double oblique orientation corresponding to the short axis view of the heart.
- Entire acquisition in breath-hold to minimize respiratory motion.
- Intravenous injection of a gadolinium-based contrast agent (Gadovist®, Bayer Schering Pharma, Berlin, Germany) using a power injector Medrad MR Injector Spectris Solaris EP (Volkach, Germany). The CA bolus (prebolus: 1 ml at 3.6 ml/s, bolus: 4 ml at 4 ml/s) was followed by a saline flush (20 ml at 4 ml/s).
- Application of an ECG-gated radial single-slice SR-LL FLASH sequence ($T_R$: 3.49 ms-3.60 ms, $T_E$: 1.54 ms-1.59 ms, $\alpha$: 12°, projections: 60, readouts points: 128, Golden Ratio [108] sampling order) over 40 consecutive heartbeats.
- Limitation of the acquisition to a temporal window of ~ 200 ms to minimize cardiac motion. The repetition time $T_R$ was adjusted to enable the acquisition of a fixed number of 60 radial projections within this time period.
- Utilization of a trigger delay adjusted to the heart rate of the measured subject to ensure imaging in diastole and further minimize cardiac motion.

### 9.3.1 Determination of the Tissue Enhancement Curves

For a determination of the TECs, all 60 projections of each frame of the bolus acquisition were gridded into one separate k-space using self-calibrating GROG (see section 2.2). A Fourier transform resulted in a series of 40 images of the CA passage. As each radial projection equally contributes to the contrast, the image series had an average contrast $\overline{T_S}$ of all saturation times $T_{S,j}$ of the acquisition (see section 2.15). Although 202 projections are necessary to fulfill the Nyquist limit for a radial trajectory with 128 readout points per projection, the quality of the resulting images was expected to be sufficient for a TEC estimation due to the nature of the radial undersampling artifacts (see section 2.2).

Next, the correction steps 1-4 described in section 2.15 were applied to the image series as follows:

1. **Motion correction:** All frames of the image series were rigidly shifted along the two image axes until the structures of the individual slices matched as closely as possible.
2. **Segmentation:** 6 myocardial sectors were defined in the motion-corrected image series using the software package [68].
3. **Partial volume correction:** A partial volume correction as described in [56] was carried out.

4. **Baseline correction:** A baseline correction as described in [55] was applied.

These TECs were used for the entire post-processing.

### 9.3.2 Determination of Unsaturated Arterial Input Functions

Both the contrast agent concentration $C$ of the bolus acquisition and the average saturation time $\overline{T_S}$ of the average contrast images are too large for the condition $T_S R_1 C \ll 1$ to hold for the signal of the blood pool. Therefore, unsaturated AIFs were estimated in the following ways:

- **A**: The data of the prebolus acquisition were reconstructed in the same way as the for the TEC estimation using the bolus data. As this acquisition was performed with a lower dose of CA, the condition $T_S R_1 C \ll 1$ is assumed to be fulfilled and an unsaturated AIF can be determined from the resulting image series. The scaling factor $\mathrm{sf}_{\mathrm{prebolus}}$ between the bolus TECs and the prebolus AIF is given by the ratio of injected CA:

$$\mathrm{sf}_{\mathrm{prebolus}} = \frac{\text{injected CA bolus}}{\text{injected CA prebolus}} = \frac{4\,\mathrm{ml}}{1\,\mathrm{ml}} = 4\,. \tag{9.2}$$

  To rescale the prebolus AIF and match the CA concentration $C$ of the bolus acquisition, the prebolus AIF is plotted $\mathrm{sf}_{\mathrm{prebolus}} = 4$ times next to each other with a distance depending on the injection rate. The sum results in an $\mathrm{AIF}_A$ that can be used in conjunction with the bolus TEC for the quantification. This previously published approach for determining the AIF was used as reference [55].

- **B**: Each of the SR-LL FLASH datasets of the bolus acquisition was reconstructed separately using the SR-MAP sequence described in the previous section. The result was a set of 60 images with contrasts corresponding to the saturation times $T_{S,1}, \ldots, T_{S,60}$ of the acquired projections for each of the 40 frames. To fulfill condition $T_S R_1 C \ll 1$ as good as possible, the image series of the shortest saturation time $T_{S,1}$ was used to estimate an unsaturated AIF. The scaling factor $\mathrm{sf}_{\mathrm{MAP}}$ between the average contrast TECs and the $\mathrm{AIF}_j$ of contrast $T_{S,j}$ is given by the ratio of the saturation times:

$$\mathrm{sf}_{\mathrm{MAP},j} = \frac{\overline{T_S}}{T_{S,j}} = \frac{\left(\sum_{n=1}^{60} T_{S,n}\right)/60}{T_{S,j}}\,. \tag{9.3}$$

  To rescale the early contrast $\mathrm{AIF}_1$ and match the level of the average contrast TECs, $\mathrm{AIF}_1$ was multiplied by $\mathrm{sf}_{\mathrm{MAP},1}$. The result was an unsaturated $\mathrm{AIF}_B$ that can be used in conjunction with the bolus TEC for the quantification. This method was compared to the reference $\mathrm{AIF}_A$.

- **C**: As the rescaled $\mathrm{AIF}_A$ of the low dose prebolus acquisition and $\mathrm{AIF}_B$ of the early contrast obtained from the model-based reconstruction differently well fulfill condition $T_S R_1 C \ll 1$, a third AIF was determined from the model-based reconstruction with saturation effects similar to the prebolus reference A. For this purpose, one of the model-based contrasts $T_{S,j}$ of the bolus acquisition was chosen with a product $T_S \cdot C$ similar to the prebolus acquisition:

$$\overline{T_S} \cdot C_{\text{prebolus}} \overset{!}{=} T_{S,j} \cdot C_{\text{bolus}} \,. \tag{9.4}$$

As the contrast agent concentrations differed by $\text{sf}_{\text{prebolus}} = 4$, the contrasts had to have exactly the ratio between the average saturation time $\overline{T_S}$ and the $T_{S,j}$ being searched for. After choosing the contrast most closely resembling this ratio, rescaling was performed as described in B according to Eq. 9.3. The resulting $\text{AIF}_C$ was expected to have the same saturation effects as the prebolus $\text{AIF}_A$.

### 9.3.3 Comparison of the Perfusion Values

Finally, the MBF of all volunteers was determined as described in [47] using the TECs in conjunction with the different AIFs obtained using methods A-C.

## 9.4 Results

The reconstructed datasets of the 6 acquisitions were numbered from V1 to V6. Measurements V1 and V5 as well as V3 and V6 correspond to the repeatedly measured volunteers.

Figure 9.1 depicts 4 different frames (that is 4 different heartbeats) of the CA passage for volunteer V1. Shown are 4 of the 60 contrasts obtained in the MAP reconstruction as well as the conventional gridding reconstruction of the prebolus as well as the bolus acquisition before any correction was carried out. To underline the difference between the MAP contrasts, the intensity of all image series was left unchanged. As expected, the image intensity of the model-based reconstructions increases along the saturation time $T_{S,j}$. In the two conventional reconstructions, the higher CA dose of the bolus series manifests in a higher intensity of the ventricles in comparison to the low dose prebolus series.

### 9.4.1 Determination of the Tissue Enhancement Curves

The determination of the TECs of measurement V6 can be seen in Figure 9.2. After the rigid motion correction and segmentation, partial volume effects are clearly visible in the septal RoIs (blue and green). They are effectively corrected by the partial volume correction. Finally, a baseline correction is conducted to obtain the TECs which can be used for the quantification.

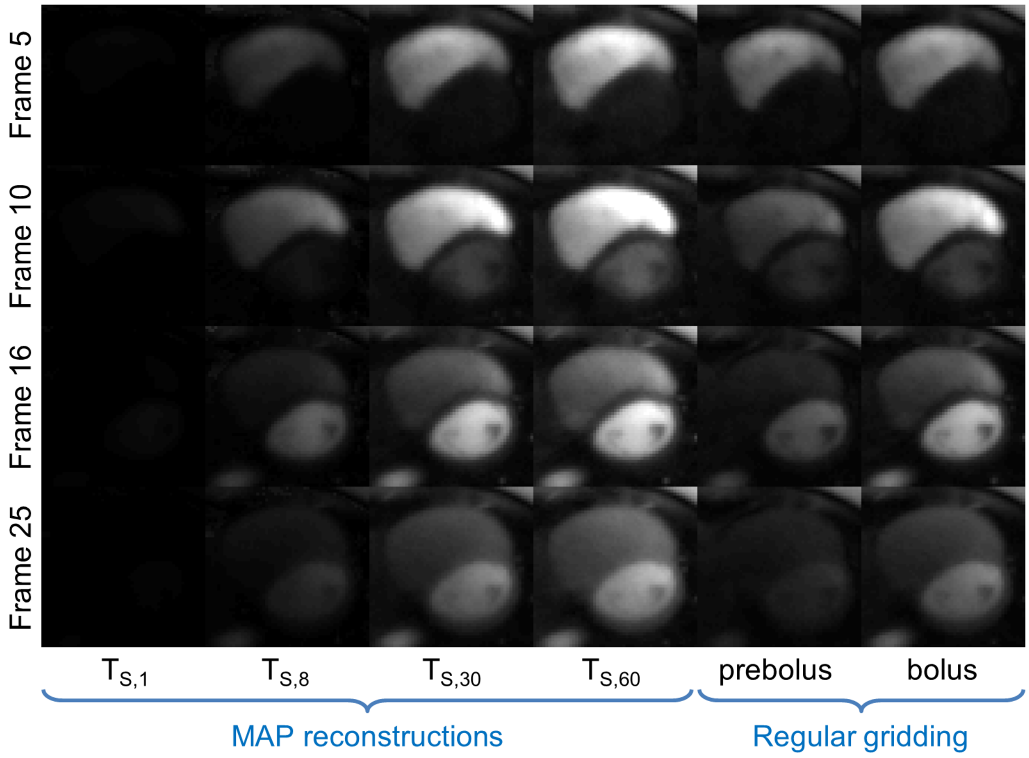

**Figure 9.1:** Reconstructed images of one volunteer. Shown are four exemplary contrasts obtained from the application of MAP to the SR-LL FLASH datasets of each heartbeat (left) as well as conventional gridding reconstructions of the prebolus and the bolus acquisition (right).

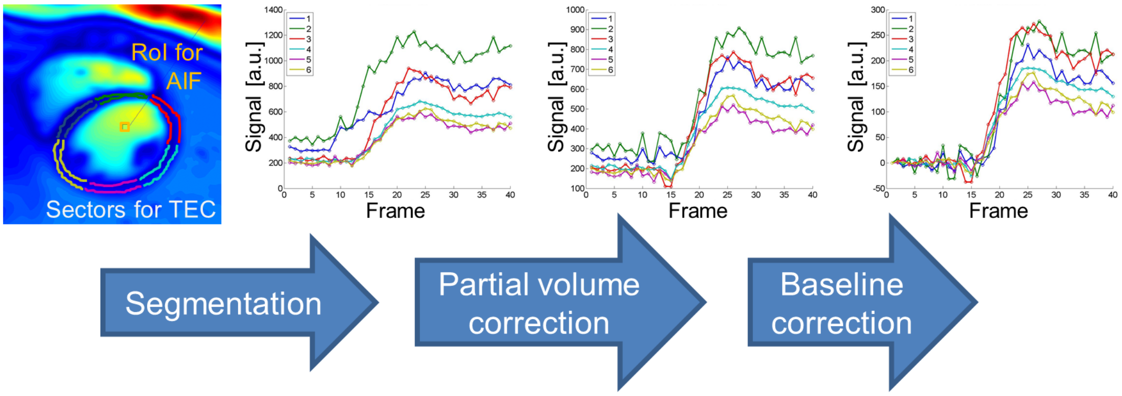

**Figure 9.2:** Determination of TECs in 6 myocardial sectors for dataset V6. After motion correction and segmentation, a partial volume correction and a baseline correction have to be performed to obtain TECs which can be used for the quantification.

### 9.4.2 Determination of Unsaturated Arterial Input Functions

Figure 9.3 depicts the methods that were used for AIF determination in this work for volunteer V1. While the prebolus blood curve has to be shift-scaled in method A (Fig. 9.3a), the model-based reconstructions of time frames $T_{S,1}$ (B) and $T_{S,j}$ (C) are rescaled using the ratios $\mathrm{sf}_{\mathrm{MAP},1}$ and $\mathrm{sf}_{\mathrm{MAP},j}$ of the saturation times (Fig. 9.3b).

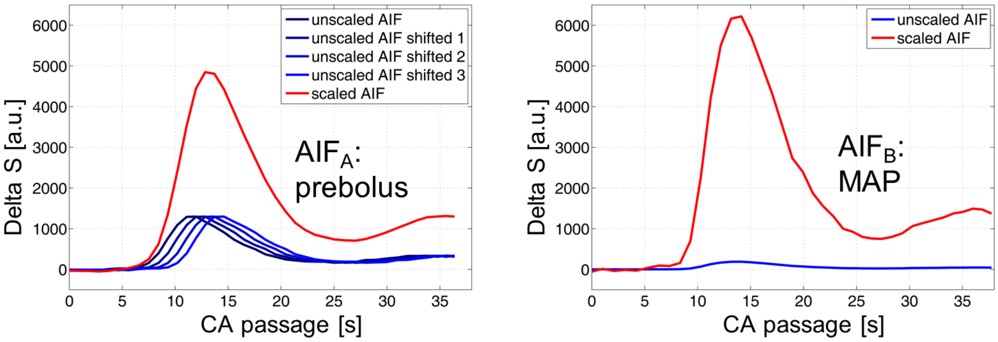

**Figure 9.3:** Determination of the AIF using methods A (by shifting the signal-time-curve of the prebolus acquisition) and B (by rescaling the signal-time-curve of the model-based reconstruction) for volunteer V1.

While the scaling of the AIF using methods A and B was performed using the signal curve of the prebolus (A) and the shortest saturation time $T_{S,1}$ of the model-based reconstruction (B), a saturation time had to be selected where the ratio of the saturation times match the contrast agent concentrations as accurately as possible (C). For all acquisitions, this was the case for saturation time $T_{S,8}$. All saturation times and the resulting scaling factors that were used for the AIF estimation are listed in Table 9.1.

| | V1 | V2 | V3 | V4 | V5 | V6 |
|---|---|---|---|---|---|---|
| $\overline{T_S}$ (ms) | 106.17 | 105.02 | 105.81 | 110.54 | 104.64 | 106.09 |
| $T_{S,1}$ (ms) | 3.22 | 2.94 | 2.85 | 3.16 | 2.85 | 3.13 |
| $\mathrm{sf}_{\mathrm{MAP},1}$ | 32.97 | 35.72 | 37.13 | 34.98 | 36.72 | 33.89 |
| $T_{S,8}$ (ms) | 27.65 | 27.56 | 27.70 | 27.41 | 28.94 | 27.18 |
| $\mathrm{sf}_{\mathrm{MAP},8}$ | 3.84 | 3.81 | 3.88 | 3.86 | 3.82 | 3.85 |

**Table 9.1:** Saturation times and scaling factors used for the AIF determination.

Figure 9.4 shows the saturated pseudo-AIF of the bolus acquisition (blue) as well as the AIFs determined using methods A-C for all volunteers (blue, red, black). For all volunteers, the saturation effects of the pseudo-AIF can be clearly recognized during the passage of the CA through the left ventricle. In the same time interval, the model-based curves $\mathrm{AIF}_B$ of the shortest saturation time ($T_{S,1}$) are least saturated and exceed all other curves. For all volunteers, these two curves frame the other AIFs of reconstruction methods A and C, which, as expected, have very similar signal intensities. Although these curves match very closely for volunteers V1, V3, V4 and V5, they still show a comparable signal intensity for volunteers V2 and V6 compared to AIF$_B$ (higher) and the saturated pseudo-AIF (lower). For all volunteers, the saturation effects of the prebolus reconstruction A are similar to or smaller than the model-based reconstruction C of comparable saturation.

The difference in the shape of reconstruction A compared to the curves of B and C can be attributed to the fact that they originate from two separate acquisitions (prebolus and bolus). For volunteers V4 and V6, a substantial change in the heart rate between these two acquisitions in conjunction with the same trigger delay led to missed ECG triggers in the bolus acquisition, which in turn resulted in a compressed signal-time-course of the bolus acquisitions compared to the prebolus curve.

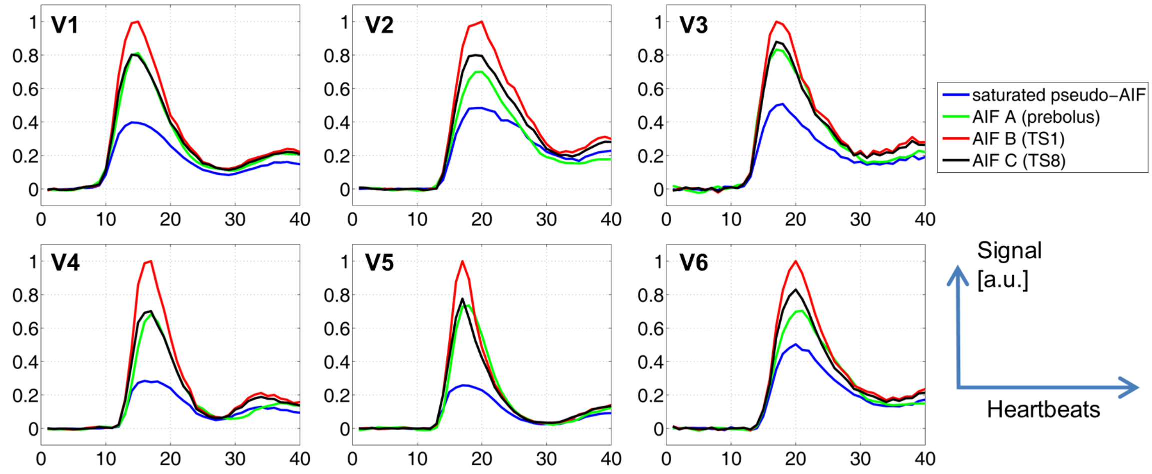

**Figure 9.4:** Arterial input functions obtained with methods A-C for all 6 volunteers. Blue: Saturated pseudo-AIF of the bolus acquisition. Green: Shift-scaled AIF$_A$ of the prebolus acquisition. Red: AIF$_B$ for $T_{S,1}$ obtained from the rescaled model-based reconstruction of the bolus acquisition. Black: AIF$_C$ for $T_{S,8}$ obtained from the rescaled model-based reconstruction of the bolus acquisition resembling the saturation effects of AIF$_A$.

### 9.4.3 Comparison of the Perfusion Values

The average perfusion values over all 6 sectors are listed in Table 9.2 for all volunteers. Additionally, the means ($\mu$), standard deviation ($\sigma$) and relative errors ($\sigma/\mu$) over all volunteers is given. While the difference in $\mu$ between the prebolus reference (A) and the comparable model-based time series of similar saturation (C) is only 5.3 %, the difference to the unsaturated model-based time series (B) is 21.3 %. As the relative error is about 10 % for all methods, this indicates a systematic deviation between the methods A and C with a more saturated AIF and method B with the least saturated AIF. A list of the perfusion values of all sectors in all volunteers is given in Table F.1 of the appendix.

| Method | V1 | V2 | V3 | V4 | V5 | V6 | $\mu \pm \sigma$ | $\sigma/\mu(\%)$ |
|---|---|---|---|---|---|---|---|---|
| A | 0.69 | 0.86 | 0.71 | 0.78 | 0.64 | 0.83 | **0.75 ± 0.09** | **11.3** |
| B | 0.56 | 0.61 | 0.67 | 0.54 | 0.52 | 0.62 | **0.59 ± 0.06** | **9.9** |
| C | 0.63 | 0.69 | 0.77 | 0.82 | 0.63 | 0.70 | **0.71 ± 0.08** | **10.7** |

**Table 9.2:** Average myocardial blood flow (ml/g/min) over all sectors for all volunteers as well as the means ($\mu$), standard deviations ($\sigma$) and relative errors ($\sigma/\mu$) over all volunteers.

## 9.5 Discussion

As the two saturation times $T_{S,8}$ and $\overline{T_S}$ are in the same ratio (1:4) as the CA concentrations $C$ of the prebolus and the bolus acquisition, the related AIFs were expected to have a comparable signal behavior for the passage of the CA through the left ventricle where saturation effects mainly occur. For all volunteers, this assumption is confirmed by $\text{AIF}_A$ and $\text{AIF}_C$. Although both of these curves show less saturation effects than the highly saturated pseudo-AIF of the bolus acquisition, a considerable level of saturation is still present in these acquisitions. This becomes apparent when looking at $\text{AIF}_B$ of the shortest possible saturation time $T_{S,1}$, which appreciably exceeds the saturated curves for all volunteers. The lower level of saturation can be explained by the fact that the condition $T_S R_1 C \ll 1$, which has to be fulfilled for the linear relation $\Delta(C) \propto T_S R_1 C$ to hold, is best satisfied in that case.

For the same TEC, a higher AIF results in lower MBF values. It was therefore expected that the perfusion values based on the deconvolution of the least saturated $\text{AIF}_B$ were lower than the perfusion values determined using $\text{AIF}_A$ and $\text{AIF}_C$. The percentage difference of 21.3 % between the perfusion values of the prebolus reference A and the model-based reconstruction B in combination with the fact that all methods have a similar relative error (about 10 %) underlines the assumption that there is an inherent saturation in the left ventricle even for the prebolus acquisition of a low CA dose. The order of magnitude of these effects is similar to the saturation at a $T_{S,8}$ of about 28 ms (percentage difference 5.3 % between perfusion values A and C), which leads to the conclusion that even the very short saturation times of ~ 50 ms that were achieved using the AIF determination techniques described in section 2.15 [33, 48] have a systematic error in the MBF quantification, which is caused by saturation effects.

The proposed MAP method enables saturation times of ~ 3 ms in myocardial first-pass perfusion imaging, which significantly improves the compliance to the condition $T_S R_1 C \ll 1$ for typical relaxivities $R_1$ and contrast agent concentrations $C$ and therefore enhances the quality of the linear approximation $\Delta(C) \propto T_S R_1 C$ (see section 2.15). This greatly reduces saturation effects compared to the current standard methods (dual bolus and two saturation time method, section 2.15). Additionally, only one acquisition has to be performed, which is advantageous compared to the two acquisitions needed in the dual bolus method, as two injections may reflect different physiological states (e.g. the variation of the heart rate between prebolus and bolus acquisition for volunteers V4 and

V6). Quantitative myocardial perfusion combined with a model-based reconstruction could therefore pave the way to a more accurate absolute quantification of myocardial blood flow in future applications.

# 10 Summary and Conclusions

In this work, a model-based acceleration of parameter mapping (MAP) for the determination of the tissue parameter $T_1$ using magnetic resonance imaging (MRI) is introduced. The iterative reconstruction uses prior knowledge about the relaxation behavior of the longitudinal magnetization after a suitable magnetization preparation to generate a series of fully sampled k-spaces from a strongly undersampled acquisition. A Fourier transform results in a spatially resolved time course of the longitudinal relaxation process, or equivalently, a spatially resolved map of the longitudinal relaxation time $T_1$.

In its fastest implementation, the MAP algorithm enables the reconstruction of a $T_1$ map from a radial gradient echo dataset acquired within only a few seconds after magnetization preparation, while the acquisition time of conventional $T_1$ mapping techniques typically lies in the range of a few minutes. After validation of the MAP algorithm for two different types of magnetization preparation (saturation recovery & inversion recovery), the developed algorithm was applied in different areas of preclinical and clinical MRI and possible advantages and disadvantages were evaluated.

The first version of the MAP algorithm was based on a saturation recovery prepared sequence, in which the longitudinal magnetization is brought to zero before data acquisition. While the magnetization subsequently relaxes back into equilibrium, several lines of k-space are collected with a gradient echo sequence. The continuous radio frequency (RF) excitation results in a shorter relaxation time $T_1^*$, which is dependent on the repetition time $T_R$ as well as the flip angle $\alpha$. This prevents a direct determination of $T_1$ without a separate measurement of the flip angle. The saturation preparation, however, has the great advantage that, as the magnetization is always brought to zero, no waiting times are necessary between consecutive measurements. This results in a potentially high temporal resolution in dynamic $T_1$ measurements. With the saturation-prepared implementation of the MAP algorithm (SR-MAP, chapter 4), all necessary data for the reconstruction of a $T_1^*$ map were acquired within 6.6 s after a single magnetization preparation. As part of a volunteer study, the $T_1^*$ values obtained using SR-MAP were compared to the results of a segmented measurement (scan time: 24 min). The differences were as low as 1.3 % in the white matter (WM), 2.4 % in the gray matter (GM) and 4.0 % in the cerebrospinal fluid (CSF). A perfect saturation was assumed in the reconstruction, on the one hand reducing the numerical complexity, but on the other hand potentially introducing errors in the iterative reconstruction if the measured signal is not perfectly saturated. In addition, only a single exponential course was assumed in each voxel, which can lead to errors in voxels consisting of several types of tissue, or where excitation is performed with multiple flip angles due to poor excitation profiles.

To enable a direct determination of the tissue parameter $T_1$, a MAP implementation for inversion-prepared gradient echo sequences was developed in chapter 5 (IR-MAP). Again, the continuous RF excitation leads to a shorter relaxation time $T_1^*$. In case of an initial inversion, however, $T_1$ can be determined using the additionally available information about the magnetization $-M_0$ directly after the inversion. To additionally consider the occurrence of voxels with multiple tissue types (partial volume) as well as the typically varying flip angle in slice selection direction (caused by imperfect slice profiles), the mono-exponential model was replaced by a linear combination of three exponential functions. $T_1$ maps of an axial slice of the brain were determined in 7 healthy volunteers using this IR-MAP algorithm. Again, the determined values (scan time: 6 s) were validated against a segmented $T_1$ mapping experiment (scan time: 30 min). The difference between the $T_1$ values for the two measurements was smaller than 5.1 %, both in GM as well as in WM. In addition, the determined $T_1$ values were in good agreement with standard literature values in GM (IR-MAP: 1395 ms-1455 ms, literature: 1331 ms-1470 ms) and WM (IR-MAP: 676 ms-777 ms, literature: 761 ms).

The main disadvantage of inversion-prepared $T_1$ determination techniques is that a certain waiting time is required before each measurement in order for the magnetization to relax back to equilibrium. To enable the use of the presented method for dynamic $T_1$ mapping, a correction of insufficient relaxation between two successive inversions was integrated in chapter 6. First, the presented combination of a model-based $T_1$ determination and a correction for insufficient relaxation was validated in 7 healthy subjects (maximum temporal deviations of 3.6 % in GM and 1.8 % in WM), before it was used for dynamic contrast-enhanced $T_1$ mapping in a brain tumor. In cooperation with Prof. Dr. Uwe Klose and the *Department of Diagnostic and Interventional Neuroradiology* at the *Eberhard Karls University Tübingen*, $T_1$ changes in the tumor tissue after the injection of contrast agent were tracked with a temporal resolution of 9 s.

In the next part of this thesis, the MAP algorithm was applied for preclinical MRI of small animals (chapter 7). This was performed in collaboration with Dr. Frank Kober and the *Centre de Résonance Magnétique Biologique et Médicale* at the *Aix-Marseille Université Marseille*. Here, the algorithm was implemented for perfusion measurements using arterial spin labeling (ASL). In a first measurement, the slice of interest is selectively inverted, before a global inversion is performed in a subsequent measurement. By determining a $T_1$ map for both measurements, a perfusion map can be calculated from the spatially resolved signal change. After the inversions, the acquisition of the individual k-space lines is synchronized with the heartbeat of the animals, which can considerably vary over the lengthy measurement (scan time: ~ 30 min). Instead of the typically used average inversion time over the entire acquisition, which is a very rough estimate, changes in the inversion time can be included in the reconstruction using MAP. The use of a model-based reconstruction led to a reduction of artifacts caused by respiratory motion of the animals.

The very short RF pulses used in most MRI sequences cause an excitation profile in the shape of a distribution of multiple flip angles instead of only a single flip angle in each voxel. As already briefly mentioned above, this, in turn, leads to an error in the description of the relaxation process using a mono-exponential model. While this effect was only considered by the very rough approximation of a linear combination of three exponentials in the IR-MAP implementation (see chapter 5), a detailed examination of this effect was carried out in chapter 8. Finally, a model for the exact description of the relaxation process after an inversion preparation with the inclusion of imperfect slice profiles is presented. Using this CSP model, systematic differences between the measured signal courses and the relaxation model, which were clearly visible using the conventional mono-exponential model in a phantom as well as an in vivo study, were largely eliminated. While the $T_1$ relaxation times were nearly identical for a good temporal coverage of the relaxation curves, the CSP model led to a significant improvement in the $T_1$ determination for a poor coverage (that is, only the approximately linear initial part of the relaxation curve is covered). The $T_1$ values obtained in a volunteer study were in good agreement with standard literature in both GM (CSP: 1393 ms-1527 ms, literature: 1331 ms-1470 ms) and WM (CSP: 703 ms-794 ms, literature: 761 ms). While the flip angle distribution was successfully incorporated in the relaxation model by the CSP model, partial volume effects caused by different tissue types in one voxel are still not considered by the CSP model. Therefore, the presented implementation of IR-MAP, which is based on a linear combination of multiple mono-exponential relaxation curves, is still useful for heterogeneous voxels. Alternatively, a linear combination of multiple CSP curves could be used for modeling partial volume effects.

In the last part of this thesis, the MAP reconstruction method was used for quantitative myocardial perfusion measurements (chapter 9). At this point, the CSP model was used instead of the conventional mono-exponential model. In cardiac perfusion measurements, a contrast agent is intravenously injected, and the passage of the contrast agent bolus through the cardiovascular system is then monitored. A series of saturation-prepared images is acquired over several heartbeats, to take account of potential arrhythmia and to obtain exactly the same contrast for successive heartbeats. For an absolute quantification of the myocardial perfusion, the signal changes caused by the contrast agent in the myocardium (tissue enhancement curve, TEC) have to be known with a good signal-to-noise ratio (SNR). These TECs are typically obtained from a series of images at a late stage after the saturation pulse after the administration of a high dose of contrast agent. In addition, however, an unsaturated signal change in the left ventricle (arterial input function, AIF) is required. This is usually obtained by a low-resolution image series acquired shortly after the saturation pulse or by previously acquiring an image series with a low contrast agent dose (prebolus measurement). In this chapter, the MAP algorithm was used to resolve the entire relaxation curve after the saturation pulses of each heartbeat over time and thus determine AIF and TECs from one measurement of high contrast agent dose. For an assessment of the determined AIFs as well as the quantified perfusion values, a reference AIF was additionally estimated in a prebolus acquisition. In a volunteer study (6 examinations), it was shown that AIFs determined using the conventional prebolus method still exhibit a certain level of saturation, which reflects in systematic deviations in the resulting perfusion values. By providing an opportunity of reconstructing unsaturated AIFs, the MAP algorithm could pave the way to quantitative myocardial perfusion measurements with an increased accuracy in the future.

The successful application of the introduced MAP algorithm is primarily dependent on the quality of the model used to describe the acquired dataset. Even the slightest deviations between measured data and relaxation model can result in significant errors brought about by the repeated application of the model within the iterative reconstruction. If the deviations are too large, the algorithm may even diverge, and a termination criterion must be applied to obtain meaningful results. For $T_1$ relaxometry, the most obvious errors are on the one hand flip angle distributions over the excited slice, which are caused by very short RF pulses, and on the other hand voxels of different tissue types and thus multiple $T_1$ values. These deviations can be minimized by modeling the signal by linear combinations of multiple mono-exponential or CSP curves.

Although the algorithm can, in principle, be implemented for all trajectories (for example, a Cartesian trajectory was used for the ASL measurements), non-Cartesian trajectories, for which the low frequencies and therefore much of the information about the image contrast is sampled very often, are well suited for the implementation of MAP.

The duration of one iteration of the MAP algorithm for a matrix of $256 \times 256$ pixels and 1000 relaxation times was in the order of about 1 minute. However, the implementations used in this work were only used to demonstrate the functionality of the algorithm. Thus, there are still some points in which an acceleration is possible, such as a gradual decrease of the interval of the parameter space used for the fit or a parallelization of the fit of the individual voxels. Additionally, the speed of the reconstruction crucially depends on the fitting method.

Although the presented MAP reconstruction algorithm with its 2D acquisition provides a poorer spatial resolution than conventional 3D techniques ($1.6 \times 1.6 \times 4\,\mathrm{mm}^3$ for MAP compared to up to $1 \times 1 \times 2\,\mathrm{mm}^3$ for other techniques), most of the other techniques are based on segmented 3D measurements, resulting in a lower temporal resolution than the non-segmented 2D MAP acquisition (a few seconds for MAP compared to several minutes for other techniques). Therefore, the choice of the method to be used must be made depending on the desired temporal and spatial resolution. Altogether, the MAP algorithm represents a promising method for accelerating magnetization-prepared $T_1$ measurements and could be applied in many areas of MRI in the future.

# 11 Zusammenfassung und Schlussfolgerungen

This chapter is a German translation of the *Summary and Conclusions* chapter 10.

Im Rahmen dieser Arbeit wurde ein modellbasiertes Verfahren namens MAP (engl. Model-based Acceleration of Parameter mapping) für die Bestimmung des $T_1$-Gewebeparameters mittels **M**agnet**r**esonanz**t**omographie (MRT) entwickelt. Dieser iterative Algorithmus verwendet das Vorwissen über den nach einer Magnetisierungspräparation zu erwartenden Signalverlauf, um aus einer im Anschluss an eine initiale Präparation aufgenommene zeitliche Serie stark unterabgetasteter k-Räume eine Serie voll abgetasteter k-Räume zu generieren. Eine Fourier-Transformation dieser Serie in den Bildraum zeigt den örtlich aufgelösten zeitlichen Verlauf der longitudinalen Relaxation, was eine Kartierung des Gewebeparameters $T_1$ ermöglicht.

In seiner schnellsten Form ermöglicht dieses Verfahren die Rekonstruktion einer $T_1$-Karte aus einem innerhalb weniger Sekunden nach einer passenden Magnetisierungspräparation aufgenommenen radialen Gradienten-Echo-Datensatz, während die Messdauer herkömmlich verwendeter $T_1$-Bestimmungstechniken üblicherweise im Bereich von einigen Minuten liegt. Nach der Validierung des MAP-Algorithmus für zwei unterschiedliche Arten der Magnetisierungspräparation (Sättigungspräparation, Inversion) wurde die entwickelte Technik im Rahmen dieser Arbeit in verschiedenen Bereichen der präklinischen und klinischen MRT angewendet und mögliche Vor- und Nachteile untersucht.

Die erste Version des MAP-Algorithmus basiert auf der Sättigungspräparation, bei der die longitudinale Magnetisierung vor der Datenakquirierung auf null gebracht wird. Während die Magnetisierung anschließend mit der Relaxationszeit $T_1$ zurück ins Gleichgewicht relaxiert, werden mittels einer Gradienten-Echo-Sequenz einzelne Zeilen des k-Raums ausgelesen. Durch die kontinuierliche Hochfrequenz-Anregung wird jedoch der zu bestimmende Parameter $T_1$ verkürzt und die Magnetisierung relaxiert stattdessen mit einer verkürzten Relaxationszeit $T_1^*$, die von der Repetitionszeit $T_R$ sowie dem Flipwinkel $\alpha$ der Pulssequenz abhängt. Dies verhindert eine direkte Bestimmung von $T_1$ ohne eine separate Messung des Flipwinkels. Die Sättigungspräparation hat jedoch den großen Vorteil, dass keine Wartezeiten zwischen aufeinanderfolgenden Messungen notwendig sind, da die Magnetisierung immer wieder auf null gebracht wird. Dies führt zu einer hohen potenziellen zeitlichen Auflösung in dynamischen $T_1$-Messungen. Mit Hilfe der sättigungspräparierten Implementierung des MAP-Algorithmus (SR-MAP, Kapitel 4) konnten die zur Bestimmung einer $T_1^*$-Karte des menschlichen Gehirns notwendigen

Daten innerhalb von 6.6 s nach einer einzigen Präparation akquiriert werden. Im Rahmen einer Probandenuntersuchung wurden die mittels SR-MAP bestimmten $T_1^*$-Werte mit den Ergebnissen einer segmentierten Messung (Messdauer: 24 min) verglichen. Dabei fielen die Unterschiede mit 1.3 % in der weißen Gehirnsubstanz (engl. white matter, WM), 2.4 % in der grauen Gehirnsubstanz (engl. grey matter, GM) und 4.0 % im Liquor (engl. Cerebrospinal fluid, CSF) sehr gering aus. Es wurde dabei eine perfekte Sättigung angenommen, was die numerische Komplexität stark vereinfacht, jedoch auch zu Fehlern in der iterativen Rekonstruktion führen kann, wenn das tatsächlich gemessene Signal nicht perfekt gesättigt wurde. Außerdem wurde in jedem Bildvoxel nur ein einziger exponentieller Verlauf angenommen, was ebenfalls zu Fehlern in Voxeln führen kann, in denen sich mehrere Gewebetypen befinden oder in denen durch schlechte Anregungsprofile mit unterschiedlichen Flipwinkeln angeregt wird.

Um die direkte Bestimmung des Gewebeparameters $T_1$ zu ermöglichen, wurde der MAP-Algorithmus in Kapitel 5 für inversionspräparierte Gradienten-Echo-Sequenzen weiterentwickelt (IR-MAP). Auch hier ergibt sich aufgrund der kontinuierlichen Hochfrequenz-Anregung eine verkürzte Relaxationszeit $T_1^*$, aus der jedoch mit Hilfe der zusätzlich vorhandenen Information über die Magnetisierung $-M_0$ direkt nach der Inversion $T_1$ bestimmt werden kann. Um außerdem das Auftreten von Voxeln mit mehreren Gewebetypen (engl. partial volume) sowie den in Schichtselektionsrichtung üblicherweise nicht konstanten Flipwinkel (durch nicht-perfekte Schichtprofile) zu berücksichtigen, wurde das mono-exponentielle Modell durch eine Linearkombination aus drei Exponentialfunktionen ersetzt. Mit diesem IR-MAP-Algorithmus wurden in 7 gesunden Probanden $T_1$-Karten einer axialen Gehirn-Schicht bestimmt. Die dabei ermittelten Werte (Messzeit: 6 s) wurden auch hier mittels einer segmentierten Messung (Messzeit: 30 min) validiert. Die Differenz zwischen den $T_1$-Werten beider Messungen war in grauer und weißer Gehirnsubstanz kleiner als 5.1 %. Außerdem stimmten die bestimmten $T_1$-Werte sowohl im GM (IR-MAP: 1395 ms-1455 ms, Literatur: 1331 ms-1470 ms) als auch im WM (IR-MAP: 676 ms-777 ms, Literatur: 761 ms) sehr gut mit gängigen Literaturwerten überein.

Der Nachteil dieser inversionspräparierten $T_1$-Bestimmung ist, dass vor jeder Messung eine gewisse Wartezeit eingehalten werden muss, damit die Magnetisierung wieder zurück ins Gleichgewicht relaxieren kann. Um die vorgestellte Methodik auch für dynamische $T_1$-Messungen verwenden zu können, wurde in Kapitel 6 eine Korrektur der unzureichenden Relaxation zwischen zwei aufeinanderfolgenden Inversionen eingebaut. Die vorgestellte Kombination aus $T_1$-Bestimmung und $T_1$-Korrektur wurde zunächst an 7 gesunden Probanden validiert (maximale zeitliche Abweichungen von 3.6 % im GM und 1.8 % im WM), um das Verfahren schließlich für eine dynamische kontrastmittelgestützte $T_1$-Messung in einem Gehirntumor zu verwenden. In Zusammenarbeit mit Prof. Dr. Uwe Klose und der *Abteilung für Diagnostische und Interventionelle Neuroradiologie* der *Eberhard Karls Universität Tübingen* konnte die $T_1$-Änderung im Tumorgewebe nach der Kontrastmittelgabe mit einer zeitlichen Auflösung von 9 s aufgezeichnet werden.

Im nächsten Teil der Arbeit wurde der MAP-Algorithmus in der präklinischen MR-Bildgebung am Kleintier eingesetzt (Kapitel 7). Dies wurde in Kooperation mit Dr.

Frank Kober und dem *Centre de Résonance Magnétique Biologique et Médicale* der *Aix-Marseille Université Marseille* durchgeführt. Hierbei wurde der Algorithmus für die Perfusions-Bestimmung mittels der Arterial-Spin-Labeling-Methode verwendet. Dabei wird in einer ersten Messung die zu betrachtende Schicht selektiv invertiert und in einer darauffolgenden Messung nochmals das gesamte Volumen. Bestimmt man für beide Messungen jeweils eine $T_1$-Karte, so kann man aus der räumlich aufgelösten Signaländerung eine Perfusionskarte bestimmen. Nach der Inversion wird die Messung der einzelnen k-Raum-Linien üblicherweise mit dem Herzschlag der Kleintiere synchronisiert, der jedoch über die langwierige Messung (ca. 30 min) stark variieren kann. Statt der üblicherweise verwendeten, über alle Herzschläge und damit sehr grob gemittelten Inversionszeit, konnten durch Einbezug des MAP-Algorithmus Änderungen in der Inversionszeit in die Rekonstruktion miteinbezogen werden. Die Verwendung der modellbasierten Rekonstruktion führte zudem zu einer Reduzierung der Atmungsartefakte.

Die in den meisten MRT-Sequenzen für die Anregung verwendeten, sehr kurzen Hochfrequenz-Pulse führen dazu, dass in jedem Voxel statt mit einem einzigen Flipwinkel mit einer ganzen Verteilung von Filpwinkeln angeregt wird. Dies wiederum führt, wie oben bereits kurz erwähnt, zu einem Fehler bei der Beschreibung der Relaxation durch ein mono-exponentielles Modell. Während dieser Effekt bei der Implementierung des IR-MAP-Algorithmus (siehe Kapitel 5) noch durch eine recht grobe Näherung berücksichtigt wurde, erfolgt in Kapitel 8 einer detaillierte Studie dieses Effekts. Schließlich wird ein Modells für die exakte Beschreibung der Relaxation nach einer Inversionspräparation unter Einbezug der nicht-perfekten Schichtprofile vorgestellt. Mit diesem sogenannten CSP-Modell (engl. Consideration of Slice Profiles) konnten sowohl in einer Phantom-, als auch in einer Probandenstudie systematische Abweichungen zwischen den gemessenen Signalverläufen und dem Relaxationsmodell, die für das herkömmlich verwendete mono-exponentielle Modell deutlich sichtbar waren, weitgehend beseitigt werden. Während die mit beiden Modellen bestimmten $T_1$-Werte bei einer guten zeitlichen Abdeckung der Relaxationskurve nahezu identisch waren, führte das CSP-Modell zu einer deutlichen Verbesserung der $T_1$-Werte, sobald die Relaxationskurven zeitlich nicht mehr ausreichend abgedeckt waren. Die in einer Probandenstudie ermittelten $T_1$-Werte im GM (CSP: 1393 ms-1527 ms, Literatur: 1331 ms-1470 ms), aber auch im WM (CSP: 703 ms-794 ms, Literatur: 761 ms) stimmten gut mit gängigen Literaturwerten überein. Während durch das CSP-Modell die Flipwinkel-Verteilung in das Relaxationsmodell miteinbezogen werden kann, werden Partialvolumeneffekte, die durch unterschiedliche Gewebetypen in einem Voxel entstehen können, auch hier nicht berücksichtigt. Daher ist für heterogene Voxel die Verwendung der vorgestellten Implementierung von IR-MAP, deren Modell auf einer Linearkombination mono-exponentieller Signalverläufe basiert, weiterhin sinnvoll. Alternativ könnte auch eine Linearkombination aus mehreren CSP-Kurven verwendet werden, um Partialvolumeneffekte zu modellieren.

Im letzten Teil der Arbeit wurde die MAP-Rekonstruktionsmethode für die quantitative myokardiale Herzperfusionsmessung eingesetzt (Kapitel 9). An dieser Stelle wurde das CSP-Modell statt des herkömmlich verwendeten mono-exponentiellen Modells verwendet. Bei der verwendeten Herzperfusionsmessung wird Kontrastmittel injiziert und anschließend die Passage des Kontrastmittels durch den Blutkreislauf verfolgt. Dabei wird über mehrere Herzschläge eine Bilderserie aufgenommen, wobei jedes dieser Einzelbilder mit einem Sättigungspuls präpariert wird, um trotz moglicher Arrhythmien für jeden der aufeinanderfolgenden Herzschläge genau den gleichen Kontrast zu erhalten. Für eine Absolut-Quantifizierung der Herzperfusion benötigt man zunächst den Signalverlauf im Myokard (engl. Tissue Enhancement Curve, TEC) mit einem guten Signal-zu-Rausch-Verhältnis. Dabei wird üblicherweise eine Bilderserie zu einem späten Zeitpunkt nach der Sättigung bei Gabe einer hohen Kontrastmitteldosis aufgenommen. Außerdem wird jedoch ein ungesättigter Signalverlauf im linken Ventrikel (engl. Arterial Input Function, AIF) benötigt. Dieser wird üblicherweise durch ein kurz nach der Sättigung zusätzlich aufgenommenes, niedrig aufgelöstes Bild oder durch eine vorher separat mit einer niedrigen Kontrastmittel-Dosis gemessene komplette Bilderserie erreicht (Präbolus-Messung). Der MAP-Algorithmus wurde in diesem Fall verwendet, um für jeden Herzschlag den gesamten Signalverlauf nach dem Sättigungspuls zeitlich aufzulösen und somit die Bestimmung von AIF und TEC aus einer Messung mit hoher Kontrastmitteldosis zu ermöglichen. Für eine Beurteilung der ermittelten AIFs sowie der quantifizierten Perfusionswerte wurde zusätzlich eine AIF aus einer Präbolus-Messung bestimmt. In einer Probandenstudie (6 Untersuchungen) konnte gezeigt werden, dass die mit der herkömmlichen Präbolus-Methode ermittelten AIFs immer noch eine gewisse Sättigung aufweisen, was sich schließlich auch in systematischen Abweichungen in den daraus daraus ermittelten Perfusionswerten niederschlägt. Durch die Rekonstruktion einer ungesättigten AIF könnte der MAP-Algorithmus zukünftig Herzperfusionsmessungen mit einer erhöhten Genauigkeit ermöglichen.

Für eine erfolgreiche Anwendung des eingeführten MAP-Algorithmus ist in erster Linie ist die Güte des zur Beschreibung der akquirierten Datensätze verwendeten Modells ausschlaggebend. Selbst kleinste Abweichungen zwischen Messdaten und angenommenem Relaxationsmodell können durch die wiederholte Applikation des Modells im Rahmen des iterativen Verfahrens zu erheblichen Fehlern in der Rekonstruktion führen. Sind die Abweichungen zu groß, so kann der Algorithmus gar divergieren, sodass ein Abbruch-Kriterium eingesetzt werden muss, um sinnvolle Ergebnisse zu erhalten. Für die $T_1$-Relaxometrie sind die offensichtlichsten Fehler zum einen die durch kurze Hochfrequenz-Pulse verursachten Flipwinkel-Verteilungen über die angeregte Schicht, zum anderen aber auch Voxel unterschiedlicher Gewebetypen und somit unterschiedlicher $T_1$-Werte. Diese Abweichungen konnten durch die Signalmodellierung durch Linearkombinationen mehrerer Exponentialfunktionen oder mehrerer CSP-Kurven minimiert werden.

Obwohl der Algorithmus prinzipiell für alle Trajektorien implementiert werden kann - beispielsweise wurde für die ASL-Messungen eine kartesische Trajektorie verwendet - eignen sich nicht-kartesische Trajektorien, bei denen die niedrigen Frequenzen und damit ein Großteil der Information über den Bildkontrast sehr häufig abgetastet werden, vorrangig für die Implementierung von MAP.

Weiterhin ist die Bewegung des zu messenden Objektes bei der Verwendung von MAP zu beachten. Da der gesamte nach der Magnetisierungspräparation gemessene Datensatz für die Rekonstruktion einer $T_1$-Karte verwendet wird, wirkt sich Bewegung während dieser Zeitspanne von einigen Sekunden negativ auf die Rekonstruktion aus und kann zu einer schlechteren Auflösung oder sogar Fehlern in den bestimmten $T_1$-Karten führen. Für die Validierung der Methoden in dieser Arbeit wurde hauptsächlich am menschlichen Kopf gemessen, wo die Bewegung sehr gut unterdrückt werden kann. Jedoch müsste das Verfahren für Anatomien wie das menschliche Herz angepasst werden, wenn - anders als bei den Herzperfusionsmessungen in dieser Arbeit - die Messung nicht unter Atemstopp durchgeführt wird und die Datenakquisition nicht auf die Diastole beschränkt wird.

Es wurde gezeigt, dass eine unzureichende zeitliche Abdeckung des gemessenen Signalverlaufs sich negativ auf die Genauigkeit der bestimmten $T_1$-Werte auswirkt. Ist nicht genug Information über den nach dem näherungsweise linearen Anfangsteil einsetzenden exponentiellen Signalverlauf vorhanden, kann der Verlauf zwar immer noch gut modelliert werden, die Ungenauigkeit der ermittelten $T_1$-Werte nimmt jedoch mit der Größenordnung der zugrunde liegenden $T_1$-Werte zu. Daher muss die Dauer der Abtastung an die zu erwartenden $T_1$-Werte angepasst werden, wenn die Genauigkeit von $T_1$ für die Messung von Bedeutung ist. Soll lediglich der Signalverlauf beschrieben werden - wie bei der AIF-Bestimmung bei der quantitativen Herzperfusionsmessung, bei der nur über ein Intervall von 200 ms gemessen werden konnte - so genügt auch eine geringere zeitlich Abdeckung der Kurve.

Obwohl MAP zunächst für anfänglich fast "leere" k-Räume implementiert wurde, die lediglich aus den zu den einzelnen Zeitpunkten gemessenen Daten bestehen, so kann das Konvergenzverhalten deutlich verbessert werden, indem die Ausgangs-k-Räume vor der ersten Iteration beispielsweise durch eine lineare Interpolation durch alle Zeitpunkte aufgefüllt werden.

Die Dauer für eine Iteration des MAP-Algorithmus bei einer Matrix von $256 \times 256$ Pixeln und 1000 Relaxationszeitpunkten war ungefähr in der Größenordnung von einer Minute. Die in dieser Arbeit verwendeten Implementierungen dienten jedoch lediglich als Beweis der Funktionalität des Algorithmus. Dieser könnte an einigen Stellen noch deutlich beschleunigt werden, beispielsweise durch eine sukzessive Intervallverkleinerung kleinerer Parameterräume oder eine Parallelisierung des Fittings in den einzelnen Voxeln. Außerdem hängt die Geschwindigkeit von der Art des Fittings ab.

Im Vergleich zu anderen Techniken der $T_1$-Bestimmung bietet der für 2D-Messungen vorgestellte MAP-Algorithmus zwar eine schlechtere räumliche Auflösung als herkömmliche 3D-Techniken ($1.6 \times 1.6 \times 4\,\text{mm}^3$ für MAP verglichen mit bis zu $1 \times 1 \times 2\,\text{mm}^3$ für andere Techniken), jedoch handelt es sich bei den anderen Verfahren meist um segmentierte 3D Messungen, weshalb die zeitliche Auflösung bei der nicht-segmentierten 2D MAP-Akquisition deutlich höher ist (einige Sekunden für MAP verglichen mit mehreren Minuten für andere Techniken). Demnach muss die Auswahl der Technik in Abhängigkeit der gewünschten zeitlichen sowie räumlichen Auflösung erfolgen. Insgesamt stellt der MAP-Algorithmus eine vielversprechende Methode zur Beschleunigung magnetisierungspräparierter Messungen dar und könnte zukünftig in vielen Bereichen der MRT Verwendung finden.

# 12 Outlook

In this doctoral thesis, a model-based reconstruction method for magnetization-prepared MRI acquisitions was developed and applied for acceleration in a wide range of MR acquisitions. However, these applications of MAP only provide a small impression on what could be achieved by the application of model-based reconstruction techniques in quantitative MR parameter mapping or other magnetization-prepared acquisition techniques such as arterial spin labeling and myocardial first-pass perfusion measurements in the future.

Although the acquisition time was greatly reduced in all implementations of MAP presented in this work, the reconstruction time lied in the range of several minutes to several hours, depending on the particular applicaition and the size of the dataset. In contrast to the majority of routinely used post-processing methods where the final images can be viewed only a few moments after the scan, the MAP algorithm goes along with a trade-off between scan time and reconstruction time. A reduction in acquisition time results in an extension of the reconstruction time. While a moderate undersampling factor can be used to reduce the required reconstruction time in applications where the temporal resolution is of no particular importance, high undersampling factors can be used if the temporal resolution has to stay within a certain limit (e.g. if data collection is performed in diastole only as in first-pass perfusion imaging). In these cases, the reconstruction time on a standard PC would be considerably too long for clinical examinations. Besides the acceleration of the fitting method to be used, the MAP algorithm could be implemented on a powerful multi-core computer to guarantee its clinical relevance.

Another important point which has to be addressed in future work is the susceptibility of the current MAP implementations to motion of the object within the scan time of several seconds. If this motion cannot be prevented, such as the cardiac and respiratory cycle in first-pass perfusion imaging, an image registration would have to be included in the model-based reconstruction to ensure a reliable parameter mapping.

One last point for potential improvements are the sampling trajectories with which the relaxation process is tracked. Radial trajectories which provide a good coverage of the low spatial frequencies were used for data collection in all but one MAP implementation performed in this work. Alternatively, the reconstructions might be even further improved using spiral readouts. While the low spatial frequencies are still well covered by spiral sampling patterns, each spiral arm encodes more than one dimension in the pseudo-2D-k-space. Therefore, more spatial information than for a radial projection is available for each acquisition time point after the magnetization preparation. Using spiral trajectories, datasets of a similar temporal resolution but with considerably more information could be acquired in the future.

# A Bibliography

[1] N. Al-Saadi, E. Nagel, M. Gross, B. Schnackenburg, I. Paetsch, C. Klein, and E. Fleck. Improvement of myocardial perfusion reserve early after coronary intervention: assessment with cardiac magnetic resonance imaging. *J Am Coll Cardiol*, 36(5):1557–64, 2000.

[2] D. J. Atkinson, D. Burstein, and R. R. Edelman. First-pass cardiac perfusion: evaluation with ultrafast MR imaging. *Radiology*, 174(3 Pt 1):757–62, 1990.

[3] W. R. Bauer, K. H. Hiller, P. Galuppo, S. Neubauer, J. Kopke, A. Haase, C. Waller, and G. Ertl. Fast high-resolution magnetic resonance imaging demonstrates fractality of myocardial perfusion in microscopic dimensions. *Circ Res*, 88(3):340–6, 2001.

[4] Bayer Inc., 77 Belfield Road, Toronto, ON, M9W 1G6, Canada. *GADOVIST® 1.0 - Contrast Enhancement Agent for Magnetic Resonance Imaging (MRI)*, March 2014.

[5] V. Belle, E. Kahler, C. Waller, E. Rommel, S. Voll, K. H. Hiller, W. R. Bauer, and A. Haase. In vivo quantitative mapping of cardiac perfusion in rats using a noninvasive MR spin-labeling method. *J Magn Reson Imag*, 8(6):1240–5, 1998.

[6] M. Bernstein, K. King, and X. Zhou. *Handbook of MRI Pulse Sequences*. Elsevier Science, 2004.

[7] M. Blaimer, F. Breuer, M. Mueller, R. M. Heidemann, M. A. Griswold, and P. M. Jakob. SMASH, SENSE, PILS, GRAPPA: how to choose the optimal method. *Top Magn Reson Imaging*, 15(4):223–36, 2004.

[8] K. T. Block, M. Uecker, and J. Frahm. Model-based iterative reconstruction for radial fast spin-echo MRI. *IEEE Trans Med Imag*, 28(11):1759–69, 2009.

[9] S. Bluml, L. R. Schad, B. Stepanow, and W. J. Lorenz. Spin-lattice relaxation time measurement by means of a TurboFLASH technique. *Magn Reson Med*, 30(3):289–95, 1993.

[10] P. A. Brex, G. J. Parker, S. M. Leary, P. D. Molyneux, G. J. Barker, C. A. Davie, A. J. Thompson, and D. H. Miller. Lesion heterogeneity in multiple sclerosis: a study of the relations between appearances on T1 weighted images, T1 relaxation times, and metabolite concentrations. *J Neurol Neurosurg Psychiatry*, 68(5):627–32, 2000.

[11] E. J. Candes, J. Romberg, and T. Tao. Robust uncertainty principles: Exact signal reconstruction from highly incomplete frequency information. *IEEE Trans Inf Theory*, 52(2):489–509, 2006.

[12] M. D. Cerqueira, N. J. Weissman, V. Dilsizian, A. K. Jacobs, S. Kaul, W. K. Laskey, D. J. Pennell, J. A. Rumberger, T. Ryan, M. S. Verani, S. American Heart Association Writing Group on Myocardial, and I. Registration for Cardiac. Standardized myocardial segmentation and nomenclature for tomographic imaging of the heart. A statement for healthcare professionals from the Cardiac Imaging Committee of the Council on Clinical Cardiology of the American Heart Association. *Circulation*, 105(4):539–42, 2002.

[13] K. T. Cheng. Gadobutrol (Molecular Imaging and Contrast Agent Database). `http://www.ncbi.nlm.nih.gov/books/NBK23589/`, February 2007.

[14] K. Chow, J. A. Flewitt, J. D. Green, J. J. Pagano, M. G. Friedrich, and R. B. Thompson. Saturation recovery single-shot acquisition (SASHA) for myocardial T1 mapping. *Magn Reson Med*, 71(6):2082–95, 2014.

[15] T. F. Christian, A. H. Aletras, and A. E. Arai. Estimation of absolute myocardial blood flow during first-pass MR perfusion imaging using a dual-bolus injection technique: comparison to single-bolus injection method. *J Magn Reson Imag*, 27(6):1271–7, 2008.

[16] T. F. Christian, D. W. Rettmann, A. H. Aletras, S. L. Liao, J. L. Taylor, R. S. Balaban, and A. E. Arai. Absolute myocardial perfusion in canines measured by using dual-bolus first-pass MR imaging. *Radiology*, 232(3):677–84, 2004.

[17] M. A. Cooper, T. D. Nguyen, P. Spincemaille, M. R. Prince, J. W. Weinsaft, and Y. Wang. Flip angle profile correction for T(1) and T(2) quantification with Look-Locker inversion recovery 2D steady-state free precession imaging. *Magn Reson Med*, 68(5):1579–85, 2012.

[18] A. P. Crawley and R. M. Henkelman. A comparison of one-shot and recovery methods in T1 imaging. *Magn Reson Med*, 7(1):23–34, 1988.

[19] R. Deichmann. Fast high-resolution T1 mapping of the human brain. *Magn Reson Med*, 54(1):20–7, 2005.

[20] R. Deichmann and A. Haase. Quantification of T1 values by SNAPSHOT-FLASH NMR imaging. *J Magn Reson*, 96(3):608–612, 1992.

[21] R. Deichmann, D. Hahn, and A. Haase. Fast T1 mapping on a whole-body scanner. *Magn Reson Med*, 42(1):206–9, 1999.

[22] S. C. Deoni, B. K. Rutt, and T. M. Peters. Rapid combined T1 and T2 mapping using gradient recalled acquisition in the steady state. *Magn Reson Med*, 49(3):515–26, 2003.

[23] D. DeSimone, M. Morris, C. Rhoda, T. Lucas, J. Zielonka, A. Olukotun, and M. Carvlin. Evaluation of the safety and efficacy of gadoteridol injection (a low osmolal magnetic resonance contrast agent). clinical trials report. *Invest Radiol*, 26 Suppl 1:S212–6; discussion S232–5, 1991.

[24] O. Dietrich, J. G. Raya, S. B. Reeder, M. F. Reiser, and S. O. Schoenberg. Measurement of signal-to-noise ratios in MR images: influence of multichannel coils, parallel imaging, and reconstruction filters. *J Magn Reson Imaging*, 26(2):375–85, 2007.

[25] M. Doneva, P. Bornert, H. Eggers, C. Stehning, J. Senegas, and A. Mertins. Compressed sensing reconstruction for magnetic resonance parameter mapping. *Magn Reson Med*, 64(4):1114–20, 2010.

[26] D. L. Donoho. Compressed sensing. *IEEE Trans Inf Theory*, 52(4):1289–1306, 2006.

[27] P. Ehses, N. Seiberlich, D. Ma, F. A. Breuer, P. M. Jakob, M. A. Griswold, and V. Gulani. IR TrueFISP with a golden-ratio-based radial readout: fast quantification of T1, T2, and proton density. *Magn Reson Med*, 69(1):71–81, 2013.

[28] M. Elad and M. Aharon. Image denoising via sparse and redundant representations over learned dictionaries. *IEEE Trans Image Process*, 15(12):3736–45, 2006.

[29] F. H. Epstein, r. Mugler, J. P., and J. R. Brookeman. Spoiling of transverse magnetization in gradient-echo (GRE) imaging during the approach to steady state. *Magn Reson Med*, 35(2):237–45, 1996.

[30] T. Ethofer, I. Mader, U. Seeger, G. Helms, M. Erb, W. Grodd, A. Ludolph, and U. Klose. Comparison of longitudinal metabolite relaxation times in different regions of the human brain at 1.5 and 3 Tesla. *Magn Reson Med*, 50(6):1296–301, 2003.

[31] D. G. Gadian, J. A. Payne, D. J. Bryant, I. R. Young, D. H. Carr, and G. M. Bydder. Gadolinium-DTPA as a contrast agent in MR imaging-theoretical projections and practical observations. *J Comput Assist Tomo*, 9(2):242–251, 1985.

[32] U. Gamper, P. Boesiger, and S. Kozerke. Compressed sensing in dynamic MRI. *Magn Reson Med*, 59(2):365–373, 2008.

[33] P. D. Gatehouse, A. G. Elkington, N. A. Ablitt, G. Z. Yang, D. J. Pennell, and D. N. Firmin. Accurate assessment of the arterial input function during high-dose myocardial perfusion cardiovascular magnetic resonance. *J Magn Reson Imag*, 20(1):39–45, 2004.

[34] B. L. Gerber, S. V. Raman, K. Nayak, F. H. Epstein, P. Ferreira, L. Axel, and D. L. Kraitchman. Myocardial first-pass perfusion cardiovascular magnetic resonance: history, theory, and current state of the art. *J Cardiov Magn Reson*, 10:18, 2008.

[35] G. H. Glover and J. M. Pauly. Projection reconstruction techniques for reduction of motion effects in MRI. *Magn Reson Med*, 28(2):275–89, 1992.

[36] M. A. Griswold, P. M. Jakob, R. M. Heidemann, M. Nittka, V. Jellus, J. Wang, B. Kiefer, and A. Haase. Generalized autocalibrating partially parallel acquisitions (GRAPPA). *Magn Reson Med*, 47(6):1202–10, 2002.

[37] W. Grodd and R. C. Brasch. Magneto-pharmaceutic contrast changes in nuclear magnetic resonance tomography. *RoFo-Fortschr Rontg*, 145(2):130–9, 1986.

[38] E. M. Haacke. *Magnetic resonance imaging : physical principles and sequence design*. Wiley, 1st edition, 1999.

[39] A. Haase. Snapshot Flash Mri - Applications to T1, T2, and Chemical-Shift Imaging. *Magn Reson Med*, 13(1):77–89, 1990.

[40] A. Haase, J. Frahm, D. Matthaei, W. Hanicke, and K. D. Merboldt. FLASH imaging. rapid NMR imaging using low flip-angle pulses. *J Magn Reson*, 67(2):258–266, 1986.

[41] R. M. Heidemann, M. A. Griswold, A. Haase, and P. M. Jakob. VD-AUTO-SMASH Imaging. *Magn Reson Med*, 45(6):1066–1074, 2001.

[42] J. Hennig, A. Nauerth, and H. Friedburg. RARE imaging: a fast imaging method for clinical MR. *Magn Reson Med*, 3(6):823–33, 1986.

[43] M. Hoehn-Berlage, M. Eis, T. Back, K. Kohno, and K. Yamashita. Changes of relaxation times (T1, T2) and apparent diffusion coefficient after permanent middle cerebral artery occlusion in the rat: temporal evolution, regional extent, and comparison with histology. *Magn Reson Med*, 34(6):824–34, 1995.

[44] L. Y. Hsu, K. L. Rhoads, J. E. Holly, P. Kellman, A. H. Aletras, and A. E. Arai. Quantitative myocardial perfusion analysis with a dual-bolus contrast-enhanced first-pass MRI technique in humans. *J Magn Reson Imag*, 23(3):315–22, 2006.

[45] L. Iles, H. Pfluger, A. Phrommintikul, J. Cherayath, P. Aksit, S. N. Gupta, D. M. Kaye, and A. J. Taylor. Evaluation of diffuse myocardial fibrosis in heart failure with cardiac magnetic resonance contrast-enhanced t1 mapping. *J Am Coll Cardiol*, 52(19):1574–80, 2008.

[46] J. I. Jackson, C. H. Meyer, D. G. Nishimura, and A. Macovski. Selection of a convolution function for Fourier inversion using gridding. *IEEE Trans Med Imag*, 10(3):473–8, 1991.

[47] M. Jerosch-Herold, N. Wilke, and A. E. Stillman. Magnetic resonance quantification of the myocardial perfusion reserve with a Fermi function model for constrained deconvolution. *Med Phys*, 25(1):73–84, 1998.

[48] E. G. Kholmovski and E. V. DiBella. Perfusion MRI with radial acquisition for arterial input function assessment. *Magn Reson Med*, 57(5):821–7, 2007.

[49] D. Kim and L. Axel. Multislice, dual-imaging sequence for increasing the dynamic range of the contrast-enhanced blood signal and cnr of myocardial enhancement at 3t. *J Magn Reson Imag*, 23(1):81–6, 2006.

[50] D. Kim, N. Oesingmann, and K. McGorty. Hybrid adiabatic-rectangular pulse train for effective saturation of magnetization within the whole heart at 3 T. *Magn Reson Med*, 62(6):1368–78, 2009.

[51] T. H. Kim, N. A. Pack, L. Chen, and E. V. DiBella. Quantification of myocardial perfusion using CMR with a radial data acquisition: comparison with a dual-bolus method. *J Cardiov Magn Reson*, 12:45, 2010.

[52] P. B. Kingsley, R. J. Ogg, W. E. Reddick, and R. G. Steen. Correction of errors caused by imperfect inversion pulses in MR imaging measurement of T1 relaxation times. *Magn Reson Imag*, 16(9):1049–55, 1998.

[53] U. Klose, S. Bisdas, H. Köstler, and J. Tran-Gia. Evaluation of Vascular Transfer Constants using Dynamic T1-Mapping during Contrast Agent Administration. *Proc ISMRM*, 22:2748, 2014.

[54] F. Kober, I. Iltis, M. Izquierdo, M. Desrois, D. Ibarrola, P. J. Cozzone, and M. Bernard. High-resolution myocardial perfusion mapping in small animals in vivo by spin-labeling gradient-echo imaging. *Magn Reson Med*, 51(1):62–7, 2004.

[55] H. Köstler, C. Ritter, M. Lipp, M. Beer, D. Hahn, and J. Sandstede. Prebolus quantitative MR heart perfusion imaging. *Magn Reson Med*, 52(2):296–9, 2004.

[56] H. Köstler, C. Ritter, M. Reiss-Zimmermann, M. Beer, D. Hahn, and J. Sandstede. Correction for partial volume errors in MR heart perfusion imaging. *Magn Reson Med*, 51(4):848–52, 2004.

[57] K. Levenberg. A method for the solution of certain non-linear problems in least squares. *Q Appl Math*, 2(2):164–168, 1944.

[58] J. Listerud, S. Einstein, E. Outwater, and H. Y. Kressel. First principles of fast spin echo. *Magn Reson Q*, 8(4):199–244, 1992.

[59] D. C. Look and D. R. Locker. Time saving in measurement of NMR and EPR relaxation times. *Rev Sci Instrum*, 41:250–51, 1970.

[60] M. Lustig, D. Donoho, and J. M. Pauly. Sparse MRI: The application of compressed sensing for rapid MR imaging. *Magn Reson Med*, 58(6):1182–95, 2007.

[61] W. J. Manning, D. J. Atkinson, W. Grossman, S. Paulin, and R. R. Edelman. First-pass nuclear magnetic resonance imaging studies using gadolinium-DTPA in patients with coronary artery disease. *J Am Coll Cardiol*, 18(4):959–65, 1991.

[62] D. W. McRobbie. *MRI from picture to proton*. Cambridge University Press, 2nd edition, 2007.

[63] D. R. Messroghli, S. Nordmeyer, T. Dietrich, O. Dirsch, E. Kaschina, K. Savvatis, O. h.-I. D, C. Klein, F. Berger, and T. Kuehne. Assessment of diffuse myocardial fibrosis in rats using small-animal look-locker inversion recovery t1 mapping. *Circ Cardiovasc Imaging*, 4(6):636–40, 2011.

[64] C. H. Meyer, B. S. Hu, D. G. Nishimura, and A. Macovski. Fast spiral coronary artery imaging. *Magn Reson Med*, 28(2):202–13, 1992.

[65] V. Mlynarik, S. Gruber, and E. Moser. Proton T (1) and T (2) relaxation times of human brain metabolites at 3 Tesla. *NMR Biomed*, 14(5):325–31, 2001.

[66] M. Nahrendorf, J. U. Streif, K. H. Hiller, K. Hu, P. Nordbeck, O. Ritter, D. Sosnovik, L. Bauer, S. Neubauer, P. M. Jakob, G. Ertl, M. Spindler, and W. R. Bauer. Multimodal functional cardiac MRI in creatine kinase-deficient mice reveals subtle abnormalities in myocardial perfusion and mechanics. *Am J Physiol Heart-C*, 290(6):H2516–21, 2006.

[67] H. Neeb, V. Ermer, T. Stocker, and N. J. Shah. Fast quantitative mapping of absolute water content with full brain coverage. *NeuroImage*, 42(3):1094–109, 2008.

[68] N. A. Pack, S. Vijayakumar, T. H. Kim, C. J. McGann, and E. V. R. DiBella. A Semi-Automatic Software Package for Analysis of Dynamic Contrast-Enhanced MRI Myocardial Perfusion Studies. *Comput Cardiol*, 36:269–72, 2009.

[69] G. J. Parker, J. Suckling, S. F. Tanner, A. R. Padhani, P. B. Revell, J. E. Husband, and M. O. Leach. Probing tumor microvascularity by measurement, analysis and display of contrast agent uptake kinetics. *J Magn Reson Imag*, 7(3):564–74, 1997.

[70] J. Pauly, D. Nishimura, and A. Macovski. A k-space analysis of small-tip-angle excitation. *J Magn Reson*, 81(1):43–56, 1989.

[71] T. Paus, D. L. Collins, A. C. Evans, G. Leonard, B. Pike, and A. Zijdenbos. Maturation of white matter in the human brain: a review of magnetic resonance studies. *Brain Res Bull*, 54(3):255–66, 2001.

[72] F. Pediconi, C. Catalano, R. Occhiato, F. Venditti, F. Fraioli, A. Napoli, M. A. Kirchin, and R. Passariello. Breast lesion detection and characterization at contrast-enhanced MR mammography: gadobenate dimeglumine versus gadopentetate dimeglumine. *Radiology*, 237(1):45–56, 2005.

[73] M. D. Plumbley, T. Blumensath, L. Daudet, R. Gribonval, and D. M. E. Sparse representations in audio and music: from coding to source separation. *Proc IEEE*, 98:995–1005, 2009.

[74] C. Preibisch and R. Deichmann. Influence of RF spoiling on the stability and accuracy of T1 mapping based on spoiled FLASH with varying flip angles. *Magn Reson Med*, 61(1):125–35, 2009.

[75] K. P. Pruessmann, M. Weiger, M. B. Scheidegger, and P. Boesiger. SENSE: sensitivity encoding for fast MRI. *Magn Reson Med*, 42(5):952–62, 1999.

[76] H. C. Roberts, T. P. Roberts, R. C. Brasch, and W. P. Dillon. Quantitative measurement of microvascular permeability in human brain tumors achieved using dynamic contrast-enhanced mr imaging: correlation with histologic grade. *AJNR Am J Neuroradiol*, 21(5):891–9, 2000.

[77] R. Rubinstein, A. M. Bruckstein, and M. Elad. Dictionaries for sparse representation modeling. *Proc IEEE*, 98(6):1045–1057, 2010.

[78] R. Rubinstein, M. Zibulevsky, and M. Elad. Efficient implementation of the K-SVD algorithm using batch orthogonal matching pursuit. *CS, Technion*, 2008.

[79] J. J. Sandstede, C. Lipke, M. Beer, K. Harre, T. Pabst, W. Kenn, S. Neubauer, and D. Hahn. Analysis of first-pass and delayed contrast-enhancement patterns of dysfunctional myocardium on MR imaging: use in the prediction of myocardial viability. *Am J Roentgenol*, 174(6):1737–40, 2000.

[80] N. Seiberlich, F. Breuer, M. Blaimer, P. Jakob, and M. Griswold. Self-calibrating GRAPPA operator gridding for radial and spiral trajectories. *Magn Reson Med*, 59(4):930–5, 2008.

[81] N. Seiberlich, F. A. Breuer, M. Blaimer, K. Barkauskas, P. M. Jakob, and M. A. Griswold. Non-cartesian data reconstruction using GRAPPA operator gridding (GROG). *Magn Reson Med*, 58(6):1257–65, 2007.

[82] N. J. Shah, M. Zaitsev, S. Steinhoff, and K. Zilles. A new method for fast multislice T(1) mapping. *NeuroImage*, 14(5):1175–85, 2001.

[83] C. Siversson, C. J. Tiderius, L. Dahlberg, and J. Svensson. Local flip angle correction for improved volume T1-quantification in three-dimensional dGEMRIC using the Look-Locker technique. *J Magn Reson Imag*, 30(4):834–41, 2009.

[84] D. K. Sodickson and W. J. Manning. Simultaneous acquisition of spatial harmonics (SMASH): fast imaging with radiofrequency coil arrays. *Magn Reson Med*, 38(4):591–603, 1997.

[85] H. K. Song and L. Dougherty. k-space weighted image contrast (KWIC) for contrast manipulation in projection reconstruction MRI. *Magn Reson Med*, 44(6):825–32, 2000.

[86] D. Stäb, J. Tran-Gia, C. O. Ritter, D. Hahn, and H. Köstler. AIF determination for quantitative myocardial perfusion imaging using a model based reconstruction of radially acquired data. *Proc ISMRM*, 19:1341, 2011.

[87] R. G. Steen, S. A. Gronemeyer, P. B. Kingsley, W. E. Reddick, J. S. Langston, and J. S. Taylor. Precise and accurate measurement of proton T1 in human brain in vivo: validation and preliminary clinical application. *J Magn Reson Imag*, 4(5):681–91, 1994.

[88] S. Steinhoff, M. Zaitsev, K. Zilles, and N. J. Shah. Fast T(1) mapping with volume coverage. *Magn Reson Med*, 46(1):131–40, 2001.

[89] J. U. Streif, M. Nahrendorf, K. H. Hiller, C. Waller, F. Wiesmann, E. Rommel, A. Haase, and W. R. Bauer. In vivo assessment of absolute perfusion and intracapillary blood volume in the murine myocardium by spin labeling magnetic resonance imaging. *Magn Reson Med*, 53(3):584–92, 2005.

[90] T. J. Sumpf, M. Uecker, S. Boretius, and J. Frahm. Model-based nonlinear inverse reconstruction for T2 mapping using highly undersampled spin-echo MRI. *J Magn Reson Imag*, 34(2):420–8, 2011.

[91] B. Takase, M. Nagata, T. Kihara, A. Kameyawa, K. Noya, T. Matsui, F. Ohsuzu, M. Ishihara, and A. Kurita. Whole-heart dipyridamole stress first-pass myocardial perfusion MRI for the detection of coronary artery disease. *Jpn Heart J*, 45(3):475–86, 2004.

[92] B. Tombach and P. Reimer. Soluble paramagnetic chelates and stabilized colloidal particle solutions of iron oxides as contrast agents for magnetic resonance imaging. *Curr Med Chem*, 12(23):2795–804, 2005.

[93] J. Tran-Gia, S. Bisdas, H. Köstler, and U. Klose. A Model-based Reconstruction Technique for Fast Dynamic T1 mapping. *Proc ISMRM*, 22:3130, 2014.

[94] J. Tran-Gia, D. Stäb, T. Wech, D. Hahn, and H. Köstler. Model-based Acceleration of Parameter mapping (MAP) for saturation prepared radially acquired data. *Magn Reson Med*, 70(6):1524–34, 2013.

[95] J. Tran-Gia, T. Troalen, H. Köstler, and F. Kober. A Model-Based Reconstruction Technique for Look-Locker FAIR Gradient Echo ASL Perfusion Data. *Proc ISMRM*, 21:1321, 2013.

[96] J. Tran-Gia, T. Wech, T. A. Bley, and H. Köstler. Model-Based Acceleration of Look-Locker T1 Mapping. *Manuscript submitted for publication in PLOS ONE*, 2014.

[97] J. Tran-Gia, T. Wech, D. Hahn, T. A. Bley, and H. Köstler. Consideration of slice profiles in inversion recovery Look-Locker relaxation parameter mapping. *Magn Reson Imag, doi: 10.1016/j.mri.2014.05.012*, 2014.

[98] M. F. Tweedle. Physicochemical properties of gadoteridol and other magnetic resonance contrast agents. *Invest Radiol*, 27 Suppl 1:S2–6, 1992.

[99] M. H. Vandsburger, R. L. Janiczek, Y. Xu, B. A. French, C. H. Meyer, C. M. Kramer, and F. H. Epstein. Improved arterial spin labeling after myocardial infarction in mice using cardiac and respiratory gated look-locker imaging with fuzzy C-means clustering. *Magn Reson Med*, 63(3):648–57, 2010.

[100] R. Venkatesan, W. Lin, and E. M. Haacke. Accurate determination of spin-density and T1 in the presence of RF-field inhomogeneities and flip-angle miscalibration. *Magn Reson Med*, 40(4):592–602, 1998.

[101] C. Waller, T. Engelhorn, K. H. Hiller, G. Heusch, G. Ertl, W. R. Bauer, and R. Schulz. Impaired resting perfusion in viable myocardium distal to chronic coronary stenosis in rats. *Am J Physiol-Heart C*, 288(6):H2588–93, 2005.

[102] C. Waller, K. H. Hiller, E. Kahler, K. Hu, M. Nahrendorf, S. Voll, A. Haase, G. Ertl, and W. R. Bauer. Serial magnetic resonance imaging of microvascular remodeling in the infarcted rat heart. *Circulation*, 103(11):1564–9, 2001.

[103] C. Waller, K. H. Hiller, D. Pfaff, S. Gattenlohner, G. Ertl, and W. R. Bauer. Functional mechanisms of myocardial microcirculation in left ventricular hypertrophy: a hypothetical model of capillary remodeling post myocardial infarction. *Microvasc Res*, 75(1):104–11, 2008.

[104] C. Waller, K. H. Hiller, T. Rudiger, G. Kraus, C. Konietzko, N. Hardt, G. Ertl, and W. R. Bauer. Noninvasive imaging of angiogenesis inhibition following nitric oxide synthase blockade in the ischemic rat heart in vivo. *Microcirculation*, 12(4):339–47, 2005.

[105] C. Waller, E. Kahler, K. H. Hiller, K. Hu, M. Nahrendorf, S. Voll, A. Haase, G. Ertl, and W. R. Bauer. Myocardial perfusion and intracapillary blood volume in rats at rest and with coronary dilatation: MR imaging in vivo with use of a spin-labeling technique. *Radiology*, 215(1):189–97, 2000.

[106] J. P. Wansapura, S. K. Holland, R. S. Dunn, and J. Ball, W. S. NMR relaxation times in the human brain at 3.0 Tesla. *J Magn Reson Imag*, 9(4):531–8, 1999.

[107] N. Wilke, M. Jerosch-Herold, Y. Wang, Y. Huang, B. V. Christensen, A. E. Stillman, K. Ugurbil, K. McDonald, and R. F. Wilson. Myocardial perfusion reserve: assessment with multisection, quantitative, first-pass MR imaging. *Radiology*, 204(2):373–84, 1997.

[108] S. Winkelmann, T. Schaeffter, T. Koehler, H. Eggers, and O. Doessel. An optimal radial profile order based on the golden ratio for time-resolved MRI. *IEEE Trans Med Imag*, 26(1):68–76, 2007.

[109] W. T. Yuh, J. D. Engelken, M. G. Muhonen, N. A. Mayr, D. J. Fisher, and J. C. Ehrhardt. Experience with high-dose gadolinium MR imaging in the evaluation of brain metastases. *Am J Neuroradiol*, 13(1):335–45, 1992.

[110] D. C. Zhu and R. D. Penn. Full-brain T1 mapping through inversion recovery fast spin echo imaging with time-efficient slice ordering. *Magn Reson Med*, 54(3):725–31, 2005.

[111] Y. Zur, M. L. Wood, and L. J. Neuringer. Spoiling of transverse magnetization in steady-state sequences. *Magn Reson Med*, 21(2):251–63, 1991.

# B Curriculum Vitae

## Johannes Tran-Gia

### Personal Information

| | |
|---|---|
| Place of Birth | Stuttgart, Germany |
| Nationality | German |
| Place of Residence | Würzburg, Germany |

### Education

| | |
|---|---|
| 04/2011 - present | **Graduate School of Life Sciences**<br>University of Würzburg, Germany<br>*Degree:* PhD (Dr. rer. nat.)<br>*Estimated Completion:* 01/2015 |
| 10/2004 - 06/2010 | **Department of Physics**<br>University of Würzburg, Germany<br>*Degree:* Diploma in Physics (Grade A) |
| 10/2007 - 06/2008 | **Department of Physics**<br>Heriot-Watt University Edinburgh, Scotland<br>*Degree:* Master of Physics in Physical Science (First Class Hons) |

### Professional Experience

| | |
|---|---|
| 06/2009 - present | Part-time Employee<br>WebLabCenter Inc, Dallas, USA |
| 04/2011 - present | Research Assistant<br>Department of Diagnostic and Interventional Radiology<br>University of Würzburg, Germany |

| | |
|---|---|
| 07/2013 | Research Stay<br>Case Western Reserve University, Cleveland, USA |
| 09/2012 | Research Stay<br>Aix-Marseille University, Marseille, France |
| 10/2008 - 03/2009 | Teaching Assistant<br>Department of Physics, University of Würzburg, Germany |
| 08/2005 | Research Assistant<br>University of Canterbury, Christchurch, New Zealand |
| 08/2004 | Internship<br>ASi Connections Pte Ltd, Singapore |

## Awards & Honors

| | |
|---|---|
| 04/2011 - 08/2014 | Scholarship of the Graduate School of Life Sciences, University of Würzburg funded by a grant of the German Excellence Initiative |
| 09/2012 - 12/2013 | Funding for a Research Stay in Marseille, France by the Bayerisch-Französisches Hochschulzentrum (BFHZ) |
| 10/2007 - 06/2008 | DAAD - Free Mover-Stipendienprogramm (FMS) Europa |

## Languages

| | |
|---|---|
| Mother Tongue: | German (fluent) |
| Other Languages | English (fluent, TOEFL-Score 109 in 2007)<br>French, Spanish, Latin (Intermediate) |

Würzburg, 26. September 2014

Johannes Tran-Gia

# C Publications

## Book Chapters

- Tran-Gia J, Köstler H, Seiberlich N. Chapter 16 : Fast Imaging. In "Basic Principles of Cardiovascular MRI: Physics and Imaging Technique", edited by Syed MA, Raman S, and Simonetti OP, Springer-Verlag, pending.

## Original Research

- Tran-Gia J, Wech T, Hahn D, Bley TA, and Köstler H. Consideration of Slice Profiles in Inversion Recovery Look-Locker Relaxation Parameter Mapping. Magn Reson Imag, doi: 10.1016/j.mri.2014.05.012 (2014).
- Wech T, Tran-Gia J, Bley TA, and Köstler H. Using self-consistency for an iterative trajectory adjustment (SCITA). Magn Reson Med, doi: 10.1002/mrm.25244 (2014).
- Wech T, Pickl W, Tran-Gia J, Ritter CO, Beer M, Hahn D, and Köstler H. Whole Heart Cine MRI in a Single Breath-hold - A Compressed Sensing Accelerated 3D Acquisition Technique for Assessment of Cardiac Function. RöFo 186(1):37-41 (2014).
- Tran-Gia J, Stäb D, Wech T, Hahn D, and Köstler H. Model-based Acceleration of Parameter mapping (MAP) for saturation prepared radially acquired data. Magn Reson Med 70:1524-1534 (2013).
- Wech T, Stäb D, Budich JC, Fischer A, Tran-Gia J, Hahn D, and Köstler H. Resolution evaluation of MR images reconstructed by iterative thresholding algorithms for compressed sensing. Med Phys 39(7):4328-4338 (2012).
- Linder F, Tran-Gia J, Dahmen SR, and Hinrichsen H. Long-range epidemic spreading with immunization. J Phys A: Math Theor 41:185005 (2008).

## Conference Contributions

- Tran-Gia J, Bisdas S, Köstler H, and Klose U. A Model-based Reconstruction Technique for Fast Dynamic T1 Mapping. Proceedings of the ISMRM 2014.
- Klose U, Bisdas S, Köstler H, and Tran-Gia J. Evaluation of Vascular Transfer Constants using Dynamic T1-Mapping during Contrast Agent Administration. Proceedings of the ISMRM 2014.
- Tran-Gia J, and Köstler H. Consideration of Slice Profiles (CSP) in Inversion Recovery Look-Locker T1 Mapping. Proceedings of the ESMRMB 2013.

- Tran-Gia J, and Köstler H. Berücksichtigung von Schichtprofilen bei der T1-Relaxationsparameter-Bestimmung mittels inversionspräparierter Look-Locker Sequenzen. Proceedings of the DGMP 2013.
- Wech T, Tran-Gia J, Hahn D, and Köstler H. Iterative Trajectory Correction for Radial Projection Imaging. Proceedings of the ISMRM 2013.
- Tran-Gia J, Troalen T, Köstler H, and Kober F. A Model-based Reconstruction Technique for Look-Locker FAIR Gradient Echo ASL Perfusion Data. Proceedings of the ISMRM 2013.
- Tran-Gia J, Hahn D, and Köstler H. A Model-based Reconstruction Technique for Inversion Recovery Prepared Radially Acquired Data. Proceedings of the ISMRM 2013.
- Tran-Gia J, Hahn D, and Köstler H. A Model-Based Reconstruction Technique for Radially Sampled Data Acquired after a Single IR Preparation. ISMRM Scientific Workshop on Data Sampling & Image Reconstruction 2013.
- Tran-Gia J, Stäb D, Hahn D, and Köstler H. A Model-Based Accelerated Parameter Mapping (MAP) Algorithm for Saturation Prepared Radially Acquired Data. Proceedings of the ESMRMB 2012.
- Tran-Gia J, Stäb D, Hahn D, and Köstler H. Ein modellbasierter Rekonstruktionsalgorithmus zur Bestimmung der Relaxationsparameter für radial aufgenommene Daten nach einer Sättigungs-Präparation. Proceedings of the DGMP 2012.
- Tran-Gia J, Stäb D, Hahn D, and Köstler H. A Model-Based Reconstruction Technique for Parameter Mapping of Saturation Prepared Radially Acquired Data. Proceedings of the ISMRM 2012.
- Tran-Gia J, Stäb D, Ritter CO, Hahn D, and Köstler H. A Model-based Reconstruction Technique for Quantitative Myocardial Perfusion Imaging. Proceedings of the ESCR 2011.
- Tran-Gia J, Stäb D, Hahn D, and Köstler H. A Model-based Reconstruction Technique for Saturation Prepared Radially Acquired Data. Proceedings of the ESMRMB 2011.
- Tran-Gia J, Stäb D, Ritter CO, Hahn D, and Köstler H. A Model-based Image Reconstruction Algorithm for Saturation Prepared Radially Acquired Data. Proceedings of the ISMRM 2011.
- Stäb D, Tran-Gia J, Ritter CO, Hahn D, and Köstler H. AIF Determination for Quantitative Myocardial Perfusion Imaging Using a Model Based Reconstruction of Radially Acquired Data. Proceedings of the ISMRM 2011.

# D Eidesstattliche Erklärung / Affidavit

## Eidesstattliche Erklärung

Hiermit erkläre ich an Eides statt, die Dissertation *Modellbasierte Rekonstruktionsmethoden für die MR-Relaxometrie* eigenständig, d.h. insbesondere selbstständig und ohne Hilfe eines kommerziellen Promotionsberaters, angefertigt und keine anderen als die von mir angegebenen Quellen und Hilfsmittel verwendet zu haben.

Ich erkläre außerdem, dass die Dissertation weder in gleicher noch in ähnlicher Form bereits in einem anderen Prüfungsverfahren vorgelegen hat.

Würzburg, 26. September 2014

Johannes Tran-Gia

## Affidavit

I hereby confirm that my thesis entitled *Model-Based Reconstruction Methods for MR Relaxometry* is the result of my own work. I did not receive any help or support from commercial consultants. All sources and / or materials applied are listed and specified in the thesis.

Furthermore, I confirm that this thesis has not yet been submitted as part of another examination process neither in identical nor in similar form.

Würzburg, 26. September 2014

Johannes Tran-Gia

# E Acknowledgements

A large number of people played a part in the completion of this doctoral thesis. Since all of them speak at least some German, I would like to take the liberty of writing this chapter in German. As my mother tongue, it serves much better for expressing my feelings than English.

Zuallererst danke ich meinem Doktorvater **Prof. Dr. Herbert Köstler**. Seit dem Beginn meiner Diplomarbeit vor mittlerweile fast schon 5 Jahren fühle ich mich in Ihrer Arbeitsgruppe sehr gut aufgehoben. Ich danke Ihnen, dass Sie durch einen offenen Umgang mit Ihren Mitarbeitern für eine sehr angenehme und produktive Atmosphäre innerhalb der von Ihnen geleiteten *Abteilung für Experimentelle Radiologie* des *Instituts für Diagnostische und Interventionelle Radiologie* sorgen. Stets konnte ich bei auftretenden Fragen und Problemen mit Ihrer Unterstützung rechnen. Dabei nahmen Sie sich sehr oft Zeit, die von mir erarbeiteten Ergebnisse "live" anzuschauen. Nach diesen Treffen brummte mir zwar oft der Kopf, ich hatte aber jedes Mal eine Vielzahl neuer Anregungen und Ideen, die es nun umzusetzen galt. Außerdem konnte ich auch bei jeglichen Rückschlägen (außer in Bezug auf meinen Lieblings-Fußballverein aus Stuttgart) immer mit aufbauenden und motivierenden Worten rechnen.

Des Weiteren bedanke ich mich bei unserem ehemaligen Institutsleiter **Prof. Dr. Dietbert Hahn** sowie seinem Nachfolger **Prof. Dr. Thorsten Bley**, die uns bildgebenden Physikern hier am Uniklinikum Würzburg ein sehr gutes Arbeitsumfeld geschaffen haben. Mir ist bewusst, dass es keinesfalls selbstverständlich ist, dass in einer radiologischen Abteilung ein so großer Wert auf die Entwicklung und Erforschung neuer Messverfahren in der MRT gelegt wird. An dieser Stelle möchte ich mich ausdrücklich auch bei **Prof. Dr. Christian Ritter** bedanken, der mir vor allem bei der kontrastmittelgestützten Herzperfusions-Probandenstudie, aber auch bei allen anderen medizinischen Fragestellungen stets sehr schnell und effektiv weitergeholfen hat. Auch persönlich haben wir im Rahmen einiger Konferenzen und Weihnachtsmarkt-Abende ein sehr freundschaftliches Verhältnis aufgebaut. Ich hoffe, dass Deine Verbundenheit mit unserer Abteilung auch von Göttingen aus erhalten bleiben wird. Abschließend möchte ich **Prof. Dr. Meinrad Beer** danken, bei dem ich während seiner Würzburger Zeit bei medizinischen Fragen immer ein offenes Ohr gefunden habe.

Besonderer Dank gebührt außerdem meinem langjährigen Zimmergenossen **Dr. Tobias Wech**. Seit dem Beginn unserer gemeinsamen Diplomarbeit vor etwa 5 Jahren haben wir zahllose angenehme und produktive Stunden im Büro verbracht, aber auch privat viele schöne Dinge erlebt - seien es mit anschließendem Road-Trip verbundene Konferenz-Teilnahmen in Salt Lake City oder Melbourne oder einfach nur gemeinsame Feierabende mit Minoas-Teller und Champions League. Mittlerweile muss ich mir sogar schon eingestehen, in einigen unaufmerksamen Momenten zu den BVB-Sympathisanten zu gehören. Nichtsdestotrotz vielen Dank für diese schöne Zeit!

Großer Dank gebührt natürlich auch allen anderen aktuellen, aber auch ehemaligen Kollegen in der Abteilung für Experimentelle Radiologie: **Dr. André Fischer**, **Dr. Marcel Gut-**

**berlet**, **Fabian Hilbert**, **Valentin Ratz**, **Anne Slawig**, **Dr. Daniel Stäb**, **Dr. Andreas Weng** und **Dr. Mario Zeller**. Ihr habt dem wissenschaftlichen Büro-Alltag nicht nur während der legendären Morgenbesprechung eine sehr menschliche Komponente hinzugefügt. Wo sonst kann man in entspannter Runde darüber diskutieren, ob sich Hamster nun wirklich ein Siphon bauen oder wie lange man auf dem Seeweg nach Australien braucht? Aber natürlich auch in Bezug auf MRT-Fragestellungen standet Ihr mir immer mit Rat und Tat zur Seite. Auch privat haben wir auf zahlreichen Geburtstagsfeiern, gemeinsamen Unternehmungen wie Betriebsausflügen, Retreats oder Konferenz-Reisen oder bei Fußballspielen gegen die Mediziner eine sehr freundschaftliche Beziehung aufgebaut. Vielen Dank! Tausend Dank auch an **Petra Küffner**. Nach Deiner Ankunft wurde die Lösung vieler vor allem nicht-physikalischer Problemstellungen deutlich leichter. Danke auch an alle Medizinisch-technischen Radiologieassistentinnen - allen voran **Bettina Borst** - die uns medizinischen Physikern in den letzten Jahren bei messbezogenen Fragestellungen wie beispielsweise der richtigen Planung der Schichten oder dem richtigen Setup der kontrastmittelverstärkten Herzperfusionsmessungen immer eine große Hilfe waren.

Dank gebührt außerdem der **Graduate School of Life Sciences (GSLS)**, die einen perfekten Rahmen für die Promotion von Naturwissenschaftlern am Uniklinikum Würzburg bildet. Als Stipendiat der GSLS hatte ich das große Glück, während meiner gesamten Promotion finanziell abgesichert zu sein und mich ganz auf die Arbeit konzentrieren zu können. Außerdem wurden mir im Rahmen des Stipendiums Forschungsmittel zur Verfügung gestellt, mit denen ich mir die für die teils sehr rechenaufwendigen Rekonstruktionen notwendige Hardware besorgen konnte, was mir aber auch die Teilnahme an zahlreichen Workshops und Konferenzen ermöglichte. An dieser Stelle möchte ich **Dr. Gabriele Blum-Oehler**, **Bianca Putz** und **Jennifer Heilig** hervorheben, die mir in allen Fragen bezüglich der Organisation meiner Promotion stets freundlich und geduldig weitergeholfen haben.

Dank auch an das **Bayerisch-Französische Hochschulzentrum (BFHZ)**, das mich bei einem Forschungsaufenthalt in *Marseille* finanziell unterstützte.

Bedanken möchte ich mich des Weiteren bei **Prof. Dr. Uwe Klose**, der mir im Rahmen einer Kooperation mit der **Uniklinik Tübingen** ermöglichte, den MAP-Algorithmus zur Lösung klinischer neuroradiologischer Fragestellungen einzusetzen.

Besonderer Dank geht auch an **Dr. Frank Kober** und **Dr. Thomas Troalen**. Dank Eurer Unterstützung konnte ich während eines sehr produktiven Forschungsaufenthaltes in *Marseille* den in dieser Arbeit vorgestellten Algorithmus für die präklinische Forschung implementieren. Abgesehen vom sehr produktiven Arbeitsumfeld wurde ich auch abseits der Arbeit sehr freundschaftlich aufgenommen. Ich habe unsere gemeinsamen Abende an der Côte D'Azur sehr genossen und hoffe, dass wir unsere Zusammenarbeit auch weiterhin aufrechterhalten werden, oder uns zumindest weiterhin regelmäßig auf Konferenzen treffen werden.

Bedanken möchte ich mich auch bei **Dr. Nicole Seiberlich** und der gesamten MR-Arbeitsgruppe der *Case Western Reserve University*, die mich im Rahmen eines Forschungsaufenthaltes in *Cleveland* sehr herzlich empfangen und bestmöglich dabei unterstützt haben, den in dieser Arbeit entwickelten Algorithmus für die quantitative Herzperfusionsmessung mit spiralen Trajektorien anzuwenden. Ich hoffe, dass wir unsere gute Zusammenarbeit auch zukünftig aufrechterhalten werden.

Mein tiefster Dank gebührt meinen Eltern **Walburga Wodarz-Tran-Gia** und **Phuoc Tran-Gia**. Ihr habt mir das beste Fundament gelegt, das man sich als Kind von seinen Eltern wünschen kann. Dank Euch habe ich während meines gesamten Lebens immer das Gefühl gehabt, dass jemand hinter mir steht und für mich da ist. Durch Eure bedingungslose Unterstützung, aber auch ehrliche Kritik, bin ich zu dem Menschen geworden, der ich heute bin. An dieser Stelle möchte ich auch meinem Bruder **Thomas Tran-Gia** danken. Ich bin froh, dass ich nicht der einzige bin. Oder wie Du zu sagen pflegst: Blut ist eben meistens doch dicker als Wasser.

Das letzte und wohl auch größte Dankeschön gilt **Johanna Dreß**, meiner besseren Hälfte. Ich bin sehr froh, Dich vor über 12 Jahren getroffen zu haben und seitdem gemeinsam mit Dir durchs Leben zu gehen. Ich weiß es sehr zu schätzen, jemanden zu haben, der mich so versteht wie ich bin und mich in guten wie in schlechten Zeiten bedingungslos und mit all seiner Kraft unterstützt. Ich wünsche mir von ganzem Herzen, dass wir noch einen sehr langen gemeinsamen Weg vor uns haben.

# F Appendix

Quantified values of the myocardial blood flow obtained in all 6 sectors (S1-S6) using AIF determination method A, B and C for all volunteers (V1-V6). Additionally, the mean values ($\mu$), the standard deviations ($\sigma$) as well as the relative errors ($\mu/\sigma$) are listed.

| Method | Volunteer | S1 | S2 | S3 | S4 | S5 | S6 | $\mu \pm \sigma$ | $\sigma/\mu(\%)$ |
|---|---|---|---|---|---|---|---|---|---|
| A | V1 | 0.68 | 0.74 | 0.95 | 0.61 | 0.55 | 0.64 | **0.69 ± 0.14** | **20.0** |
| | V2 | 0.74 | 0.91 | 1.21 | 0.86 | 0.72 | 0.73 | **0.86 ± 0.19** | **21.7** |
| | V3 | 0.84 | 0.90 | 0.80 | 0.59 | 0.50 | 0.65 | **0.71 ± 0.16** | **21.9** |
| | V4 | 0.79 | 0.92 | 1.00 | 0.72 | 0.54 | 0.75 | **0.78 ± 0.16** | **20.8** |
| | V5 | 0.64 | 0.82 | 0.73 | 0.51 | 0.55 | 0.58 | **0.64 ± 0.12** | **18.8** |
| | V6 | 0.72 | 1.02 | 1.21 | 0.70 | 0.63 | 0.68 | **0.83 ± 0.23** | **28.4** |
| | AVG | 0.73 | 0.89 | 0.98 | 0.66 | 0.58 | 0.67 | **0.75 ± 0.17** | **22.1** |
| B | V1 | 0.54 | 0.60 | 0.76 | 0.49 | 0.44 | 0.51 | **0.56 ± 0.11** | **20.0** |
| | V2 | 0.53 | 0.64 | 0.86 | 0.61 | 0.51 | 0.52 | **0.61 ± 0.13** | **21.6** |
| | V3 | 0.76 | 0.83 | 0.76 | 0.57 | 0.50 | 0.61 | **0.67 ± 0.13** | **19.8** |
| | V4 | 0.54 | 0.62 | 0.69 | 0.49 | 0.37 | 0.51 | **0.54 ± 0.11** | **20.7** |
| | V5 | 0.53 | 0.67 | 0.61 | 0.41 | 0.44 | 0.47 | **0.52 ± 0.10** | **19.1** |
| | V6 | 0.54 | 0.76 | 0.91 | 0.53 | 0.48 | 0.51 | **0.62 ± 0.18** | **28.3** |
| | AVG | 0.57 | 0.69 | 0.76 | 0.52 | 0.46 | 0.52 | **0.59 ± 0.13** | **21.7** |
| C | V1 | 0.62 | 0.67 | 0.87 | 0.55 | 0.51 | 0.58 | **0.64 ± 0.13** | **20.0** |
| | V2 | 0.59 | 0.73 | 0.98 | 0.70 | 0.57 | 0.58 | **0.69 ± 0.16** | **22.6** |
| | V3 | 0.88 | 0.96 | 0.87 | 0.65 | 0.57 | 0.71 | **0.77 ± 0.15** | **19.7** |
| | V4 | 0.85 | 0.81 | 1.10 | 0.79 | 0.59 | 0.81 | **0.82 ± 0.16** | **19.8** |
| | V5 | 0.63 | 0.80 | 0.74 | 0.50 | 0.54 | 0.57 | **0.63 ± 0.12** | **18.8** |
| | V6 | 0.60 | 0.85 | 1.01 | 0.59 | 0.54 | 0.58 | **0.70 ± 0.19** | **27.6** |
| | AVG | 0.69 | 0.80 | 0.93 | 0.63 | 0.55 | 0.64 | **0.71 ± 0.15** | **21.4** |

**Table F.1:** Perfusion values (ml/g/min) for all 6 sectors of all 6 volunteers as well as the average over all volunteers.